Noise reduction of rotating machinery by viscoelastic bearing supports

H.G. Tillema

This research project was supported by and carried out at the SKF Engineering & Research Centre BV in Nieuwegein, the Netherlands. The support is gratefully acknowledged.

De promotiecommissie is als volgt samengesteld:

Voorzitter en secretaris:
Prof.dr.ir. H.J. Grootenboer, Universiteit Twente
Promotor:
Prof.dr.ir. H. Tijdeman, Universiteit Twente
Assistent-promotor:
Dr.ir. J.A. Wensing, SKF ERC
Leden:
Prof. E. Ioannides DIC,MSc,PhD, Imperial College University London/SKF ERC
Prof.dr.ir. J.B. Jonker, Universiteit Twente
Prof.dr.ir. J.W.M. Noordermeer, Universiteit Twente
Prof.dr.ir. D.J. Schipper, Universiteit Twente

Tillema, Hedzer Gido

Title: Noise reduction of rotating machinery by viscoelastic bearing supports
PhD thesis, University of Twente, Enschede, The Netherlands
February 2003

ISBN: 90-36518776
Subject headings: viscoelasticity, acoustics, rolling bearings

Cover with permission of SKF

Printed by Ponsen & Looijen bv., Wageningen, The Netherlands

NOISE REDUCTION OF ROTATING MACHINERY BY VISCOELASTIC BEARING SUPPORTS

PROEFSCHRIFT

ter verkrijging van
de graad van doctor aan de Universiteit Twente,
op gezag van de rector magnificus,
prof.dr. F.A. van Vught,
volgens besluit van het College voor Promoties
in het openbaar te verdedigen
op donderdag 27 februari 2003 te 13.15 uur.

door

Hedzer Gido Tillema

geboren op 12 juni 1975
te Nunspeet

Dit proefschrift is goedgekeurd door de promotor

Prof.dr.ir. H. Tijdeman

en de assistent-promotor

Dr.ir. J.A. Wensing

Summary

The demand for silent rolling bearing applications, such as electric motors and gearboxes, has resulted in an investigation of viscoelastic bearing supports. By placing a thin viscoelastic layer between the bearing outer ring and the surrounding structure, vibrations of the shaft-bearing arrangement can be isolated and damped in such a way that the radiated sound power is reduced. The ultimate goal of this research was to develop a design strategy for viscoelastic bearing supports resulting in an effective noise reduction.
This thesis describes the dynamic and acoustic behaviour of rolling bearing applications with viscoelastic bearing supports. Ultimately, the investigations cover a wide range of aspects in mechanical engineering:

(1) the description of viscoelastic material behaviour;
(2) development of a new Component Mode Synthesis method for viscoelastic components;
(3) experimental investigations into the mechanical properties of viscoelastic materials;
(4) development of advanced structural models of rotor dynamics applications;
(5) numerical and experimental investigations of the dynamic and acoustic behaviour of an electric motor;
(6) development of a design strategy for noise reduction by viscoelastic bearing supports

In the present research, elastic components, like the shaft or the housing, and the viscoelastic support are modelled with the finite element method. In addition, the models are reduced by Component Mode Synthesis to save computation time. Viscoelasticity is described by a generalised Maxwell representation suitable for both time and frequency domain analyses. Viscoelastic materials are measured on a Dynamic Mechanical Analyzer to obtain the frequency dependent stiffness and damping characteristics.

The viscoelastic modelling approach is succesfully validated at a component level with sandwich rings. The results showed that a significant amount of damping can be created by the viscoelastic layer.

As a next step, numerical and experimental studies were performed on a rotor dynamics test rig. A clear vibration reduction was achieved with viscoelastic supports, especially for high running speeds.

Subsequently, the dynamic and acoustic behaviour of a running electric motor was analysed. The acoustic analysis was based on the boundary element method using so-called radiation modes. The agreement between experimental and numerical results was satisfactory in the noisiest frequency range from 1000 to 2500 Hz. It was found that the sound power level of the electric motor can be reduced by 3 to 5 dB(A) with a viscoelastic bearing support.

Finally, a strategy is proposed for designing noise reducing viscoelastic bearing supports. A set of qualitative design rules and a more quantitative design approach are presented.

Samenvatting

De vraag naar stille rollagerapplicaties, zoals elektromotoren en tandwielkasten, heeft geleid tot een onderzoek naar visco-elastische lagerophangingen. Door middel van het plaatsen van een dunne visco-elastische laag tussen de buitenring van het lager en de omringende constructie, kunnen trillingen van de as-lager combinatie worden geïsoleerd en gedempt, op een dusdanige manier dat het afgestraald geluidsvermogen vermindert. Het uiteindelijke doel van dit onderzoek is de ontwikkeling van een ontwerpstrategie voor visco-elastische lagerophangingen welke resulteren in een effectieve lawaaireductie.

Dit proefschrift beschrijft het dynamisch en akoestisch gedrag van rollagerapplicaties met visco-elastische lagerophangingen. Uiteindelijk bestrijkt het onderzoek een breed scala aan aspecten in de werktuigbouwkunde:

(1) de beschrijving van visco-elastisch materiaalgedrag;
(2) ontwikkeling van een nieuwe Component Mode Synthese methode voor visco-elastische componenten;
(3) experimenteel onderzoek naar de mechanische eigenschappen van visco-elastische materialen;
(4) ontwikkeling van geavanceerde structurele modellen van rotordynamica toepassingen;
(5) numeriek en experimenteel onderzoek naar het dynamisch en akoestisch gedrag van een elektromotor;
(6) ontwikkeling van een ontwerpstrategie voor visco-elastische lagerophangingen met als doel lawaaireductie

In dit onderzoek worden elastische componenten, zoals de as of het huis, en de visco-elastische ophanging gemodelleerd met de eindige elementen methode. Bovendien worden de modellen gereduceerd met Component Mode Synthese om rekentijd te besparen. Visco-elasticiteit wordt beschreven door een Maxwell representatie welke geschikt is voor analyses in zowel het tijds-

als in het frequentiedomein. Visco-elastische materialen worden gemeten in een Dynamic Mechanical Analyzer om de frequentie afhankelijke stijfheids- en dempingseigenschappen te verkrijgen.

Het visco-elastische model is met succes gevalideerd op componentniveau met behulp van sandwichringen. De resultaten lieten zien dat een significante hoeveelheid demping gecreëerd kan worden door de visco-elastische laag.
Als vervolgstap zijn numerieke en experimentele studies uitgevoerd aan een rotordynamica testopstelling. Een duidelijke trillingsreductie is behaald met visco-elastische lagerophangingen, vooral voor hoge omloopsnelheden.
Vervolgens is het dynamisch en akoestisch gedrag van een roterende elektromotor geanalyseerd. De akoestische analyse is gebaseerd op de rand elementen methode gebruikmakend van zogenaamde afstraalmodes. De overeenkomst tussen experimentele en numerieke resultaten was bevredigend in het meest lawaaiige frequentiegebied van 1000 tot 2500 Hz. Het is aangetoond dat het niveau in geluidsvermogen van de elektromotor met 3 tot 5 dB(A) kan worden gereduceerd door middel van een visco-elastische lagerophanging.

Tenslotte is een strategie voorgesteld voor het ontwerpen van geluidsreducerende visco-elastische lagerophangingen. Een set van kwalitatieve ontwerpregels en een meer kwantitatieve ontwerpaanpak zijn gepresenteerd.

Contents

Chapter 1

Introduction

1.1 Background

The demand for low noise machinery has become an increasingly important issue in our society. Typical examples of nuisance caused by noise are often experienced in household appliances such as vacuum cleaners, washing machines or refrigerators. At work the inconvenience due to noise can be caused by computers, air conditioning systems or industrial machines. Noise, the term for unwanted sound, is closely related to the occurrence of structural vibrations. The vibrating surfaces of a structure excite the surrounding medium, in most cases air, causing pressure disturbances which are experienced as noise. This phenomenon is known as noise radiation. In many cases where noise is a problem, rotating machinery such as electric motors or gear boxes are involved. The vibration source in these types of machinery are electromagnetic forces, the meshing of gears or mechanical vibrations caused by imbalance of the rotating parts. Often, the resulting vibrations are transmitted from the rotating parts to the surrounding structure, which in the end radiates noise. Generally, the rolling bearings in such applications are relatively flexible components. Therefore, the bearings play a crucial role in the application as a vibration transmitter. As a vibration source, the rolling bearings have become less important, mainly due to improved quality.

In order to reduce the noise level of rotating machinery, either the source, the transfer or the radiation of noise can be suppressed. Source reduction, for example, can be achieved by altering the running conditions such as, if possible, the rotational speed or the bearing preload (Wensing, 1998a). The transfer and radiation of noise can be reduced by a smart (re)design of the structural components of the application. The transfer of noise can also be reduced by decoupling the components in such a way that the noise path is interrupted. This can be achieved by adding noise reducing treatments to the structure such as elastic elements, masses, local shielding or damping layers. In the present investigation, the use of viscoelastic damping layers as a noise reducing measure in rotating machinery is considered.

1.2 Viscoelastic bearing support

In many cases, structural vibrations in rotating machinery are transmitted from the shaft and the bearings to the surrounding structure, also known as the housing. Due to its relatively large surface the housing often radiates most of the noise. The basic idea of the present project is to implement a viscoelastic layer between the outer ring of a rolling bearing and the housing (Figure 1.1). In order to interrupt the vibration transmission path the bearings are supported in soft viscoelastic sleeves.

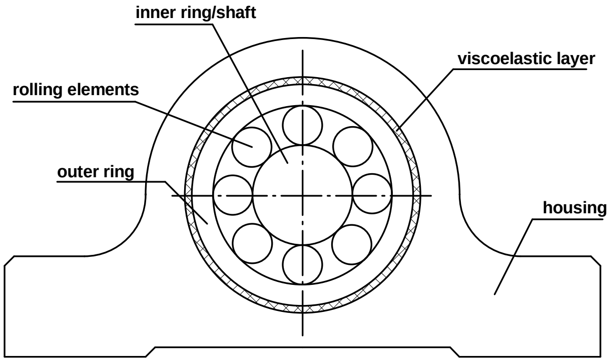

Figure 1.1: *A viscoelastic layer mounted between the bearing outer ring and the housing.*

In this way vibrations of the shaft are isolated from the surrounding structure. Moreover, the viscoelastic layer can introduce a significant amount of damping. A disadvantage of a relatively soft bearing support is the decrease in static stiffness of the application. As a result, the running accuracy of the system can be affected in such a way that the excitation level increases. Therefore, a balance needs to be found between a suitable combination of vibration isolation and damping on the one hand and static and dynamic support on the other.

In recent years active and hybrid noise control have become popular subjects of study. In some of these techniques, for example, piezo-electric elements are used to control the deformation of a viscoelastic damping layer (Baz, 1993; Shen, 1996). These methods, however, are still in their infancy. The present research focuses on the passive use of viscoelastic layers.

1.3 Vibration isolation and damping

The principles of vibration isolation and vibration damping can easily be explained with the help of simple mass-spring systems. Let us consider a vibrating object transmitting vibrations to a certain structure via a specific stiffness. In the two-dimensional example this system is represented by two masses $M1$ and $M2$ and springs $K1$ and $K2$ on an excited support (see Figure 1.2a). The vibrating support, for example, could represent a shaft, whereas the two masses could represent a housing with 2 degrees of freedom.

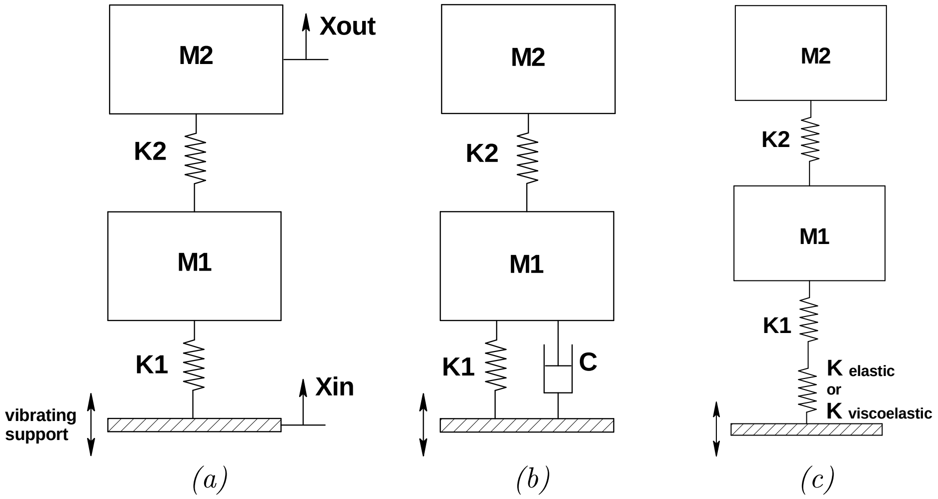

(a) (b) (c)

Figure 1.2: *Two-dimensional mass-spring systems on an excited support: (a) reference system, (b) viscously damped system and (c) (visco)elastically supported system.*

Vibration damping can be achieved by adding a parallel damper C to the system (Figure 1.2b). Vibrations of the support can be isolated by use of a soft elastic or viscoelastic support, indicated by $K_{elastic}$ and $K_{viscoelastic}$, respectively, in Figure 1.2c.

In the case of a harmonic excitation of the support the transmissibility of the system is defined as the ratio between the displacement of mass $M2$, $\mathbf{X_{out}}$, and the displacement of the vibrating support $\mathbf{X_{in}}$. Obviously, a low transmissibility implies a good vibration isolation. The transmissibility curves of the reference system, the viscously damped system and the elastically supported system are collected in Figure 1.3. In addition, the curve of a viscoelastically supported system is shown.

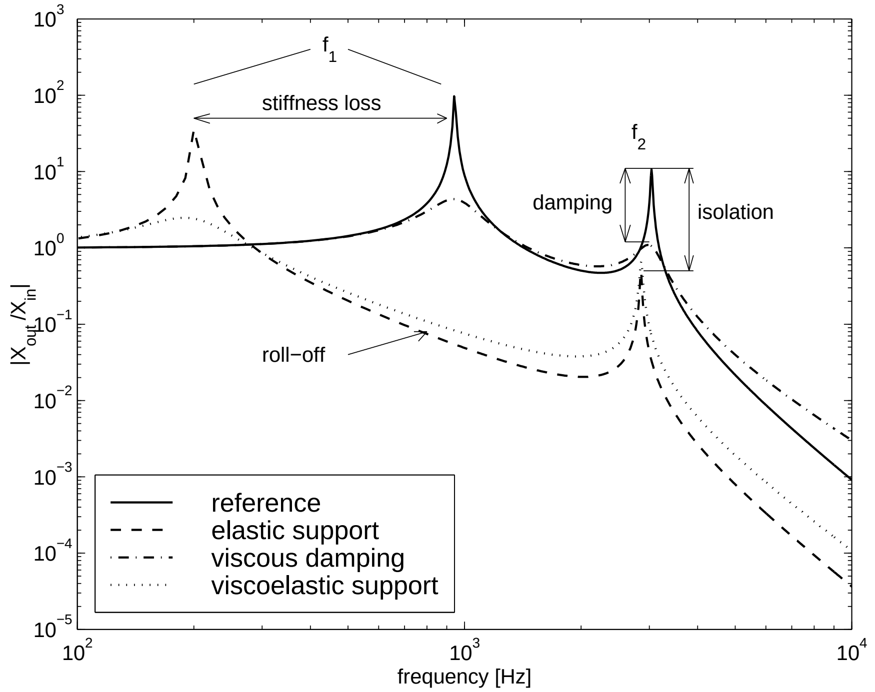

Figure 1.3: *Transmissibility of the 2-DOF mass-spring system.*

The system shows two resonance frequencies. At the lowest resonance frequency, f_1, both masses move in phase on the spring with stiffness $K1$. At the second resonance frequency, f_2, the masses move out of phase. Clearly, the vibration amplitudes of the reference system near the resonance frequencies are reduced when a viscous damping treatment is applied. In the case of an elastically supported system the first resonance frequency significantly decreases as a result of the stiffness loss. For frequencies above the first resonance frequency, however, the transmissibility decreases with increasing driving frequency, the so-called *roll-off*. As a consequence, the second resonance frequency is effectively isolated. In many cases, isolation is more effective than a reduction in vibration level by the addition of damping.

The effects of both damping and isolation can be combined by applying a viscoelastic support as demonstrated in the figure. In that way, the first resonance peak is highly damped, and the isolation of the second peak is also effective. This makes viscoelastic materials particularly attractive for the reduction of noise and vibrations.

In practice, the choice of the support depends on several aspects of the application; for example the characteristics of excitation, the requirements with respect to the static stiffness and the geometrical constraints.
It will be clear that in the present investigations on bearing applications, a simplified mass-spring system is not sufficient and that one has to resort to more accurate dynamic models. The mechanisms of vibration isolation and damping, however, are in principle very similar.

1.4 General approach

Application of viscoelastic materials in perspective

Viscoelastic materials have been used in industrial applications for many years for their outstanding vibration isolation and damping properties over wide temperature and frequency ranges (Nashif, Jones and Henderson, 1985). Examples of discrete viscoelastic damping devices are engine mounts, transmission couplings, shock absorbers and suspension bushings. In sheet metal structures, viscoelastic materials are applied as a surface damping treatment to solve resonant noise and vibration problems. The design of an effective viscoelastic layer configuration in this type of application is based on the laminate theories by Ross, Ungar and Kerwin (1959) and Mead and Markus (1969). Recently, viscoelastic damping materials have also been used in rotor dynamic applications. For rotor stability improvement, viscoelastic bearing supports have been studied by some researchers (Dutt and Nakra, 1992; Panda and Dutt, 1999). The dynamic behaviour of viscoelastically supported bearing applications has been analysed by Dutt and Nakra (1993), Aktürk and Gohar (1994) and Shabaneh and Zu (2000). In all of these studies, the structure is represented by a two-dimensional, analytical model with a simple geometry. Moreover, the bearings are modelled in an oversimplified way.

The present study focuses on the understanding and the prediction of the dynamic behaviour of applications with viscoelastic bearing supports through a more sophisticated numerical approach. Ultimately, this should lead to better results and to a design strategy for practical purposes.

Present approach

The SKF Engineering & Research Centre developed a research program, called Orpheus, to accurately predict the dynamic behaviour of bearing applications. The program used comprises both the detailed dynamics of the rolling bearing and the flexibility of the elastic components, such as the shaft and the housing. An essential part of the methods used is based on the work of Wensing (1998a), who analysed transient dynamic effects occuring in rolling bearing applications. For that purpose the Finite Element Method (FEM) was used to describe the structure in combination with the so-called Component Mode Synthesis (CMS) in order to effectively reduce the number of degrees of freedom.

In view of the present study it was essential to include also the possibility of handling viscoelastic materials. This type of material is characterised by a strong time- and frequency dependent stiffness and damping. This is, of course, of major importance for the static and dynamic characteristics of the system we are looking at. This urged for the development of a new CMS reduction method, suited for viscoelastic components.

Clearly, the numerical models must be validated by means of experiments. In the present approach, the validation of the viscoelastic model is performed with the help of several ring samples with viscoelastic layers.

As a next step, the dynamic behaviour of a complete bearing application is validated. This is applied on a rotor dynamics test rig and an electric motor.

Besides the prediction of the structural behaviour of an application, it is also essential to analyse the acoustic radiation of the structure. For that purpose the Boundary Element Method (BEM) is employed, a method with which the acoustic behaviour of a vibrating object in a free field can be predicted. In the present approach, BEM is used to determine the radiated sound power level of the vibrating structure in A-weighted decibels, which is representative for the perception of the human ear. The approach is applied for the acoustic evaluation of the electric motor with viscoelastic bearing supports. The acoustic model of this application is validated with the results obtained from sound intensity measurements on the running electric motor.

1.5 Problem definition

In view of the considerations in the previous sections, this research project focuses on two major aspects:

- Development and validation of a numerical tool to predict the dynamic and acoustic behaviour of a bearing application with viscoelastic bearing supports.
- Application of a viscoelastic bearing support in an actual rotor dynamics application and to demonstrate a significant noise reduction.

1.6 Outline of thesis

Chapter 2 presents the way in which the structural dynamics of a bearing application with viscoelastic bearing supports is modelled. This includes the models for the rolling bearing, the elastic components and the viscoelastic bearing support. For this purpose a new reduction method is developed, which is validated with results obtained from a full FEM simulation.

In Chapter 3 the numerical model for viscoelastic material behaviour is validated by means of experiments. First, the material properties are obtained from dynamic tests on a material sample. Based on these results, the stiffness and damping properties can be approximated numerically by a number of model parameters. Secondly, experiments are performed on steel ring samples with constrained viscoelastic damping layers. It will be shown that the predicted dynamic responses of these samples agree well with experimental results.

A complete rotor dynamics assembly is studied in Chapter 4. It concerns a test rig in which for both non-rotating and rotating conditions the vibrations of a shaft are effectively isolated from the housing by viscoelastic bearing supports. Moreover, it is shown that numerical results are in good agreement with the experiments.

Chapter 5 deals with the dynamic behaviour of an electric motor. An advanced structural model is constructed and validated. In addition, a redesign of the motor was carried out to implement a viscoelastic bearing support in practice. Vibration measurements show the potential for noise reduction by a viscoelastic layer in the vicinity of the rolling bearings.

Acoustic investigations, including both computations and experiments, are carried out on the electric motor (Chapter 6). The radiated sound power is chosen as a measure for the acoustic performance of the application. This quantity is efficiently determined with BEM in combination with the so-called radiation modes formulation. The acoustic model of the electric motor is validated by means of sound intensity measurements on the rotating system. These measurements also show a clear noise reduction if a properly designed viscoelastic bearing support is applied.

Based on the results obtained from the investigations so far, a design strategy including some essential design rules is presented in Chapter 7. Some parameter studies for the viscoelastic support design are performed for the test rig and the electric motor. It demonstrates the possibility for a further improvement of noise and vibration levels.

Finally, conclusions and recommendations are presented in Chapter 8.

Chapter 2

Modelling

2.1 Introduction

Numerical simulation is widely used to predict the dynamic behaviour of products in the design stage. Nowadays, this is also valid for the dynamics of rotating machinery containing rolling bearings. Critical modelling aspects encountered in such systems are the time dependence and the nonlinearity of the Hertzian contacts in the rolling bearings and the interfaces between adjacent components. As a consequence, advanced modelling techniques are required.

This chapter addresses the modelling procedure for a complete bearing application including viscoelastic bearing supports. For this purpose, a distinction is made between three important components of the system: the bearing, the viscoelastic layer and the linear elastic components such as the shaft or the housings.

The rolling bearing model is based on the work by Wensing (1998a) and is explained in Section 2.2. In this approach, the bearing is represented by a mass-spring-damper system with which both the generation of vibrations and the vibration transmission phenomena can be described.

As mentioned earlier we consider the possible application of a constrained damping layer mounted between the outer ring of the bearing and the housing. This layer exhibits viscoelastic material behaviour, which is characterised by time or frequency dependent stiffness and damping properties. This material behaviour and the derivation of the equations of motion for a viscoelastic component forms the subject of Section 2.3.

The linear elastic components in the application, such as a shaft or a housing, often have a complex geometry. In order to predict the dynamic behaviour of such components the engineer generally makes use of the so-called finite element method (FEM). In FEM the structure is subdivided into a large number of finite elements. For a good accuracy, a finite element model usually consists of thousands of degrees of freedom with associated equations. For simulations of the time dependent behaviour of complex systems this can result in very elaborate computations. To overcome this problem the size of a linear elastic component model is reduced using so-called *component mode synthesis* (CMS), which is discussed in Section 2.4.

In order to predict the dynamic behaviour of an arbitrarily shaped viscoelastic component this must also be modelled with FEM. Moreover, the FEM model of the viscoelastic component needs to be reduced by CMS to limit computation times and to enable an easy coupling with the adjacent elastic components. For this purpose, a new CMS technique has been developed, which accounts for viscoelastic material behaviour. This method is then validated by comparing the results of the reduced model with those of the original (full) finite element model.

The model of a complete rotor dynamics application is constructed by assembling the seperate models of each component (Section 2.5). With this model transient analyses in the time domain as well as harmonic response and modal analyses in the frequency domain can be performed.

In Figure 2.1 a schematic overview of the complete modelling procedure is presented. For the sake of completeness, the acoustic analyses are also shown in this diagram. This subject matter, however, is covered in Chapter 6.

2.2 Bearing model

In rotor dynamic applications, such as electric motors or gear boxes, rolling bearings are used to overcome the difference in speed between the rotor and its surrounding structure, often referred to as the housing. In addition, the bearings and the housings need to provide sufficient static support for the rotor.

Rolling bearings consist of a number of rolling elements guided by the raceways of an inner and an outer ring and separated by a cage (see Figure

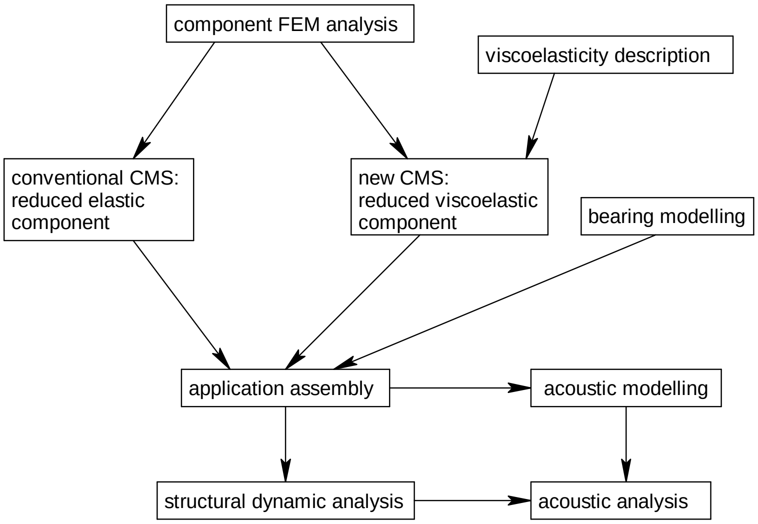

Figure 2.1: *Schematic overview of the modelling procedure.*

2.2). Moreover, the bearings are lubricated with oil or grease to reduce wear and friction and to increase their life.

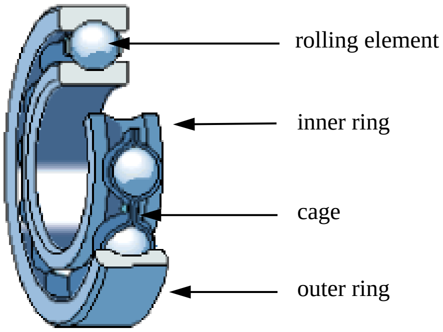

Figure 2.2: *A deep groove ball bearing*

The rolling bearing acts both as a vibration source and as a vibration transmitter. The excitation in a bearing is caused by several mechanisms. Firstly, a rolling bearing will generate vibrations due to the rotation of a

finite number of loaded rolling contacts between the balls and the guiding rings. The bearing stiffness becomes explicitly dependent on time as these contacts are elastic. As a result, vibrations are generated. This mechanism is called *parametric excitation* and is regarded as one of the main vibration sources in rolling bearings (Wensing, 1998a). Secondly, small imperfections of the contacting surfaces due to irregularities in the grinding and honing process cause vibrations. These imperfections are often classified according to wavelength and are also referred to as waviness. Waviness imperfections are global sinusoidally shaped imperfections with wavelengths that are much larger than the dimensions of the Hertzian contact areas. Finally, surface roughness, contamination, grease and the cage contribute to the generation of vibrations in a rolling bearing.
It should be noted, however, that nowadays rolling bearings have become products of high quality, also from a vibrational point of view. This is mainly a result of improved manufacturing techniques.

Apart from the excitation by the bearing, vibrations can be generated by various other parts of the application. In automotive appliances, for example, gear contacts cause vibrations as a result of geometrical inaccuracies and gear tooth flexibility. Alternatively, an important vibration source in electric motors are the electromagnetic forces acting between the rotor and the stator. Often, these types of vibrations are transmitted from the shaft via the bearings to a housing. Due to its large surface, the housing generally radiates most of the acoustic energy. Essentially, the rolling bearings now act as vibration transmitters. In many cases the vibrations that are caused by gear contacts or electromagnetic forces are of much larger amplitude than those generated by the bearing itself.

A three-dimensional numerical model of a rolling bearing was developed by Wensing (1998a), who accounted for the flexibility of the outer ring, the effect of lubrication and the influence of geometrical imperfections (waviness). This model was validated successfully with experiments on a bearing vibration test spindle (Wensing, 1998b).
The bearing model used in the present study is based on the afore mentioned model, though subjected to some simplifications. First, it is assumed that both the inner ring and the outer ring of the bearing can be considered as being rigid. This assumption is justified because in the present study relatively small bearings are considered, i.e. with an outer diameter of up to 35 mm. In our frequency range of interest, i.e. from 10 Hz to about 10

kHz, the flexibility of the outer ring plays a role in larger size bearings only. Because the lubricated contact model is considered as being too complex in view of the present study, the stiffness of the lubricant film is neglected here. Instead, a Hertzian stiffness is assumed in every ball-raceway contact. The effect of lubrication damping, however, is accounted for. For more details on the effects of lubrication in rolling bearings the reader is referred to Wijnant (1998) and Wijnant, Wensing & van Nijen (1999).
Finally, it should be mentioned that the effect of bearing waviness is not included and that only parametric excitation is considered as a possible source of vibration in the bearing.

The rolling bearing is represented by an inner and outer ring connected by a series of mass-spring-damper systems, as illustrated in Figure 2.3.

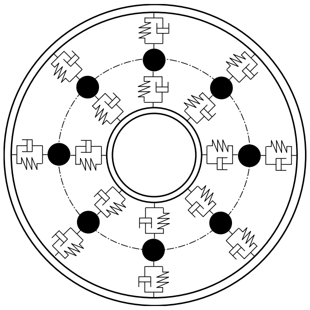

Figure 2.3: *The model of a ball bearing, represented by mass-spring-damper systems.*

When applying the assumptions mentioned earlier, each contact stiffness is described by a nonlinear spring (Hertz, 1881) and the damping by a linear viscous damper. The contact force in each ball-raceway contact is given by:

$$F_c = \kappa \delta_c^{\frac{3}{2}} + c\dot{\delta}_c \tag{2.1}$$

where δ_c is the contact displacement and $\dot{\delta}_c$ its time derivative. The deflection coefficient κ is determined by the material and geometrical properties of the elastic bodies. The viscous damping coefficient c is not only determined by these properties but also by the properties of the lubricant and the surface velocities in the contact.
When the rolling elements are considered to be massless, the inner and

outer contact of each rolling element can be represented by a model with the inner and outer spring-damper systems connected in series (Figure 2.4).

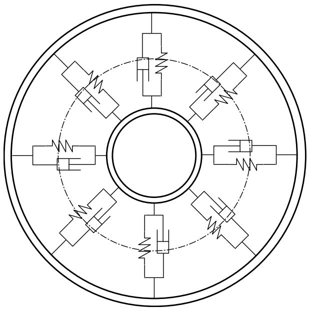

Figure 2.4: *The reduced model of a ball bearing.*

The resulting deflection coefficient κ_{res} of this combined system reads:

$$\kappa_{res} = (\frac{1}{\kappa_i^{2/3}} + \frac{1}{\kappa_o^{2/3}})^{-3/2} \tag{2.2}$$

where κ_i and κ_o are the deflection coefficients for the inner and outer raceway contact, respectively. The resulting contact damping coefficient is given by:

$$c_{res} = (\frac{1}{c_i} + \frac{1}{c_o})^{-1} \tag{2.3}$$

where c_i and c_o are the contact damping coefficients for the inner and outer raceway contact, respectively.
The cage is solely accounted for by assuming a constant angle between two consecutive rolling elements.

A Lagrangian approach is adopted to derive the equations of motion of the different bearing components, i.e. the inner ring and the outer ring. The constitutive relations of the contact model are used to describe the interaction between the structural components of the bearing. The equations of motion for the inner ring and the outer ring yield:

$$[m_i]\{\ddot{q}_i\} + \textstyle\sum_{j=1}^{Z} F_{res}^j \frac{\partial \delta_{res}^j}{\partial \{q_i\}} = \{f_i\} \tag{2.4}$$

$$[m_o]\{\ddot{q}_o\} + \textstyle\sum_{j=1}^{Z} F_{res}^j \frac{\partial \delta_{res}^j}{\partial \{q_o\}} = \{f_o\} \tag{2.5}$$

where F^j_{res}, δ^j_{res}, denote the force and displacement of the combined inner and outer ball-raceway contact, respectively. Z is the total number of rolling elements, whereas $[m_i]$ and $[m_o]$ represent the mass matrices of the inner and outer rings. The degrees of freedom (DOF) for the inner and outer rings are stored in the vectors $\{q_i\}$ and $\{q_o\}$. Because the rings are assumed rigid, the vector containing the degrees of freedom for each ring consists of three translations and three rotations. The generalised external forces are stored in $\{f_i\}$ and $\{f_o\}$. Finally, it is noted that gyroscopic effects are assumed to be negligibly small and are therefore not accounted for.

2.3 The modelling of viscoelastic material

Many materials exhibit a behaviour which combines liquidlike and solidlike characteristics. Such a material slowly deforms with time under constant stress (creep) and the stress in the material relaxes under a constant deformation. If the imposed stress varies sinusoidally, the strain is neither exactly in phase with the stress (as for an elastic solid) nor 90^0 out of phase (viscous liquid) but is somewhere in between. Part of the energy is stored and recovered during each cycle, some is dissipated as heat. Materials that show this type of behaviour are called viscoelastic. If in a given experiment the ratio of stress to strain is solely a function of time (or frequency) and temperature, and not of stress magnitude, one speaks of linear viscoelasticity. It has been the subject of investigation for many researchers for decades (Alfrey, 1948; Fung, 1965; Flügge, 1975; Ferry, 1980).

The damping layer envisaged in the present investigations features viscoelastic material behaviour. The damping properties of this material are of interest as these can provide significant damping to the application, whereas the relatively low stiffness can ensure vibration isolation.
In the present study the vibration amplitude is assumed to be much smaller than the thickness of the viscoelastic layer, meaning that the material can be considered as being linear viscoelastic. Also, it is assumed to be isotropic and subject to isothermal conditions. Moreover, material ageing is not included. In general, viscoelastic behaviour is mainly governed by the deviatoric stresses and strains in the material (Ferry, 1980). Therefore, the bulk stiffness is assumed to be constant in this study.

As described above viscoelastic materials slowly deform with time under a constant stress, a phenomenon that is known as creep. In a bearing application the gravitational forces and the bearing preload brings the viscoelastic layer continuously under stress causing the material to creep. Clearly, this is an undesirable process and should be avoided at all times. It is therefore preferable to use rubber or vulcanised materials as contain strong cross-links. As a result, they have a better resistance against deformation by creep.

The dynamic behaviour of rolling bearings is governed by transient mechanisms, which can only be described in the time domain. To be able to predict the behaviour of a viscoelastic component in combination with bearings the constitutive equations for viscoelastic material and the equations of motion of the component also have to be described in the time domain. As experimental data for viscoelastic materials are usually obtained as a function of frequency it is important that the constitutive model can also be transformed into the frequency domain.
For modal and harmonic response analyses the viscoelastic material properties can be described via a complex modulus of elasticity. This method is justified by the so-called correspondence principle (Alfrey, 1948; Flügge, 1975), which states that once the solution to a linear elastic problem is known, the solution to the corresponding linear viscoelastic problem can be obtained by replacing the real modulus of elasticity by a complex one. In general, this complex modulus of elasticity is frequency dependent.

2.3.1 Stress and strain tensors

The Cauchy stress σ_{mn} is defined in the deformed state by prescribing equilibrium of an infinitesimal volume. It follows from the conservation of angular momentum of an infinitesimal volume that the Cauchy stress tensor is symmetric (first law of Cauchy):

$$\sigma_{mn} = \sigma_{nm} \tag{2.6}$$

By definition, the stress tensor σ_{mn} can be subdivided into a deviatoric stress tensor s_{mn}, of which the mean normal stress is zero, and a hydrostatic part σ_{kk}:

$$\sigma_{mn} = s_{mn} + \frac{1}{3}\sigma_{kk}\delta_{mn} \tag{2.7}$$

where δ_{mn} is the Kronecker delta. Subsequently, also the linear strain tensor ε_{mn} can be divided into a deviatoric and a hydrostatic part:

$$\varepsilon_{mn} = e_{mn} + \frac{1}{3}\varepsilon_{kk}\delta_{mn} \tag{2.8}$$

where e_{mn} and ε_{kk} denote the deviatoric and hydrostatic strain part, respectively. The relation between the stress and the strain tensor is described by Hooke's law:

$$\sigma_{mn} = 2Ge_{mn} + \frac{1}{3}K\varepsilon_{kk}\delta_{mn} \tag{2.9}$$

where $K = E/(3(1-2\nu))$ denotes the compression (or bulk) modulus, $G = E/(2(1+\nu))$ the shear modulus, E Young's modulus and ν Poisson's ratio.

2.3.2 Constitutive equations in the time domain

The convolution integral form is a general constitutive equation for linear viscoelastic material (Fung, 1965):

$$\sigma_{mn}(t) = \int_{-\infty}^{t} 2G_{rel}(t-t')\dot{\varepsilon}_{mn}(t')\mathrm{d}t' \tag{2.10}$$

where $G_{rel}(t)$ is the stress relaxation function. In case of a so-called Maxwell representation (Alfrey, 1948; Ferry, 1980) this function can be written as a series of exponential functions, reading:

$$G_{rel}(t) = G_0 + \sum_{i=1}^{N} G_i \exp\left(-\frac{t}{\tau_i}\right) \tag{2.11}$$

Here G_0 is the instantaneous modulus of the material whereas G_i and $\tau_i = \eta_i/G_i$ are the relaxation strength and relaxation time corresponding to the i-th dissipative mechanism. N is the total number of dissipative mechanisms. The time dependence of G_{rel} can be interpreted mechanically by a sufficient number of elastic and viscous elements. For example, the generalised Maxwell model consists of a number of parallel connected spring-dashpot systems, a parallel spring and a parallel damper (Figure 2.5) for which the relaxation modulus matches equation 2.11. It is assumed that time dependent behaviour for viscoelastic materials is only present in the

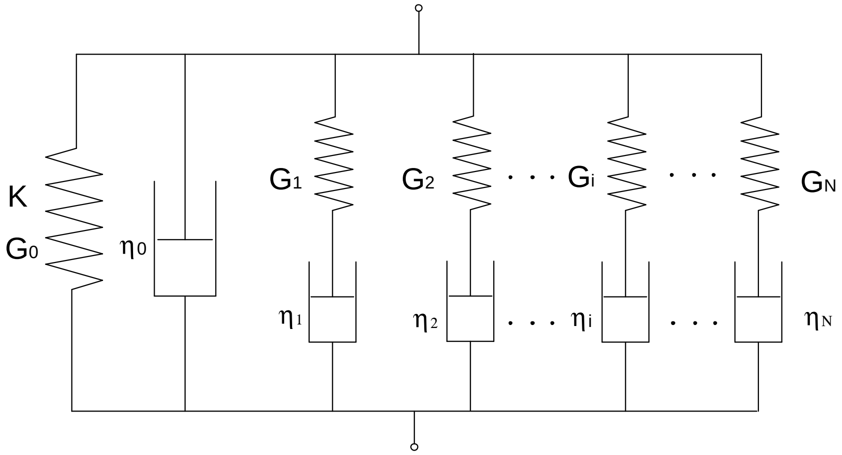

Figure 2.5: *The generalised Maxwell model.*

deviatoric direction. Therefore, the compression modulus is assumed to be constant and is defined by a single parameter K.

The advantage of the Maxwell model is that the dynamic behaviour can be described efficiently in both the time and frequency domain.

Let us assume a generalised Maxwell model, as presented in Figure 2.5. The constitutive equation can then be expressed as:

$$\sigma_{mn}(t) = \frac{1}{3}K\varepsilon_{kk}(t)\delta_{mn} + 2G_0 e_{mn}(t) + 2\eta_0 \dot{e}_{mn}(t) + \\ + \sum_{i=1}^{N} \int_{-\infty}^{t} 2G_i \exp\left(\frac{t'-t}{\tau_i}\right) \dot{e}_{mn}(t')\mathrm{d}t' \qquad (2.12)$$

where G_0 is the shear modulus of the parallel spring and G_i and τ_i the shear modulus and relaxation time of the i-th Maxwell element which is defined as a spring and a dashpot in series. The damping coefficient of the parallel dashpot is represented by η_0. Note that for the remaining dashpots the damping coefficients are denoted as η_i.

The convolution integral represents a sum of the present strain rate and the historical strain rates of the material. For $t < 0$ the material is assumed to be at rest, so the lower boundary of the integral is set to $t = 0$. The convolution integral can be discretised with time step $\Delta t = t^{p+1} - t^p$ according to Baaijens (1991):

$$\sigma_{mn}^{p+1} = \frac{1}{3}K\varepsilon_{kk}^{p+1}\delta_{mn} + 2G_0 e_{mn}^{p+1} + 2\eta_0 \dot{e}_{mn}^{p+1} + \\ + \sum_{i=1}^{N} \int\limits_{0}^{t^{p+1}} 2G_i \exp\left(\frac{t' - t^{p+1}}{\tau_i}\right) \dot{e}_{mn}(t')\mathrm{d}t' \tag{2.13}$$

By using the relation $\exp\left(-t^{p+1}/\tau\right) = \exp\left(-\Delta t/\tau\right)\exp\left(-t^{p}/\tau\right)$ and assuming a piecewise linear rate of deformation $\dot{e}_{mn}$, the integral can be solved and the resulting constitutive equation yields:

$$\sigma_{mn}^{p+1} = \frac{1}{3}K\varepsilon_{kk}^{p+1}\delta_{mn} + 2G_0 e_{mn}^{p+1} + 2\eta_0 \dot{e}_{mn}^{p+1} + \\ +2\sum_{i=1}^{N} \hat{\eta}_i \dot{e}_{mn}^{p+1} + \sum_{i=1}^{N} \mathcal{H}_{mn_i}^{p+1} \tag{2.14}$$

where

$$\hat{\eta}_i = \tau_i G_i \frac{\Delta t - \tau_i(1 - \exp\left(-\Delta t/\tau_i\right))}{\Delta t} \tag{2.15}$$

$$\mathcal{H}_{mn_i}^{p+1} = 2\tau_i G_i (1 - \exp\left(-\Delta t/\tau_i\right)) \times \\ \times (1 - \frac{\Delta t - \tau_i(1 - \exp\left(-\Delta t/\tau_i\right))}{\Delta t}) \dot{e}_{mn}^{p} + \exp\left(-\Delta t/\tau_i\right)\mathcal{H}_{mn_i}^{p} \tag{2.16}$$

The tensor $\mathcal{H}_{mn_i}^{p+1}$ is called the *history* tensor, since it contains the strain rates from the past ($t < t^{p+1}$).
Equation 2.14 is the discretised constitutive equation for a generalised Maxwell model giving the relation between stresses and strains as a function of time. A stiffness term, a damping term and a history term can be recognized. It is an advantage that the equation is written in a convenient form, i.e. the history tensor is linearly dependent on the strain rate and the history tensor of the previous time step only. This is in contrast with some formulations for which the history term is dependent on all previous time steps. For the Maxwell formulation the computation time therefore remains relatively short.

It should be added that another, more recently developed formulation for viscoelasticity is the so-called fractional derivative model (Bagley and Torvik, 1983; Enelund and Olsson, 1997). In this method stress relaxation in polymers is described by fractional order derivatives. As a consequence, the number of parameters required to describe viscoelastic material properties is, in general, less than for the Maxwell model.

A third formulation of viscoelasticity in the time domain has been developed by Lesieutre and Mingori (1990). In their formulation so-called augmented thermodynamic fields (ATF) are introduced that interact with the usual mechanical displacement field. This approach is based on the fact that viscoelastic material damping involves the transfer of energy and is therefore fundamentally a thermodynamic phenomenon. The ATF method, however, was limited to one-dimensional stress states only. More recently, the approach was generalised to three-dimensional states, in which the total displacement field is subdivided into an elastic and an anelastic displacement field (ADF) (Lesieutre and Bianchini, 1995). This method is closely related to the one introduced by Dovstam (1995), who employs the augmented Hooke's law to describe three-dimensional material damping. These methods are mentioned for the sake of completeness, but they are beyond the scope of the present investigation.

The transformation matrices $[T_1]$ and $[T_2]$ are introduced to relate the hydrostatic and deviatoric part of a tensor with the strain vector $\{\varepsilon\}$, respectively.

$$\frac{1}{3}\varepsilon_{kk}\delta_{mn} \equiv [T_1]\{\varepsilon\} \tag{2.17}$$

$$e_{mn} \equiv [T_2]\{\varepsilon\} \tag{2.18}$$

Consequently, equation 2.14 can be put into the following matrix notation:

$$\{\sigma\}^{p+1} = [E]\{\varepsilon\}^{p+1} + [D]\{\dot{\varepsilon}\}^{p+1} + \{\mathcal{H}\}^{p+1} \tag{2.19}$$

where $[E]$ is the elastic material matrix and $[D]$ the viscous material matrix:

$$[E] = K[T_1] + 2G_0[T_2] \qquad [D] = 2(\eta_0 + \sum_{i=1}^{N} \hat{\eta}_i)[T_2] \tag{2.20}$$

The history vector $\{\mathcal{H}\}^{p+1}$ is defined as:

$$\begin{aligned} \{\mathcal{H}\}^{p+1} &= 2\tau_i G_i(1 - \exp(-\Delta t/\tau_i)) \times \\ \times(1 - \frac{\Delta t - \tau_i(1 - \exp(-\Delta t/\tau_i))}{\Delta t})&\{\dot{\varepsilon}\}^p + \exp(-\Delta t/\tau_i)\{\mathcal{H}\}^p \end{aligned} \tag{2.21}$$

2.3.3 Equations of motion

The equations of motion are derived using the procedure of weighting and Galerkin's method in combination with the constitutive equation. A vector $\{x\}$ is introduced containing the generalised coordinates. A standard finite element approach is applied, in which $[N]$ is the matrix with the shape functions relating the displacements $\{u\}$ to the generalised coordinates $\{x\}$ and $[B]$ the matrix that relates the strain vector $\{\varepsilon\}$ to $\{x\}$.
The resulting equations of motion for a viscoelastic component read:

$$[M_{ve}]\{\ddot{x}\}^{p+1}+[C_{ve}]\{\dot{x}\}^{p+1}+[K_{ve}]\{x\}^{p+1}=\{F\}-[H_{ve}]\{h\}^{p+1} \tag{2.22}$$

where $[M_{ve}]$ is the mass matrix, $[C_{ve}]$ the damping matrix and $[K_{ve}]$ the stiffness matrix of the viscoelastic layer. The vector $\{F\}$ contains the externally applied forces and $[H_{ve}]\{h\}^{p+1}$ the history forces. Because of this characteristic, $[H_{ve}]$ is called the history matrix. The different matrices are defined as follows:

$$[M_{ve}]=\int_V \rho[N]^T[N]\mathrm{dV} \tag{2.23}$$

$$[C_{ve}]=\int_V [B]^T[D][B]\mathrm{dV} \tag{2.24}$$

$$[K_{ve}]=\int_V [B]^T[E][B]\mathrm{dV} \tag{2.25}$$

$$[H_{ve}]=\int_V [B]^T[T_2][B]\mathrm{dV} \tag{2.26}$$

where ρ is the material density. The vector $\{h\}^{p+1}$ corresponds with equation 2.21, but this time expressed in the generalised coordinates $\{x\}$, i.e. in terms of the previous velocity vector $\{\dot{x}\}^p$ instead of the previous strain rate $\dot{e}_{mn}^p$:

$$\begin{aligned}\{h\}^{p+1} &= 2\tau_i G_i(1-\exp(-\Delta t/\tau_i))\times\\ \times(1-\frac{\Delta t-\tau_i(1-\exp(-\Delta t/\tau_i))}{\Delta t})&\{\dot{x}\}^p+\exp(-\Delta t/\tau_i)\{h\}^p\end{aligned} \tag{2.27}$$

2.3.4 Constitutive equations in the frequency domain

By writing the shear strain e_{mn} as a complex periodic function, one obtains the complex dynamic (shear) modulus G_d in the frequency domain:

$$\lim_{t\to\infty}\frac{s_{mn}(t)}{2e_{mn}(t)}=G_d(\omega)=G'(\omega)+\jmath G''(\omega)\ ,\quad m\neq n,\quad 2e_{mn}(t)=\exp(\jmath\omega t) \tag{2.28}$$

where $\jmath=\sqrt{-1}$ is the imaginary unit, ω the angular frequency. $G'(\omega)$ is called the storage modulus and $G''(\omega)$ the dissipation or loss modulus. The loss factor η is defined as the ratio between the loss modulus and the storage modulus :

$$\eta(\omega) = \frac{G''(\omega)}{G'(\omega)} \tag{2.29}$$

The way in which the Maxwell model is transformed from the time domain to the frequency domain is demonstrated for a single Maxwell element. This can easily be extended to several Maxwell elements. The constitutive relation in shear deformation for a single Maxwell element (with properties G_i and τ_i) is:

$$s_{mn}(t) = 2G_i \int_0^t \exp\left(\frac{t'-t}{\tau_i}\right) \dot{e}_{mn}(t')\mathrm{d}t' \tag{2.30}$$

Substitution into equation 2.28 gives the complex dynamic modulus G_d for this Maxwell element:

$$G_d(\omega) = \lim_{t\to\infty} G_i \int_0^t \jmath\omega \exp\left((\jmath\omega + \frac{1}{\tau_i})(t'-t)\right)\mathrm{d}t' = G_i \frac{\jmath\omega\tau_i}{1+\jmath\omega\tau_i} \tag{2.31}$$

Next, the storage and dissipation modulus of the Maxwell element can be written as:

$$G'(\omega) = \frac{(\omega\tau_i)^2}{1+(\omega\tau_i)^2} G_i \tag{2.32}$$

$$G''(\omega) = \frac{\omega\tau_i}{1+(\omega\tau_i)^2} G_i \tag{2.33}$$

For the generalised Maxwell model with N elements, a parallel spring and a parallel dashpot, the storage and dissipation moduli are given by:

$$G'(\omega) = G_0 + \sum_{i=1}^{N} \frac{(\omega\tau_i)^2}{1+(\omega\tau_i)^2} G_i \tag{2.34}$$

$$G''(\omega) = \omega\eta_0 + \sum_{i=1}^{N} \frac{\omega\tau_i}{1+(\omega\tau_i)^2} G_i \tag{2.35}$$

Note that the dissipation modulus of the parallel dashpot is a linear function of the frequency.

In chapter 3 it is shown how experimentally obtained material data are approximated by the generalised Maxwell representation.

2.4 Component Mode Synthesis

Frequently the size of a mathematical model of a dynamic problem has to be reduced considerably to obtain acceptable turn-around times of the computations. A well known way to limit the amount of computational effort is the application of the Ritz method, for example, where the displacement field of a structure is described by a series of admissible shape functions in order to reduce the number of degrees of freedom (DOFs) of the finite element model. When the structure contains a number of components which are described by the Ritz method, one can speak of a *component mode synthesis* (CMS).
In a bearing application the shaft, the housing, the bearing outer ring and the viscoelastic layer can be modelled with a CMS technique. For the shaft and the housing a standard method can be applied, whereas for the bearing outer ring a new CMS method has been developed. The latter method includes the effect of rotating contact loads (Wensing, 1998a; Wensing and Nijen, 2001). The shape functions applied in this method are very well-suited for the description of flexible interfaces. Therefore, these functions are also introduced to reduce the model for flexible viscoelastic components.

Let us e.g. consider the equations of motion of a (FEM) component:

$$[M]\{\ddot{x}\} + [C]\{\dot{x}\} + [K]\{x\} = \{F\} \tag{2.36}$$

where $[M]$ is the mass matrix, $[C]$ the damping matrix, $[K]$ the stiffness matrix and $\{F\}$ the vector containing the externally applied forces. The displacements of the component are written as a linear combination of suitable shape functions:

$$\{x\} = [\Psi]\{p\} \tag{2.37}$$

where the vector $\{p\}$ contains the generalised DOFs. It is emphasized that the number of generalised DOFs is much smaller than the number of (FEM) DOFs in the vector $\{x\}$. Substitution of equation 2.37 into 2.36 and premultiplication with $[\Psi]^T$ yields:

$$[m]\{\ddot{p}\} + [c]\{\dot{p}\} + [k]\{p\} = \{f\} \tag{2.38}$$

with the following reduced matrices:

$$[m] = [\Psi]^T[M][\Psi] \qquad [c] = [\Psi]^T[C][\Psi] \qquad [k] = [\Psi]^T[K][\Psi] \tag{2.39}$$

and the applied forces $\{f\} = [\Psi]^T\{F\}$. From the solution of the reduced set of equations of motion, the displacements of the original system can be found by backsubstitution into equation 2.37.

2.4.1 CMS for a general component

Frequently the component mode synthesis is very suitable for complex mechanical systems, because the structure can be subdivided into a number of logical components. The components are connected to each other by interfaces, which can either be rigid or flexible. The essence of CMS is that one chooses a minimum set of shape functions or component modes that accurately describes the dynamic behaviour of the system in the frequency range of interest. If necessary the set of component modes should be able to describe the static solution in order to account for the effect of interface loads caused by adjacent components. If applicable, the component mode set should also account for rigid body motions. For an easy coupling of the component models the vector with the generalised DOFs of each component must explicitly contain the DOFs of the interfaces.

In general, the component mode set consists of static and dynamic modes. Several techniques have been developed to find suitable component modes. For more details about this subject the reader is referred to the overview given by Wensing (1998a).
In the present study we employ the so-called fixed interface method, because it enables an easy computation of the component modes with a commercial finite element package. In this method the interface DOFs are constrained while calculating the static and dynamic component modes (Craig and Bampton, 1968). The number of static modes is governed by the number of interface DOFs of the component. The number of dynamic modes depends on the frequency range of interest.

The fixed interface method can easily be understood by considering a simple beam with two components A and B, which are connected through an interface node with one translational DOF x_b and one rotational DOF φ_b (Figure 2.6a).
For each component one has to determine a set of constraint modes (or static modes) and a set of fixed interface normal modes (dynamic modes). The constraint modes are obtained by giving one interface DOF a unitary displacement or rotation while keeping the other interface DOFs suppressed. The first and second constraint mode of the beam example are shown in

Figures 2.6b and 2.6c. In Figure 2.6d the first dynamic mode with fixed interface DOF is shown.

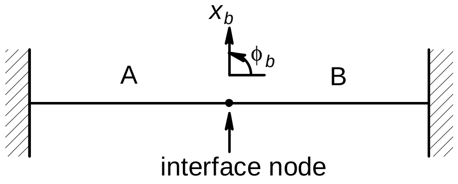

(a): Structure consisting of two beam components.

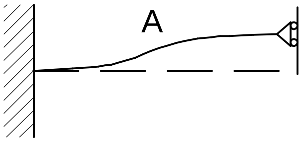

(b): First constraint mode with x_b*=1 and* φ_b*=0.*

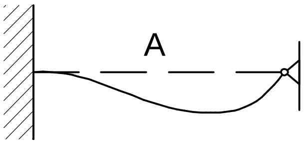

(c): Second constraint mode with x_b*=0 and* φ_b*=1.*

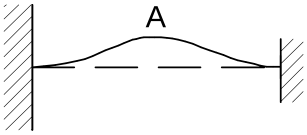

(d): First fixed normal mode with x_b*=0 and* φ_b*=0.*

Figure 2.6: *Constraint modes and fixed interface normal modes of a simple beam.*

The constraint modes are obtained via a static analysis, while the fixed interface normal modes can be calculated by means of a modal analysis. In the present study all component modes are computed with the finite element package ANSYS.

In the structures considered in the present study the interfaces between the components contain a large number of nodes. This makes the conventional

CMS method less effective, because it is based on a small number of nodes at the interfaces. To avoid this problem we select a set of component modes, suited to describe the static and dynamic behaviour of components with interface areas containing many nodes. A distinction is made between rigid and flexible interface areas, as illustrated in Figure 2.7.

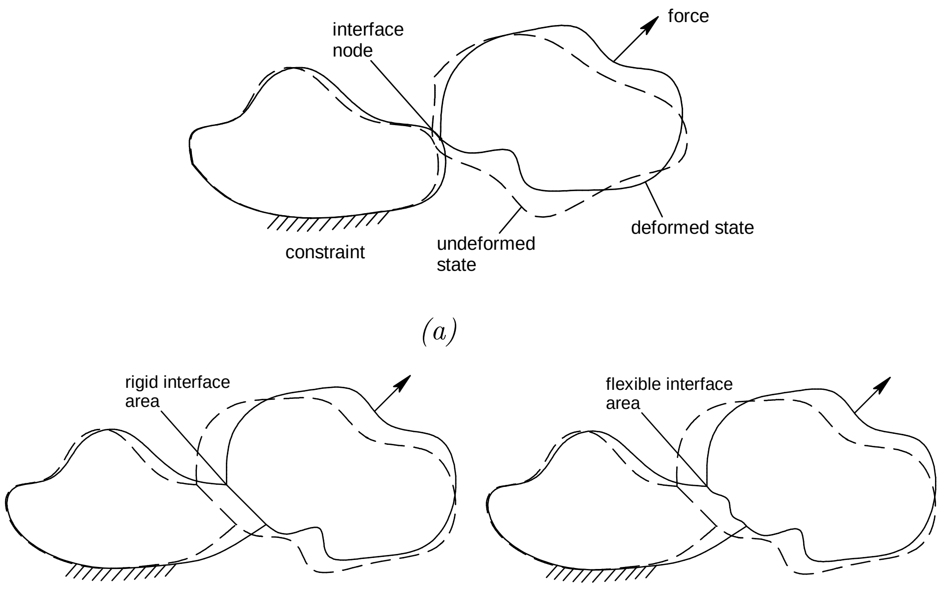

(a)

(b) *(c)*

Figure 2.7: *Illustration of (a) an interface node, (b) a rigid interface area and (c) a flexible interface area.*

In the case of a rigid interface area, the displacement of each interface node is rigidly connected to a reference node having six degrees of freedom, i.e. three translations and three rotations. In case of a flexible interface area, the displacements of the surface are described by analytical series including both rolling bearing motion and deformations of the interface. This will be described in more detail in section 2.4.3.

2.4.2 CMS for a viscoelastic component

The use of undamped modes in CMS is most efficient for components which are undamped, slightly damped or proportionally damped. In general, viscoelastic components are non-proportionally damped and in many cases highly damped. Therefore, the conventional CMS method cannot be applied to a viscoelastic FEM component. In order to deal with complex geometries and flexible interfaces, however, it is desired that a viscoelastic component can be modelled with FEM. Therefore, a new CMS method is developed in which the viscoelastic properties of a material are accounted for.

Let us consider a viscoelastic layer that is modelled with the finite element method. The equations of motion of the viscoelastic layer were found to be:

$$[M_{ve}]\{\ddot{x}\} + [C_{ve}]\{\dot{x}\} + [K_{ve}]\{x\} = \{F\} - [H_{ve}]\{h_x\} \tag{2.40}$$

If the static and dynamic behaviour of the viscoelastic layer can be described by a number of suitable mode shapes, the model can be reduced according to the CMS technique. The modes are stored column-wise in the reduction matrix $[\Psi]$. Next, the reduced matrices are obtained from equation 2.39:

$$[m_{ve}] = [\Psi]^T[M_{ve}][\Psi] \qquad [c_{ve}] = [\Psi]^T[C_{ve}][\Psi] \qquad [k_{ve}] = [\Psi]^T[K_{ve}][\Psi] \tag{2.41}$$

and similarly the applied forces $\{f\} = [\Psi]^T\{F\}$. Also the reduced history matrix can be obtained from the relation $[h_{ve}] = [\Psi]^T[H_{ve}][\Psi]$, because the vector $\{h_x\}$ is a linear combination of the degrees of freedom (see appendix A).

For viscoelastic structures the assumption of proportional damping does not apply. Therefore, the matrices $[C_{ve}]$ and $[H_{ve}]$ can not directly be derived from the stiffness matrix $[K_{ve}]$ as calculated by a commercial FEM package such as ANSYS.
However, it can be observed from equations 2.24, 2.26 and 2.20 that the system damping matrix $[C_{ve}]$ and the history matrix $[H_{ve}]$ are proportional to the deviatoric part of the stiffness matrix $[K_{ve}]_{dev}$. The deviatoric stiffness matrix is obtained by setting the compression modulus K to zero:

$$[K_{ve}]_{dev} = 2G_0 \int_V [B]^T[T_2][B]\mathrm{dV} \tag{2.42}$$

The damping and history matrices can thus directly be derived from the deviatoric stiffness matrix:

$$[C_{ve}] = \frac{\left(\eta_0 + \sum\limits_{i=1}^{N} \hat{\eta}_i\right)}{G_0}[K_{ve}]_{dev} \tag{2.43}$$

$$[H_{ve}] = \frac{1}{2G_0}[K_{ve}]_{dev} \tag{2.44}$$

The deviatoric part of the stiffness matrix is obtained in a FEM package by setting the compression modulus to zero or close to zero in order to avoid a singular stiffness matrix. Next, the reduced damping and history matrices are calculated with the original set of modes:

$$[c_{ve}] = [\Psi]^T[C_{ve}][\Psi] = \frac{\eta_0 + \sum\limits_{i=1}^{N} \hat{\eta}_i}{G_0}[\Psi]^T[K_{ve}]_{dev}[\Psi] \tag{2.45}$$

$$[h_{ve}] = [\Psi]^T[H_{ve}][\Psi] = \frac{1}{2G_0}[\Psi]^T[K_{ve}]_{dev}[\Psi] \tag{2.46}$$

The result is a set of reduced matrices which are put into a new set of equations of motion:

$$[m_{ve}]\{\ddot{p}\} + [c_{ve}]\{\dot{p}\} + [k_{ve}]\{p\} = \{f\} - [h_{ve}]\{h_p\} \tag{2.47}$$

where $\{h_p\}$ is a vector based on the generalised DOF $\{p\}$.

The reduced matrices have to be based on a set of suitable mode shapes that describe the dynamic and static behaviour of the component. In the case of a viscoelastic component the use of undamped modes may not be sufficient for an accurate description as the component is non-proportionally and highly damped. For thin layers, however, the mode shapes are not expected to be dependent on damping. In fact, it is assumed that the dynamic behaviour of the layer can be described with only a static mode set for the component interfaces, which can either be rigid or flexible. Due to the small mass of a thin layer, the use of dynamic modes is considered redundant. These assumptions are justified in section 2.4.4.

2.4.3 Flexible interfaces

When flexibility of the interfaces has to be incorporated, constraint modes have to be determined for each DOF on the interface, thus resulting in a highly inefficient reduction. A more efficient CMS reduction can be obtained by defining smooth global functions that describe the deformation of the interface surface. This approach was also adopted to model flexible bearing outer rings, in which the problem of a moving interface load (by the rolling elements) is addressed (Wensing, 1998a).

For the description of the radial and axial displacement of a flexible interface, Fourier series are used in the circumferential direction. In the radial and axial directions Chebyshev polynomials are applied. For the geometry of a viscoelastic layer surface (Figure 2.8) these functions can also be used.

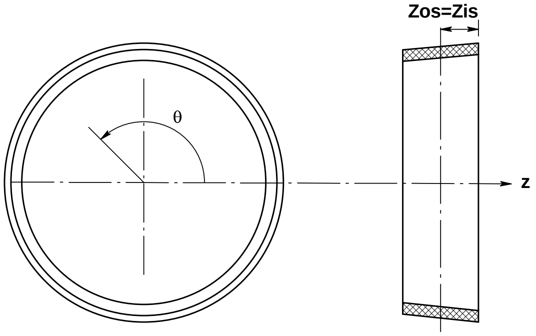

Figure 2.8: *Geometry of a viscoelastic layer.*

The radial (u_r), axial (u_z) and the tangential displacements (u_t) are described by analytical series. The displacements for a flexible outer surface (using the index *os*) can be expressed as:

$$\begin{aligned} u_r^{os} &= \sum_{n=0}^{N_r} \sum_{m=0}^{M_r} a_r(t)\cos(n\theta)\cos(m\arccos(\frac{z}{Z_{os}})) + \\ &+ \sum_{n=1}^{N_r} \sum_{m=0}^{M_r} b_r(t)\sin(n\theta)\cos(m\arccos(\frac{z}{Z_{os}})) \end{aligned} \tag{2.48}$$

$$\begin{aligned} u_z^{os} &= \sum_{n=0}^{N_z} \sum_{m=0}^{M_z} a_z(t)\cos(n\theta)\cos(m\arccos(\frac{z}{Z_{os}})) + \\ &+ \sum_{n=1}^{N_z} \sum_{m=0}^{M_z} b_z(t)\sin(n\theta)\cos(m\arccos(\frac{z}{Z_{os}})) \end{aligned} \tag{2.49}$$

$$\begin{aligned} u_t^{os} &= \sum_{n=0}^{N_t} \sum_{m=0}^{M_t} a_t(t)\cos(n\theta)\cos(m\arccos(\frac{z}{Z_{os}})) + \\ &+ \sum_{n=1}^{N_t} \sum_{m=0}^{M_t} b_z(t)\sin(n\theta)\cos(m\arccos(\frac{z}{Z_{os}})) \end{aligned} \tag{2.50}$$

where a_r, b_r, a_z, b_z, a_t and b_t denote the new set of interface DOF of the model, i.e

$$\{x_b\}^T = \{\{a_r\}^T, \{b_r\}^T, \{a_z\}^T, \{b_z\}^T, \{a_t\}^T, \{b_t\}^T\} \tag{2.51}$$

Note that the index *os* can be replaced by *is* to describe the inner surface of the layer.

By prescribing a displacement field of unit amplitude in one of the generalised interface DOFs, while suppressing all other interface DOFs, a global constraint mode can be obtained. Each term in the series provides one constraint mode. Rigid body motions are also accounted for. As an example, some characteristic radial and axial displacements of a viscoelastic layer are shown in Figure 2.9.

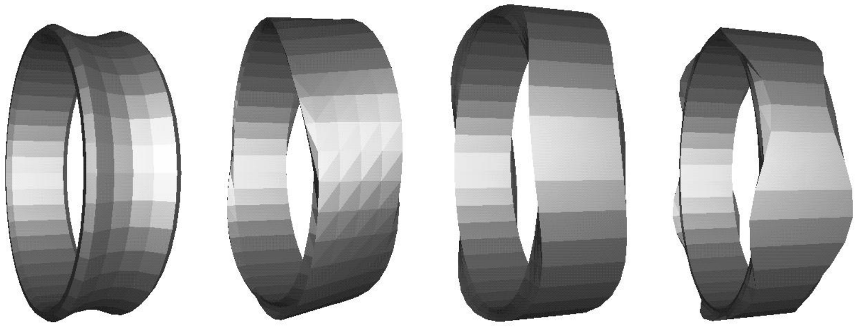

(a) (b) (c) (d)

Figure 2.9: *Radial displacement for (a) n=0 and m=2 and (b) n=2 and m=1 and the axial displacement of a layer for (c) n=3 and m=0 and (d) n=5 and m=1.*

The performance of this new CMS method for flexible interfaces has been demonstrated by Wensing (1998a) who showed that the same modelling accuracy can be achieved as in classical CMS methods.
The flexible interface approach is applied only in Chapter 3 for the validation of the viscoelastic model. In the case of a rolling bearing application, the interfaces of the viscoelastic component are assumed to be rigid.

2.4.4 Numerical validation of the new CMS method

The finite element model of a viscoelastic layer as shown in Figure 2.10 is used to validate the CMS method as described in the previous section. The

full model consists of 360 solid quadratic elements. The interface areas of this model are at the inner and outer bores and are assumed rigid.
The component mode set for the model reduction consists of three translational and three rotational DOFs for both the inner and outer interfaces. As a result, the total number of constraint modes equals 12. As no inertial effects of the layer are considered, the FEM model of the viscoelastic layer is reduced from 6720 DOFs to 12 generalised DOFs.

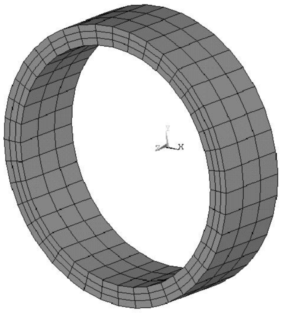

Figure 2.10: *Finite element model of a viscoelastic layer.*

The geometry of this layer is chosen to fit around a regular size deep groove ball bearing, i.e. a layer with an inner diameter of 35 mm and a width of 11 mm. The thickness of the layer is 3.0 mm. The material, which is representative for rubbers, is assigned a bulk modulus K of 3500 MPa, a static shear modulus G_0 of 1.0 MPa and a single Maxwell element with properties $G_1 = 10$ MPa and $\eta_1 = 1000$ Ns/m^2. The material density ρ is set to 1000 kg/m^3. An assembly model is considered consisting of the viscoelastic layer extended with a rigid ring mounted around the outer interface of the layer. This rigid ring has a mass of 50 g and mass moments of inertia $I_{xx} = I_{yy} = 5 \cdot 10^{-5}$ kgm^2 and $I_{zz} = 1 \cdot 10^{-4}$ kgm^2.

To numerically validate the new CMS method for viscoelastic components, the results of a full FEM model are compared with those of the reduced CMS model. A transient dynamic analysis is performed as it is the only possible analysis in the FEM package ANSYS for a model with viscoelastic properties. For the numerical analyses the inner bore is fixed in all directions, whereas the outer surface of the layer and the adjacent rigid ring is free to move. A 100 N (ramped) impact force is applied during $4 \cdot 10^{-5}$ s to the (rigid) outer ring simultaneously in the radial, axial, tilt and circumferential directions, see Figure 2.11. The response signals are presented in

Figure 2.12.

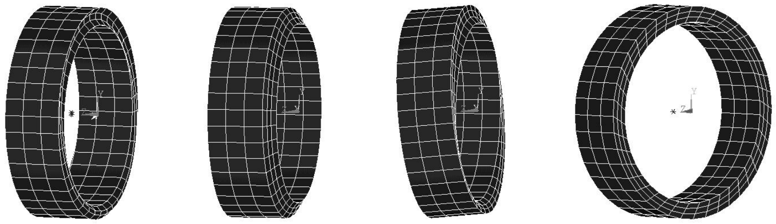

(a) (b) (c) (d)

Figure 2.11: *(a) Radial, (b) axial, (c) tilt and (d) torsional mode.*

A good agreement is obtained between the full FEM model and the reduced CMS model. Only for the radial response signal a small deviation is observed. This is attributed to the dynamic effect across the layer thickness which cannot be described by the static modes used for the CMS model. It is noted that the computation time on an ordinary workstation for the full model is approximately 16 hours, and for the reduced model about 6 seconds.

The analysis was repeated for different values of η_1, but no significant differences between the full and the reduced model were found. It is noted that Figure 2.12 already shows an overcritically damped axial response.

In addition, a variation in layer thickness was investigated. It was found that up to a layer thickness of at least 75 mm no large deviations were observed. For very thin layers, however, a numerical limitation is reached. In that case it appears very difficult to mesh the model with solid finite elements. In the present example, the model could be meshed for a layer with a thickness from about 0.1 mm.

It can be concluded that for (thin and meshable) viscoelastic supports the dynamic behaviour can be described sufficiently accurate with the use of static modes, even for high damping values. This justifies the application of the presented CMS technique for such components.

2.5 Modelling procedure for applications

The way in which the methods described so far were used in the modelling procedure of applications is addressed in this section. The model of a complete bearing application is constructed by combining the models of each component. In Figure 2.13 a model of a rotor dynamic application

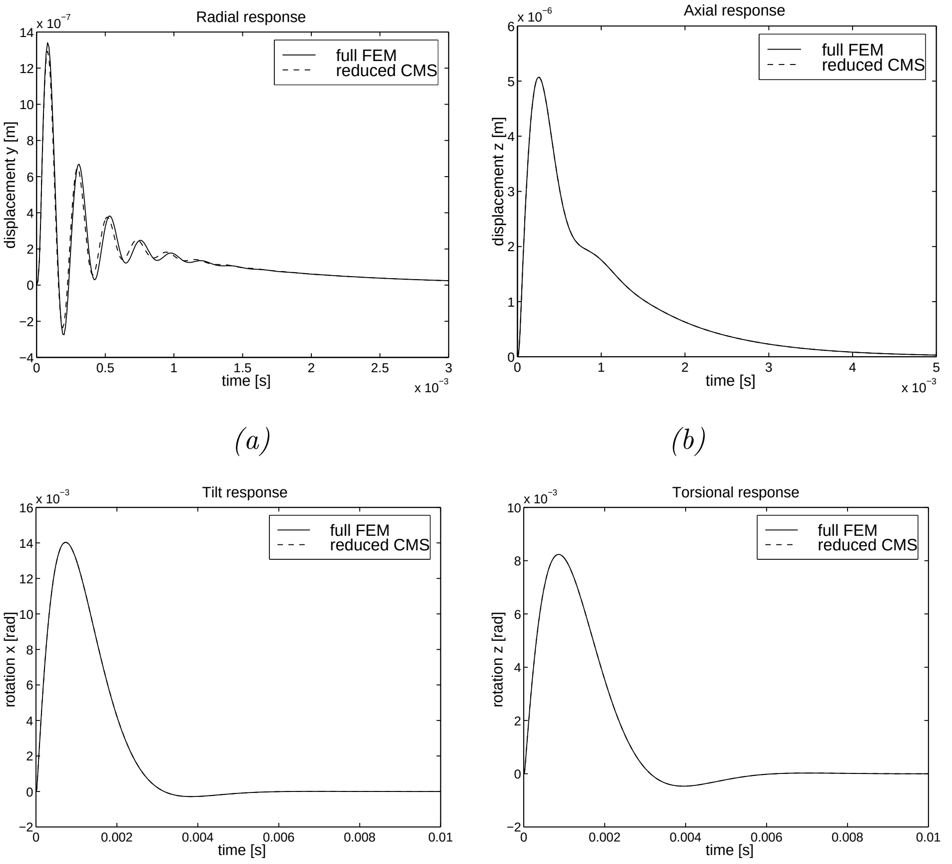

(a) *(b)*

(c) *(d)*

Figure 2.12: *Response signals of a viscoelastic layer under an impact load in the (a) radial, (b) axial, (c) tilt and (d) circumferential directions.*

with ball bearings is presented. This model consists of a flexible shaft supported by two identical deep groove ball bearings in a viscoelastic support mounted in flexible housings. In Tillema (2001) some results of this application model have been addressed.

In the present investigations, the bearing inner and outer rings as well as the interfaces of the viscoelastic layer in a rotor dynamics application are considered as being rigid. The contact model presented in Section 2.2 is used to couple the rotating inner rings to the bearing outer rings. To ensure full contact of the rolling elements with the raceway the bearing application is axially pre-loaded so that one of the bearing outer rings can move freely

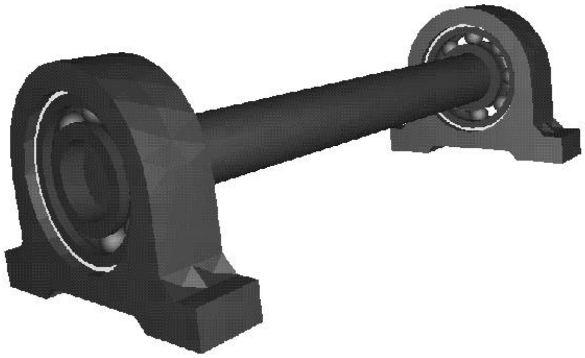

Figure 2.13: *Rotor dynamic application model with viscoelastic bearing supports.*

in the axial direction.

The shaft and the housings are modelled with a standard finite element method and are reduced according to the conventional component mode synthesis. The viscoelastic bearing support is also modelled with FEM, but then reduced according to the new CMS technique.

The equations of motion of the complete system consisting of the shaft, the housings, the bearings and the viscoelastic layer are written in matrix notation:

$$[m]\{\ddot{p}\} + [c]\{\dot{p}\} + [k]\{p\} = \{R\} - \{F(p, \dot{p}, t)\} - \{H(t)\} \tag{2.52}$$

where the mass matrix $[m]$, the damping matrix $[c]$ and the stiffness matrix $[k]$ are determined beforehand using CMS. The nonlinear and time dependent bearing contact forces are stored in the vector $\{F(p, \dot{p}, t)\}$, whereas the vector $\{H(t)\}$ contains the load history of the viscoelastic components. In $\{R\}$ the external forces are stored.

First, the static solution is determined, i.e. the displacements of the system as a result of the externally applied forces. Due to the non-linearity of the bearing springs and the bearing geometry the analysis is performed with a Newton-Raphson iteration process. A linearised stiffness matrix is obtained from the static solution. For a transient dynamic analysis the nonlinear equations of motion are numerically integrated with the Newmark method, based on a constant-average acceleration scheme (Bathe, 1982). A modified Newton-Raphson iteration is then used to solve the set of nonlinear equations.

In order to perform accurate modal and harmonic response analyses, the frequency dependent stiffness and damping properties of the viscoelastic layer are incorporated. For a modal analysis the following set of equations is solved iteratively:

$$-\omega^2[m]\{p\} + [k(\omega)]\{p\} = \{0\} \tag{2.53}$$

The frequency dependent eigensolver finds the requested number of eigenfrequencies of the system. First, all eigenfrequencies of the system are solved with a constant stiffness matrix. The calculated eigenfrequencies are then used as an estimate starting frequency for the next iteration. Equation 2.53 is solved repetitively until the difference between two consecutive iterations for a certain eigenfrequency is smaller than a certain cut-off value ϵ. When an eigenfrequency has converged it is saved and the next eigenfrequency is searched for. It should be recalled that the undamped eigenfrequencies are calculated.

For a harmonic response analysis equation 2.54 is evaluated for the required frequency range.

$$-\omega^2[m]\{p\} + \jmath\omega[c]\{p\} + ([k(\omega)] + \jmath\eta(\omega)[k_{ve}(\omega)]_{dev})\{p\} = \{F\} \tag{2.54}$$

Note that both the stiffness matrices and the loss factor η are frequency dependent. The vector $\{p\}$ in this case is complex.

2.6 Summary and concluding remarks

A rolling bearing model has been presented, covering both vibration transmission and vibration generation aspects. This bearing model consists of a rigid inner and outer ring, whereas the rolling elements are considered massless. For each ball-raceway contact a nonlinear Hertzian spring and a linear dashpot are used. Bearing excitation by form deviations (waviness) is not analysed.

The constitutive behaviour for linear viscoelasticity has been derived in a discretised form. It is based on a generalised Maxwell model in order to facilitate the derivation in both the time and frequency domain. The equations of motion were derived using a standard finite element approach and are written in a convenient linearised form using the exponentially decaying *history* vector. With this method, transient dynamic calculations can be performed relatively quickly.

The linear equations of motion for a viscoelastic component are suited for the usage of the component mode synthesis. A key feature in this new approach is that the damping and history matrices are proportional to the deviatoric part of the stiffness matrix. The reduction of a thin layer FEM component is based on a transformation matrix containing only the static mode set for the component interfaces, which can either be rigid or flexible. Due to the small mass of a thin layer, the use of dynamic modes was considered redundant. This modelling approach was numerically validated by comparing the results of a full FEM model with those of the reduced model. It was shown that the agreement between the reduced model and the full model was very good, even for high damping values of the viscoelastic layer.

Chapter 3

Experimental investigation of viscoelastic materials and components

3.1 Introduction

The properties of viscoelastic material are strongly dependent on frequency, temperature and age. Usually, material properties such as the shear modulus and the loss factor are neither supplied by the manufacturer, nor listed in standardised tables. Therefore, one part of the present investigation focuses on the experimental determination of the frequency and temperature dependent stiffness and damping properties of some of the applied viscoelastic materials (section 3.2). For this purpose, measurements were carried out on a so-called Dynamic Mechanical Analyzer (DMA). The measured material properties were used in combination with the Time-Temperature Superposition (TTS) principle to extract material data over a wide frequency range. Subsequently, the frequency dependent shear modulus and loss factor were curve fitted with the Maxwell model parameters.

One of the aims of this study is the experimental validation of the modelling procedure for viscoelastic components as was presented in Chapter 2. For this purpose, several ring samples with a constrained viscoelastic layer were manufactured. Apart from the geometry also the material of the samples was varied, for which two different manufacturing methods were used. The frequency response functions of the samples were experimentally determined and compared with the predicted values (section 3.3).

3.2 Determination of viscoelastic material properties

3.2.1 Test on the Dynamic Mechanical Analyzer

The Dynamic Mechanical Analyzer is a force controlled instrument. The machine is composed of a motor, applying a sinusoidal force to the material specimen, a force sensor and a displacement sensor, measuring the amplitudes and the phase angle δ between force and displacement during deformation. The force is adapted until the DMA measures the requested displacement amplitude. Moreover, the specimen can be cooled or heated in a furnace chamber, which accurately controls the temperature (± 0.05 ^0C). In order to investigate the time, frequency and temperature dependent properties of polymers, both static and dynamic measurements can be performed with the DMA. Several clamping devices have been designed to measure different types of deformation situations such as tension, compression, bending and shear. The DMA (type DMA 2980 of TA Instruments, height is about 40 cm) is shown in Figure 3.1.

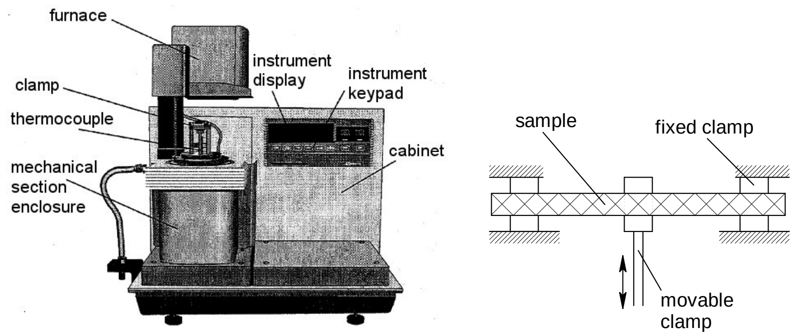

Figure 3.1: *The DMA instrument (left) and a sketch of the dual cantilever clamp (right).*

The operating frequency of the DMA for a dynamic test ranges from 0.01 Hz to 100 Hz. The temperature can be varied between -145 and 600 ^0C. The so-called dual cantilever clamp (Figure 3.1) was used to measure the Young's (storage) modulus E' and the loss factor $\eta = \tan(\delta)$ of the material samples. Due to the relatively high bulk modulus (Poisson's ratio $\nu \approx 0.5$), the shear (storage) modulus G' follows from:

$$G' = \frac{E'}{2(1+\nu)} \approx \frac{E'}{3} \tag{3.1}$$

For the present measurements the specimen was excited with a displacement amplitude of 20 μm. It was shown in a series of preliminary measurements that for this value the material properties were linear in amplitude.

For the materials used in the present study, the operating frequency was varied from 0.1 to 20 Hz in a total of ten steps. In addition, the test was repeated for temperatures between $-15\ ^0C$ and $+25\ ^0C$ with steps of 2 ^0C. The latter was done to extend the frequency range for which the material properties are valid up to at least 10 kHz. This extension is based on the so-called time temperature superposition principle, which is explained in section 3.2.2. Liquid nitrogen was used to cool the material specimens. A typical data set, representing the measured shear modulus of a Vamac 5022 rubber, is shown in Figure 3.2.

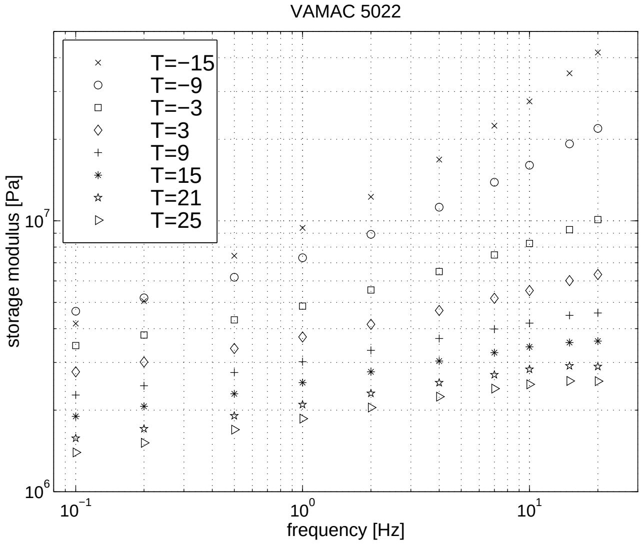

Figure 3.2: *Measured storage modulus for Vamac 5022 as a function of frequency and temperature (in ^0C).*

Evidently, the shear modulus depends strongly on frequency and temperature. In the next subsection all the data is used to create a smooth curve over a wide frequency range.

3.2.2 Time Temperature Superposition principle

The time-temperature superposition (TTS) principle states that the shear modulus of a material at frequency ω and temperature T can be related directly to the modulus at frequency ωa_T and a reference temperature T_0 (Schwarzl and Staverman, 1952):

$$G(\omega, T) = G(\omega a_T, T_0)\frac{T_0\rho(T_0)}{T\rho(T)} \tag{3.2}$$

where ρ is the temperature dependent material density and a_T is the so-called shift factor, which is a function of the temperature. The denomination term of temperature and density is a correction factor.

In other words, a temperature change for materials that obey this relation corresponds to a horizontal shift of the modulus curve on the time or frequency axis. Materials which behave according to this rule are called thermorheologically simple.

The TTS principle, which is also known as the method of reduced variables, is widely used to determine the material properties over a wide frequency range by performing a relatively simple experiment. The software supplied with the DMA 2980 also includes a program to perform a TTS analysis.

Choosing a reference temperature, in this case room temperature, the program automatically shifts the curves horizontally until they coincide and one smooth curve arises representing the storage modulus as a function of frequency (see Figure 3.3). The constructed curve is also known as the master curve. The correction factor for temperature and density is determined via a vertical shift. In the present investigations the procedure was applied only for the temperature. The density of the material was assumed to be constant with temperature.

For the Vamac 5022 material a master curve created in this way is presented in Figure 3.4. It is noted that a reference temperature $T_0 = 19\ ^0C$ was used. This also holds for all further analyses.

As can be seen a smooth overlap of all the curves was achieved. The accompanying shift factors of the analysis for the Vamac 5022 material are plotted as a function of temperature in Figure 3.5.

As a monotonously decreasing curve can be fitted on these shift factors, it confirms that the material obeys the TTS principle. The time-temperature shift for polymers near the glass transition temperature tends to follow the empirical WLF-equation (after William, Landel and Ferry (Ferry, 1980)), reading

$$log(a_T) = -\frac{C_1(T - T_0)}{C_2 + (T - T_0)} \tag{3.3}$$

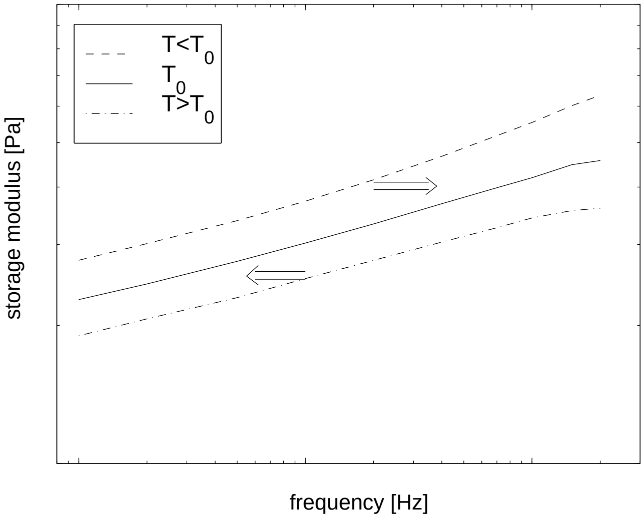

Figure 3.3: *Principle of the shift procedure for the storage modulus.*

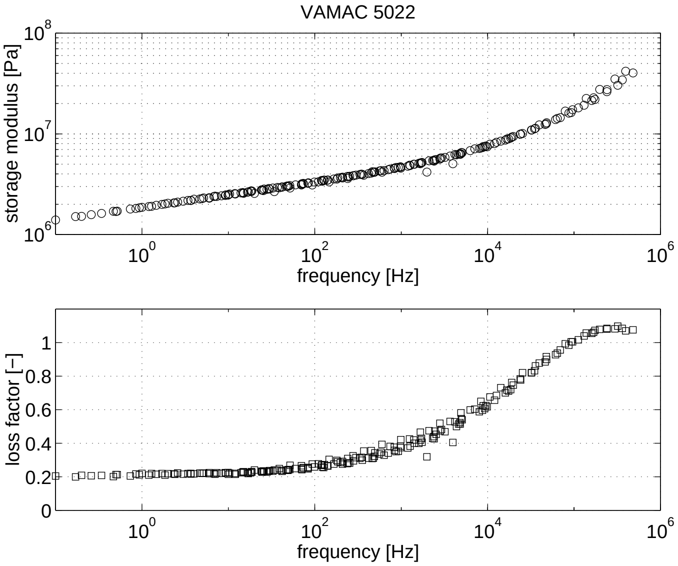

Figure 3.4: *Master curve of the storage modulus and loss factor for Vamac 5022.*

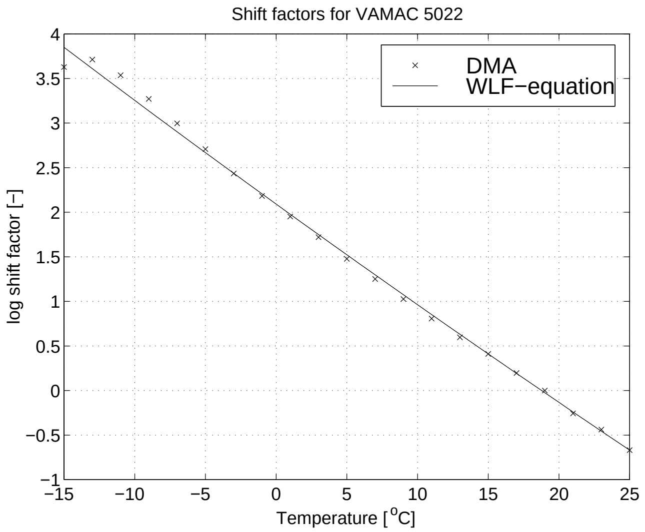

Figure 3.5: *Shift factors of the TTS analysis for Vamac 5022 with corresponding WLF-curve.*

where the coefficients C_1 and C_2 depend on the particular polymer. From an analysis of the material used in this test it appeared that $C_1 = 73.39$ and $C_2 = 689.7$ for the reference temperature $T_0 = 19\ ^0C$. The corresponding WLF curve is also shown in Figure 3.5.

Obviously, when the overlap of measured data is difficult to establish by horizontal shifting only, the material is not thermorheologically simple. It is known that most composite materials, for example, are not thermorheologically simple (Lakes, 1998).

3.2.3 Results and material data fitting

In the present study several types of materials were tested, which basically fall into two categories. First, some acrylic-ethylene-rubbers (AEM) were tested, indicated by the commercial product name Vamac. Vamac is a cross-linked rubber compound with very good damping characteristics. In addition, the material possesses good temperature and oil resistance. The latter makes Vamac particularly useful for demanding applications such as in the automotive industry.

Secondly, some types of two-component polyurethane-rubbers (PMC) were applied. These rubbers were manufactured by mixing two liquid compounds into a pourable polymer at room temperature. This material cures in about 12 hours into a solid, flexible rubber product. The product is well suitable for a good attachment to steel surfaces. The damping performance of PMC materials, however, is less than that of Vamac. Also, the temperature and oil resistivity are less.

In Figure 3.6 the shear modulus and the loss factor of the Vamac 5022 material are shown again as a function of frequency, this time for a frequency range from 10 Hz to 10 kHz. The experimentally determined behaviour can be approximated in a satisfactory way with the help of a Maxwell model with 5 elements, as shown in Figure 3.7.

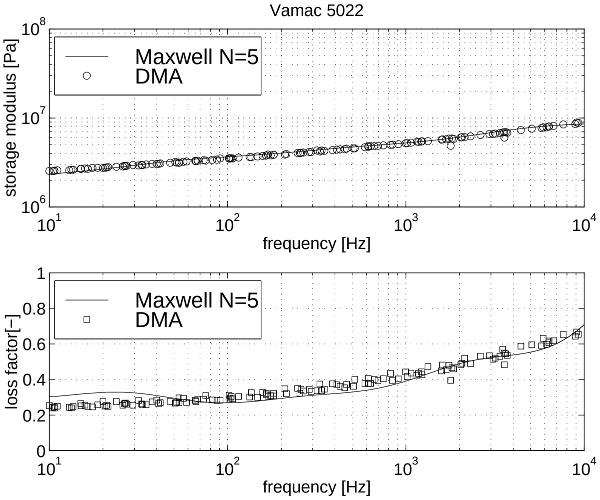

Figure 3.6: *Measured and curve fitted shear modulus and loss factor for Vamac 5022.*

The material data for Vamac 6522 are presented in Figure 3.8. The corresponding model parameters are listed in appendix B. Note that the materials show a large loss factor, specifically in the high frequency range. This is attributed to the fact that the material shifts from a rubbery state to a glassy state via a leathery transition region. This change is accompanied by a strong increase of the shear modulus in the frequency range from 10 Hz to 10 kHz. In the transition region the loss factor reaches

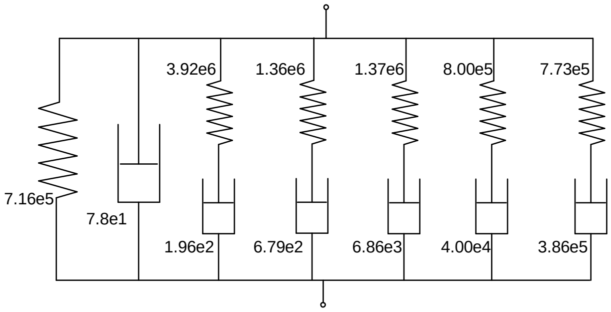

Figure 3.7: *The equivalent Maxwell representation for Vamac 5022.*

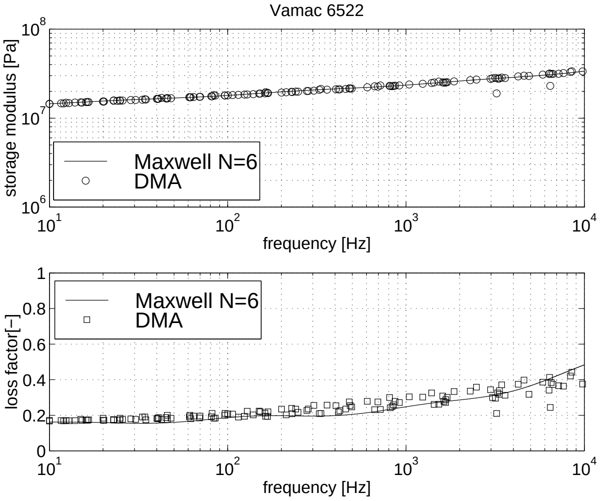

Figure 3.8: *Shear modulus and loss factor for Vamac 6522.*

its maximum value, which can exceed unity as can be observed in Figure 3.4. The stiffness of Vamac 5022 is lower than for Vamac 6522, but the corresponding loss factor is considerably higher. Therefore, this material is of particular interest when vibration damping is required.

The material data are well approximated (curve fitted) with a number of Maxwell elements in accordance with equation 2.32. The curve fitting process was performed numerically using a least square method with the program Matlab. In the approximation, the relaxation times τ_i are set on

fixed values varying from 10^{-6} to 0.5 s, whereas the shear moduli G_i are computed automatically. A minimum number of Maxwell elements is used for the analysis, though sufficient to obtain data fits with an acceptable accuracy over the complete frequency range.
Due to limitations of the software, the program is not capable of determining both the shear moduli and the relaxation times simultaneously. As a result, the data fits still deviate slightly at some frequencies from the measurement results.

One might expect that the DMA procedure itself is also not perfectly consistent. This concerns on the one hand the repeatibility of the DMA test and on the other hand the material properties from different production cycles which may show small differences as well (reproducibility). The results in Figure 3.9 show a fairly good repeatibility for a specific sample, even though the sample was removed and reclamped in the machine.
The results of the test on a DMA sample and on a second specimen from another batch are compared in Figure 3.10. The differences are relatively small and the material fit remains well within the scatter between the two experiments. The material fit only shows some deviations from the measured data for the loss factor at low frequencies, i.e. below 50 Hz.

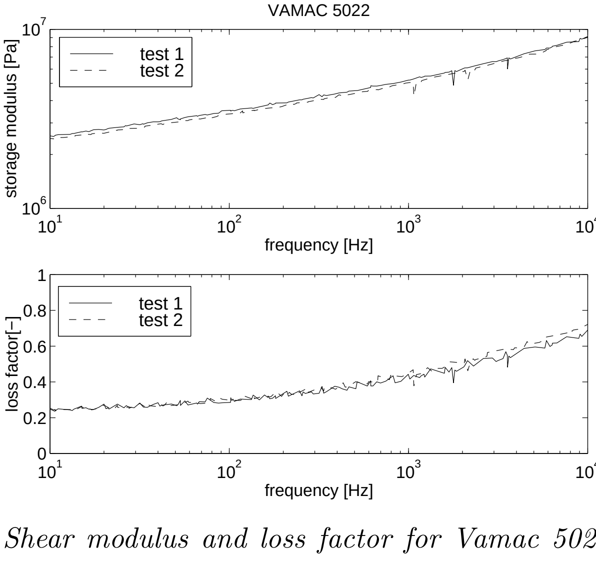

Figure 3.9: *Shear modulus and loss factor for Vamac 5022 regarding repeatibility.*

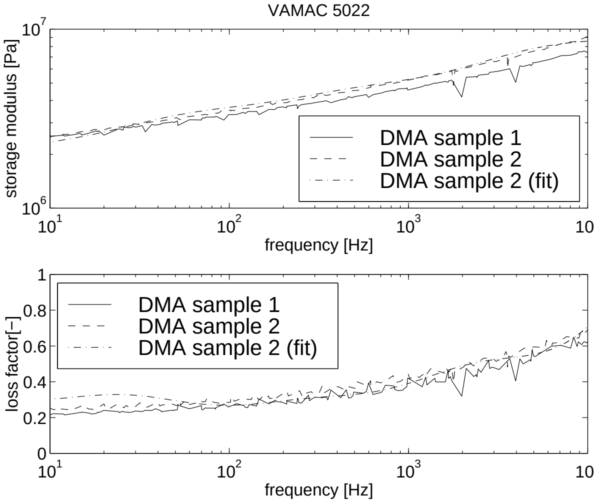

Figure 3.10: *Shear modulus and loss factor for Vamac 5022 regarding reproducibility.*

The shear modulus and the accompanying loss factor of the PMC materials are collected in Figures 3.11 and 3.12 (see appendix B for the model parameters).

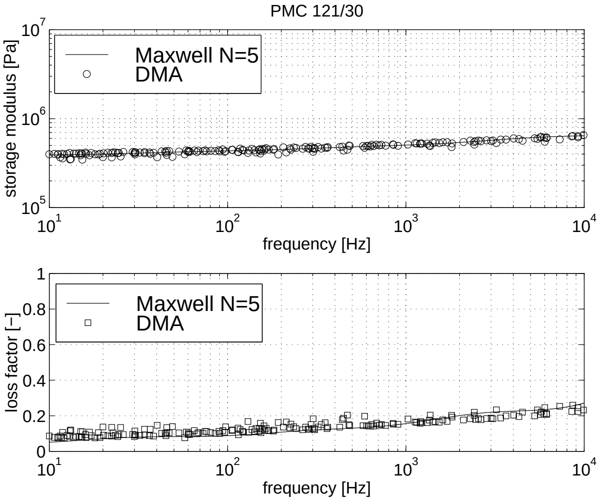

Figure 3.11: *Shear modulus and loss factor for PMC 121/30.*

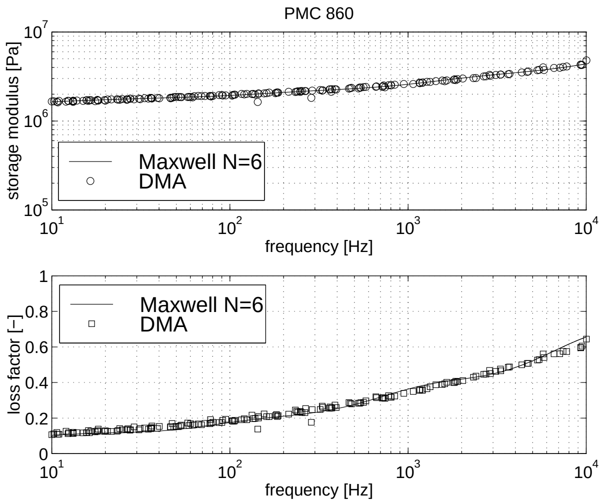

Figure 3.12: *Shear modulus and loss factor for PMC 860.*

These materials are significantly softer than the Vamac materials. As the shear modulus is less frequency dependent, the loss factor of PMC 121/30 is lower than for PMC 860. Due to its relatively low stiffness, PMC 121/30 has a potential for vibration isolation purposes.

Apart from the dynamic shear modulus of the viscoelastic material, also a bulk modulus K must be determined. In the present investigation, this was based on information provided by a material supplier. The bulk modulus K was set to 3500 MPa corresponding with a Possion's ratio of approximately 0.499.

3.3 Experimental validation of a viscoelastic component

The present section deals with the validation of viscoelastic components by means of dynamic (impact) tests on a set of ring samples. These samples contain a viscoelastic layer, and were manufactured in two different ways. It is noted that the experiments were carried out as an intermediate step for validation purposes only. So the aspects of vibration damping and isolation with regard to rolling bearing applications are not yet considered.

3.3.1 Manufacturing methods of ring samples

In order to experimentally validate the viscoelasticity model in combination with the new CMS technique several test samples were analysed with respect to the dynamic behaviour. The samples consist of an inner and an outer steel ring constraining a viscoelastic layer. Different samples are manufactured with either a Vamac or a PMC material layer. Moreover, the thickness, the width and the angle of the layer were varied, as is shown in Figure 3.13 and Table 3.1.

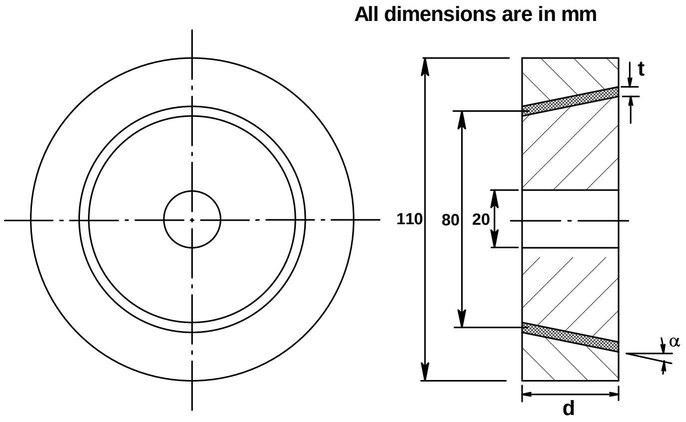

Figure 3.13: *Designs for the ring samples.*

sample	material	thickness t [mm]	width d [mm]	angle α [^{0}]
A	Vamac 5022	1.0	20.0	0
B1	Vamac 5022	2.0	20.0	0
B2	PMC 121/30	2.0	20.0	0
B3	PMC 860	2.0	20.0	0
C	Vamac 5022	3.0	20.0	0
D1	Vamac 5022	2.0	30.0	0
D2	Vamac 6522	2.0	30.0	0
E	Vamac 5022	2.0	30.0	20

Table 3.1: *Parameters of the sample designs.*

The manufacturing of the samples with Vamac was outsourced. Use was made of a transfer moulding process, in which the rubber is pressed inbe-

tween the rings at a high temperature for about 6 minutes. This ensures an effective vulcanization process, which is necessary to create the cross-links inside the rubber.
To create the required stiffness and hardness of the rubber, carbon is added to the compound. Additionally, a large number of other ingredients is used such as release agents, fillers, processing aids, vulcanisers and plasticisers. For a good bonding to the steel surfaces an adhesive is applied. A schematic overview of the transfer moulding process is illustrated in Figure 3.14.

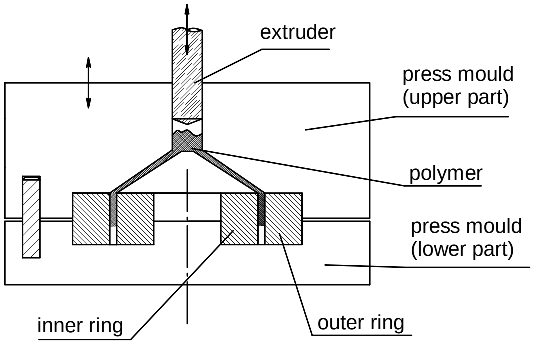

Figure 3.14: *Transfer moulding process for Vamac material.*

The PMC samples are made in a completely different way. In this case use is made of the process as illustrated in Figure 3.15. The liquid polymer mixture is poured into a cavity enabling a flexible, fast and cost effective production of rubber products.

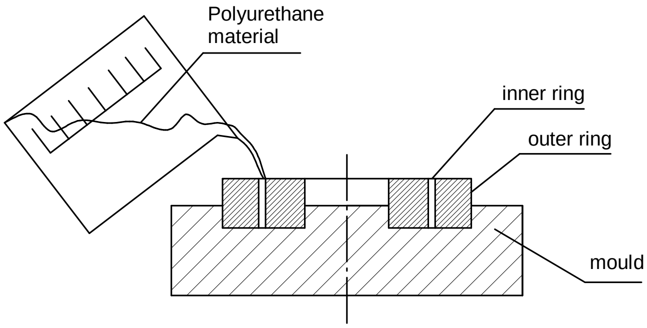

Figure 3.15: *PMC material cold moulding process.*

3.3.2 Experimental results and comparison with numerical results

In order to validate the numerical simulation of the viscoelastic material, Frequency Response Function (FRF) measurements were carried out on the test samples. During the experiments the ring samples were hung in a soft suspension, a condition which is representative for free-free conditions. The LMS Cada-X analyzer is a measurement system that was used for the data acquisition and the signal analysis. The sample is excited by an impact hammer (type PCB) equipped with a force transducer. An accelerometer (type PCB 353B67) was attached to the sample for the response measurement. The response was determined for a point on the outer ring in the axial direction under an impact load on the outer ring at the other side (see Figure 3.16). The time signals were processed with FFT to obtain the auto-power- and cross-power spectra. The cross-power spectrum between the response and force signals was divided by the auto-power spectrum of the force signal to obtain the FRF between the response and the force signals.

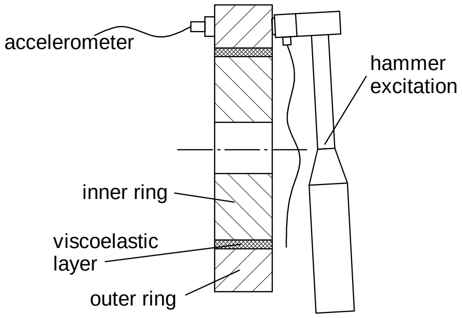

Figure 3.16: *FRF experiments using a hammer impact on a ring sample.*

The model used in the numerical analysis consists of two flexible steel rings and a flexible viscoelastic layer. The interfaces between the components were also considered flexible. In accordance with the theory explained in section 2.4.3, a number of flexible (static) modes was calculated for each interface. In this case it was found to be sufficient to apply 5 waves around the circumference of the interface ($N_r = N_z = N_t = 5$) and a quadratic displacement field over the width ($M_r = M_z = M_t = 2$). In this way, the dynamic behaviour of the sample can be accurately described up to at least 20 kHz. Also a sufficient number of (2nd order) elements was used to accurately describe the deformation of the components. In the case of the viscoelastic layer 4 elements were used across the width, 3 across the thickness and 40 along the circumference.

The FRF of sample B1 as a result of the axial impact is shown in Figure 3.17. Both the displacement amplitude and the phase angle of the FRF are plotted as a function of frequency.

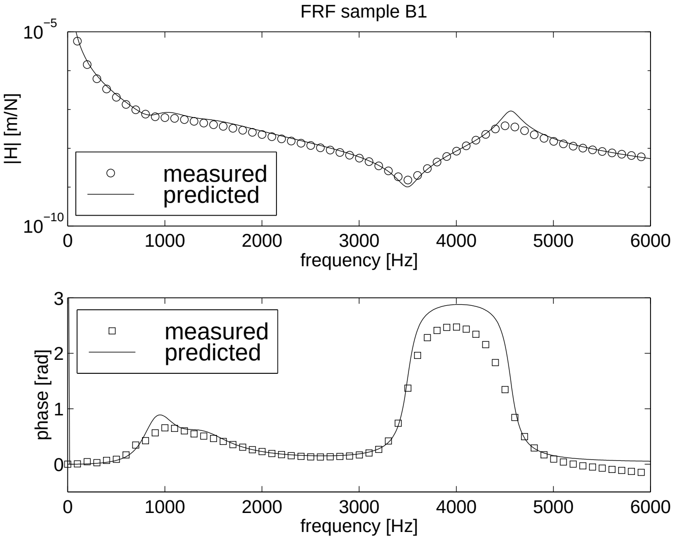

Figure 3.17: *Measured and predicted FRF of sample B1 (Vamac 5022, t=2.0 mm, d=20 mm)*

A good agreement exists between the measured and predicted frequencies of the flexural mode at 4566 Hz (see also Figure 3.18). From Figure 3.17 it also follows that the damping is slightly underestimated. From the computed results it became apparent that around 1000 Hz two resonance frequencies appear which represent the axial and tilting rigid body modes of the outer ring with respect to the inner ring. Clearly, these modes are highly damped.

Similar graphs are shown for the other ring samples, in which the geometry and the material of the viscoelastic layer are varied. In Figure 3.19 the measured and predicted results are presented for samples A, B1 and C having a Vamac 5022 layer with a thickness of 1.0, 2.0 and 3.0 mm, respectively.
It can be observed that besides the increasing resonance frequencies (caused by a higher stiffness), also the damping increases for smaller

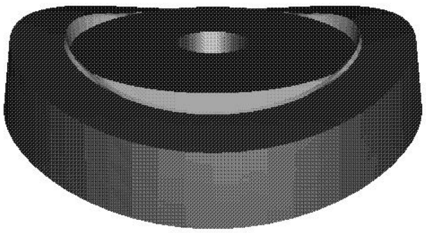

Figure 3.18: *Flexural eigenmode of sample B1 at 4566 Hz.*

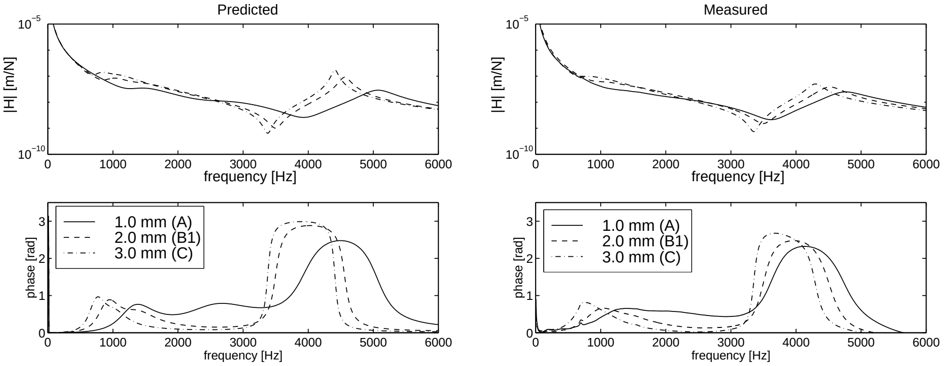

Figure 3.19: *Effect of the layer thickness on the FRF (axial excitation).*

layer thicknesses. The latter can be attributed to the relatively large shear deformation occurring in thin layers. Clearly, these effects are well predicted.

The results discussed so far concern an excitation in the axial direction. A similar analysis was performed in which the radial acceleration as a result of a radial impact force on the outer ring was determined, see Figure 3.20.

In these curves only one resonance frequency above 5 kHz is observed. This frequency corresponds to a flexural mode of the steel outer ring and it is highly damped. In the case of samples A and B1, the resonance modes are hardly observed due to the high stiffness and damping of the configuration. For sample A, the agreement between prediction and measurement is far from excellent. The stiffness of this sample is considerably overestimated, which may be caused by the sample manufacturing process. Due to the small thickness of the viscoelastic layer (1.0 mm), some shrinkage was observed resulting in a poor bonding quality. Obviously, this affects the

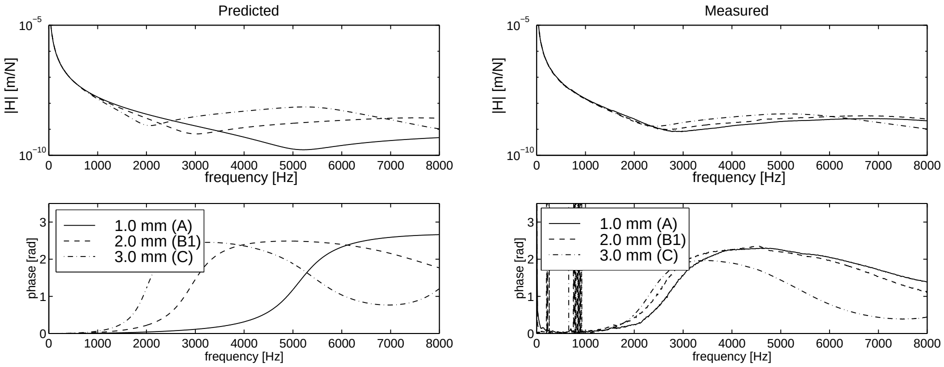

Figure 3.20: *Effect of the layer thickness on the FRF (radial excitation).*

overall stiffness of the sample.
It is noted that very similar radial FRFs were obtained for the remaining samples. Therefore, additional results for radial impacts are not further discussed.

In Figure 3.21 the results on an axial impact force are shown for samples B1 and D1, for which the sample width equals 20 mm and 30 mm, respectively. Both layers consist of Vamac 5022 with a thickness of 2.0 mm.

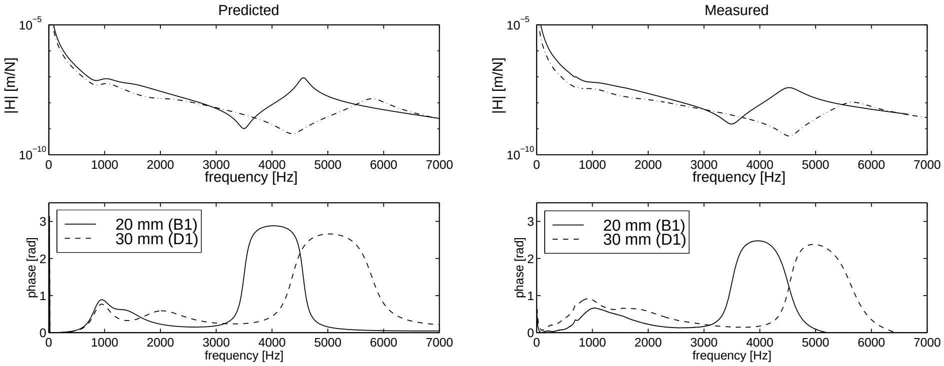

Figure 3.21: *Effect of the layer width on the FRF (axial excitation).*

Due to a larger sample width the flexural stiffness increases so that the resonances shift to higher frequencies. The increased shear deformation causes the damping to increase slightly as well.

The effects of a material change are shown in Figure 3.22, in which sample D is equipped with either a Vamac 5022 (sample D1) or a Vamac 6522 material layer (sample D2).

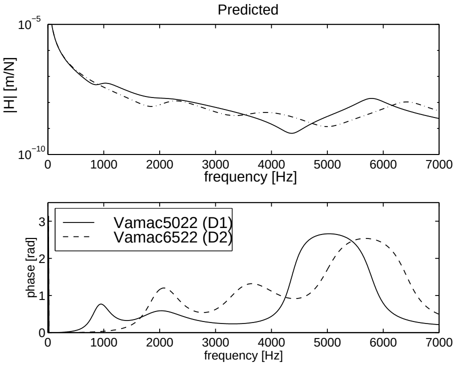

Figure 3.22: *Effect of the layer material on the FRF (axial excitation).*

As could be expected Vamac 6522 behaves more stiffly and is less dissipative than Vamac 5022. The differences, however, are more pronounced in the prediction than in the measurement.

The effect of high damping in the Vamac material and lower damping in the PMC materials is illustrated in Figure 3.23. Note that in this case samples B1, B2 and B3 are considered.

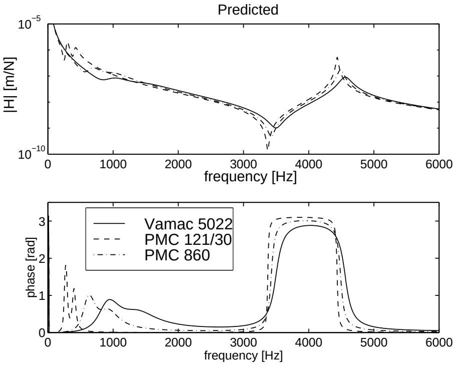

Figure 3.23: *Effect of the PMC layer material on the FRF (axial excitation).*

Clearly, the damping is less for the PMC materials than for Vamac 5022 as follows from the sharp peaks in the curves. Due to the low stiffness the resonance frequencies are lower for sample B with PMC 121/30 in particular.

As a next step we consider the effect of an angle between the viscoelastic layer and the sample axis. The angle of the viscoelastic layer is set to 20^0 for sample E with a (Vamac 5022) layer thickness of 2.0 mm (see Figure 3.13). The FRF is compared with that of sample D1 (also Vamac 5022), as shown in Figure 3.24.

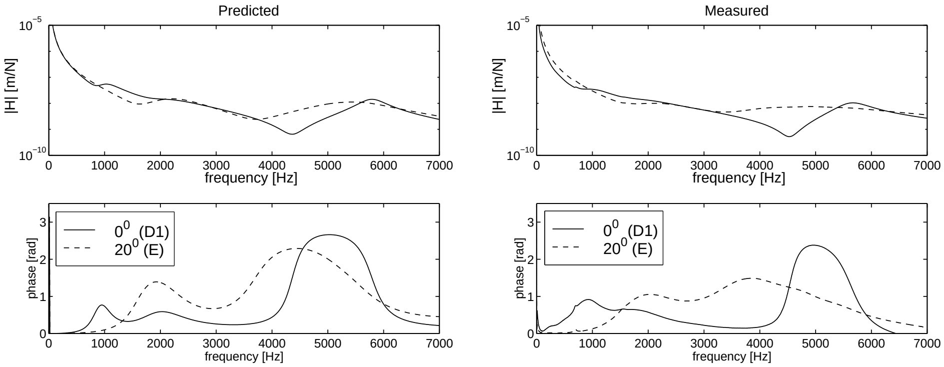
Predicted

Measured

Figure 3.24: *Effect of the layer angle on the FRF (axial excitation).*

This figure reveals that the lower resonance frequencies, i.e. the rigid body modes of the outer ring between 1.0 and 2.0 kHz, increase for a larger layer angle due to an increased axial stiffness. The decrease in resonance frequency of the flexural mode of sample E from 5.6 kHz to about 4.5 kHz has to be attributed to the decrease in stiffness of the steel outer ring, as for a tapered ring the thickness decreases significantly over the axial direction (see Figure 3.13). Note that for sample E the damping of the flexural resonance is significantly higher than for sample D1. The good agreement between the predictions and measurements shows that the flexible interface model is also applicable to conical ring shapes.

3.4 Conclusions

Experiments were performed on several viscoelastic materials. Measurements on the Dynamic Mechanical Analyzer (DMA) in combination with the Time Temperature Superposition principle have shown to be an effective way of determining the frequency dependent stiffness and damping of a material over a wide frequency range. Subsequently, the measured data can accurately be approximated in the frequency domain from 10 Hz to 10 kHz with 5 or 6 Maxwell elements.

The numerical model for viscoelastic components is validated with dynamic experiments on various ring samples. A number of samples were made with the cold moulding process. It was found that this is a flexible and cost effective manufacturing method for viscoelastic products.

In general, a good agreement is obtained between the numerically and experimentally determined dynamic behaviour of several ring samples. Both the influence of the viscoelastic material type and the effects of a geometry variation are reasonably well predicted. This justifies the conclusion that the modelling of viscoelastic components is sufficiently accurate for usage in the design of an effective viscoelastic bearing support.
The results also showed that the damping capability of the viscoelastic layer is high, in particular for Vamac material.

Chapter 4

Structural analysis of a rotor dynamics test rig

4.1 Introduction

In order to demonstrate the capability of a viscoelastic support to reduce the vibration level of a structure, a rotor dynamics application was analysed both numerically and experimentally (see also Tillema and Wensing (2002a)). For this purpose a specially designed test rig, named VICTORIA, was used. For the present design studies a structural model of this test rig was made. First, FEM models were built and validated at a component level (section 4.3). Next, a structural model of the assembly was constructed based on the procedure described in Chapter 2.

The dynamic behaviour of the test rig model was validated with experiments on the non-rotating system (section 4.4). This included configurations of the test rig with several viscoelastic material supports.
Finally, in section 4.5, the dynamic behaviour of the test rig is analysed under operating conditions.

4.2 The VICTORIA test rig

In these investigations a specially designed test rig, VICTORIA, is used. VICTORIA stands for VIbration Control Test rig Of Rolling bearings In Applications (Figures 4.1 and 4.2). It was developed by SKF ERC for testing the vibration behaviour of low-noise rolling bearings. VICTORIA is a flexible and well-controllable apparatus enabling the study of the operation of the bearing under a wide range of conditions, representative for actual applications.

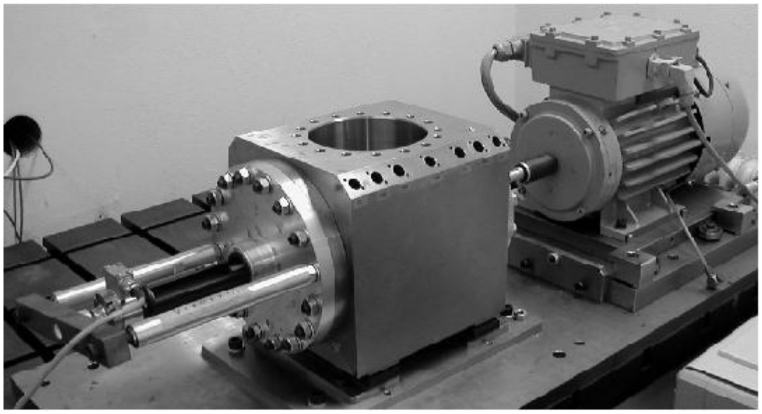

Figure 4.1: *The VICTORIA test rig.*

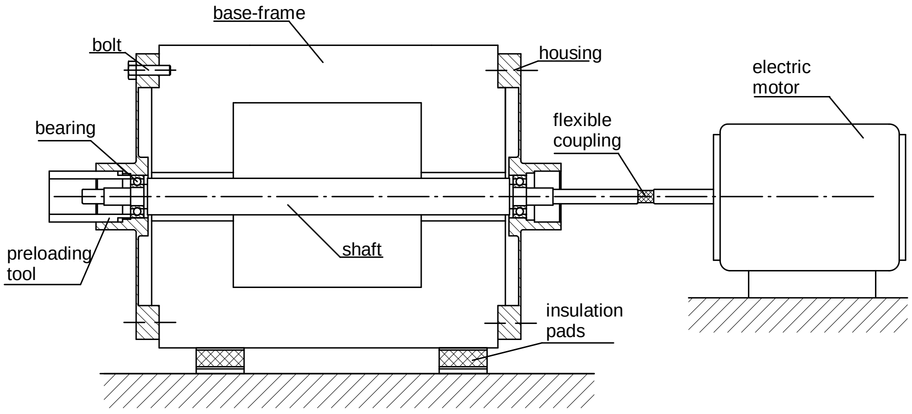

Figure 4.2: *Schematic overview of the VICTORIA test rig.*

Basically, the test rig consists of the following components (Figure 4.2):

- A very stiff and heavy base-frame supported by a soft mounting.
- Exchangeable housings bolted to the base-frame.
- A long, flexible shaft supported in the housings by two rolling element bearings (DGBB 6202).

- A tool used for axial preloading of the bearings.
- An electric motor to drive the test rig. A highly flexible coupling between the motor and the test rig ensures that motor vibrations are not transferred to the test rig shaft.
- Rubber insulation pads ensuring that vibrations of the environment are fully isolated.

Although the test rig is designed to analyse bearing related parameters under operating conditions, it is also well-suited to study vibration transmission characteristics under non-rotating conditions. Using the base-frame and the shaft as they are, it means that only the flexible housings had to be redesigned to investigate the dynamic behaviour of the test rig with viscoelastic supports.

4.2.1 Practical implementation of the viscoelastic bearing support

In Figure 4.3 it is shown how a configuration of the flexible housing with a viscoelastic bearing support is obtained. The sandwich rings consist of a steel inner and outer ring constrained by a viscoelastic core. The sandwich rings with a PMC material core were manufactured with the cold moulding process. The rings with a Vamac core were made with a (cost saving) cut and glue method.

To enable an easy assembly of the sandwich rings it is necessary to provide the rings with loose fittings for the outer bore. This, however, creates an additional interface which might cause problems when the structure starts to vibrate. There is a strong possibility that the rings will vibrate at the interface level rather than in the sandwich core itself. To avoid this problem the rings need to be locked to the adjacent components, e.g. by a bolt connection. A solution is shown in Figure 4.4, in which the inner and outer ring are fixed in the axial direction.

4.2.2 Experimental setup

One of the main purposes of the tests was to demonstrate that vibrations of the shaft can be isolated from the housing with the viscoelastic layer.

In non-rotating conditions this was achieved by determining the FRF between the shaft excitation and the flexible housing, as is illustrated in Figure

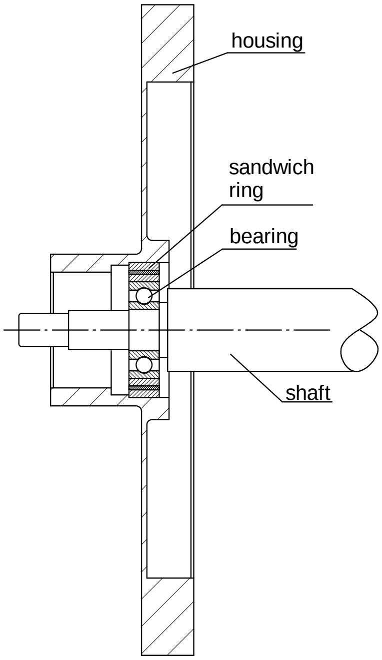

Figure 4.3: *Redesigned housing with a viscoelastic bearing support.*

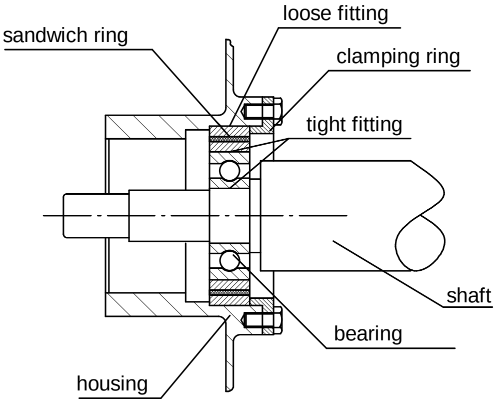

Figure 4.4: *Assembly arrangement for the sandwich ring.*

4.5. This setup was also used for the modal analysis. The signal analysis was performed again using the LMS Cada-X analyzer (see section 3.3.2).

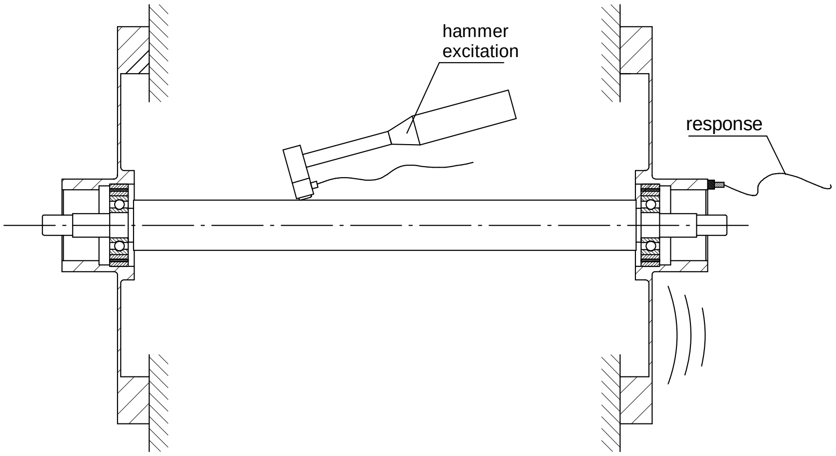

Figure 4.5: *Test setup of the test rig for dynamic transfer analysis and experimental modal analysis.*

Under operating conditions, the bearings and the shaft imbalance are the main vibration sources of the test rig (see Figure 4.6). The shaft vibrations are transmitted from the shaft through the bearings and the sandwich rings to the housing. The bearing vibrations are transmitted to the housing via the sandwich rings.

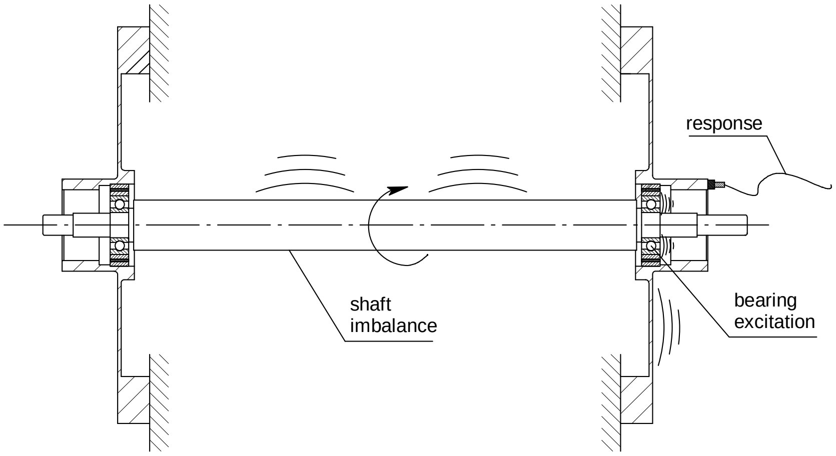

Figure 4.6: *Test setup of the test rig under operating conditions.*

The shaft was driven by a frequency controlled electric motor. The rotational speed was varied from 0 to 6000 rpm. During these running tests the response signal of the housing was measured with a single accelerometer (type PCB) and processed with a National Instruments data acquisition card (type AT-A2150). Finally, the time signals were recorded in the software program LabView.

4.3 Structural model of the test rig

The VICTORIA test rig contains 4 flexible elastic components: the shaft, two housings and the base-frame. In addition, the assembly contains two rolling element bearings and two sandwich rings. Each flexible component of the assembly was modelled with FEM and the results were validated with the measured results. The bearings were modelled as a special element in the software and included in the assembly model. The sandwich rings were modelled in the same way as the sample rings, as described in Chapter 3.

4.3.1 Elastic components

The *steel shaft* was modelled with 164 beam elements along the total length. Up to 9 kHz the calculated eigenfrequencies showed an excellent agreement with the measured ones, as shown in Table 4.1.

nr.	mode	experiment [Hz]	FEM [Hz]	difference [%]
1	1st bending	568	574	1.1
2	2nd bending	1305	1286	-1.5
3	3rd bending	2738	2694	-1.6
4	4th bending	3563	3554	-0.3
5	5th bending	4701	4683	-0.4
6	6th bending	6908	6620	-4.2
7	axial	7178	7375	2.7
8	7th bending	8634	8268	-4.2

Table 4.1: *Eigenfrequencies of the shaft.*

The average deviation between FEM model and experiment is 2 %.

The *aluminium housing* was modelled in the FEM package ANSYS. At the bolt positions (Figure 4.2) the housing is assumed fixed to the ground. The eigenfrequencies of the system were determined up to 6 kHz both numerically and experimentally (see Table 4.2). The average deviation from the experimental results is less than 6 %, which is acceptable for further analysis.

nr.	mode	experiment [Hz]	FEM [Hz]	difference [%]
1	axial tube (1)	369	327	-11.4
2	tilt tube (1)	621	561	-18.4
3	flexural (1)	2858	2905	1.6
4	axial tube (2)	2913	2818	-3.3
5	tilt tube (2)	3015	2929	-2.9
6	flexural (2)	3443	3367	-2.2
7	flexural (3)	4064	4067	0.1
8	flexural (4)	4818	5055	4.9

Table 4.2: *Eigenfrequencies of the housing.*

The *base-frame* of the test rig was very stiff. Its first eigenfrequency is at about 2.5 kHz. In order to accurately predict the dynamic behaviour of the total application up to about 5 kHz it was decided to model the base frame in ANSYS as well. The results, showing a good agreement with the measured results, are given in Table 4.3.

nr.	mode	experiment [Hz]	FEM [Hz]	difference [%]
1	oval top (1)	2452	2700	10.1
2	oval top (2)	3152	3222	2.2
3	oval front	4278	4513	5.5
4	oval side	4487	5171	15.2
5	torsion (1)	4765	4900	2.8
6	breath	5031	5244	2.2

Table 4.3: *Eigenfrequencies of the base-frame.*

Before assembly, each FEM component was reduced with the Component Mode Synthesis technique. For this purpose, interfaces were defined on the surfaces shared between adjacent components, such as for the housing bore, the shaft-bearing fittings and the interfaces between the housings and the base-frame. For each of these surfaces a rigid interface was assumed.

4.3.2 Viscoelastic sandwich rings

The sandwich rings consist of an inner and outer ring of steel with a viscoelastic layer in between. The inner bore of the inner ring is 35 mm, whereas the outer bore of the outer ring measures 49 mm. The ring width is 11 mm (Figure 4.7). The thickness of the viscoelastic core was varied between 1.5 and 3.0 mm. In addition, different viscoelastic materials, i.e. Vamac 5022 and PMC 121/50, were applied. A Maxwell representation was used to describe the frequency dependent material properties (see Appendix B).

The steel rings and the viscoelastic core were separately modelled with FEM and reduced with the CMS technique. The interfaces of each component were assumed to be rigid (ref. section 2.4.1).
Due to their relatively small size, it appeared not possible to perform an experimental modal analysis on the sandwich rings. The structural model and a photograph of a deep groove ball bearing mounted in a sandwich ring are shown in Figure 4.7.

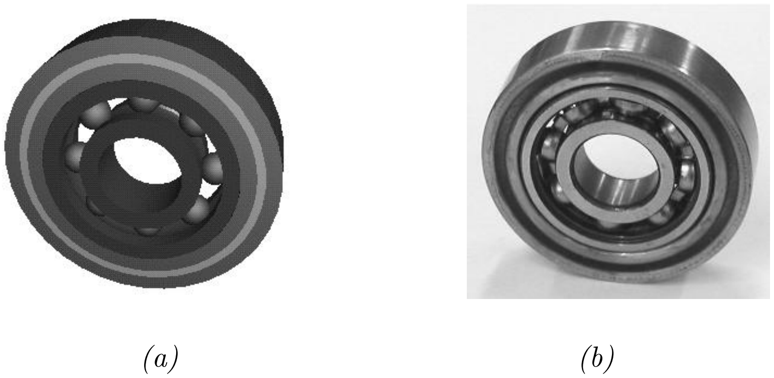

(a) (b)

Figure 4.7: *(a) Numerical model and (b) photograph of a deep groove ball bearing (type DGBB 6202) mounted in a sandwich ring with a viscoelastic core.*

4.3.3 Assembly

The remaining components to be modelled were the rolling bearings. The VICTORIA test rig contains two deep groove ball bearings (type 6202, see Appendix C for details) which were modelled as special elements in the structural modelling tool. In this case, a rigid ring ball bearing model was added to the test rig assembly. The stiffness of the bearing depends on the geometry and the bearing preload, which for this application was set to 60 N. The preload was applied on the outer ring of the left bearing (see Figure 4.2), which is free to move in the axial direction. The effect of lubrication damping was accounted for by a constant contact damping coefficient of 100 Ns/m^2. Experience at SKF has shown that this value is characteristic for a combined inner and outer contact in a deep groove ball bearing.

As a next step, the components were assembled into the complete test rig model as presented Figure 4.8. A close-up view of the viscoelastic bearing support is shown in Figure 4.9.

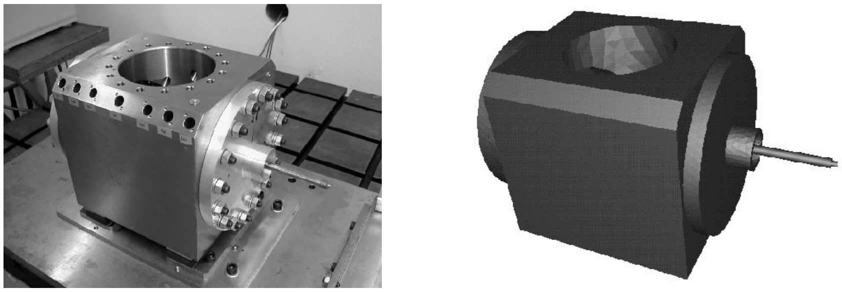

(a) Photograph *(b) Structural model*

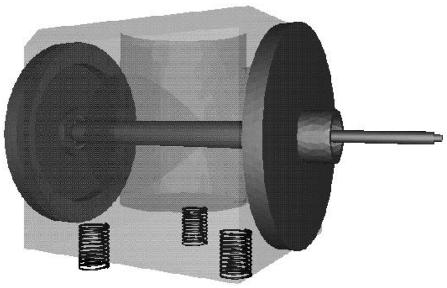

(c) Transparent view

Figure 4.8: *The VICTORIA test rig.*

It is noted that the base-frame is suspended from soft springs.

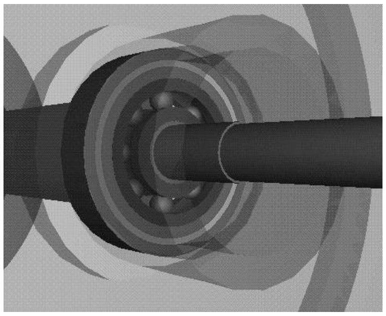

Figure 4.9: *The model of the the rolling bearing and its support in the test rig.*

4.4 Experimental validation of the test rig model

In order to validate the numerical model with experiments, both a modal analysis and an FRF analysis were carried out on the non-rotating system. The procedure was repeated for different viscoelastic bearing supports.

4.4.1 Modal analysis of the non-rotating test rig

The experiments on the non-rotating test rig were carried out with the LMS Cada-X analyzer. The setup, as sketched in Figure 4.5, was used to determine the modal properties of the application. It is noted that the selected position of the sensors and the location of the hammer impact depend on which eigenmode is to be determined. The most important eigenmodes up to 5 kHz and accompanying modal damping values were determined. In general, the eigenmodes of the system are dominated by the displacements of either the shaft, the housing or the base-frame.

First, the test rig was considered without a viscoelastic bearing support. For this purpose the sandwich ring was replaced by a steel dummy ring. In Figure 4.10 the measured and predicted eigenfrequencies and corresponding eigenmodes of the test rig that are dominated by the motions of the base-frame are shown.
Obviously, the base-frame eigenfrequencies are in the high frequency range and are well predicted by the structural model. It should be noted that the base-frame resonance modes will hardly be excited by the vibration sources under normal running conditions. The resonance modes of the test rig which

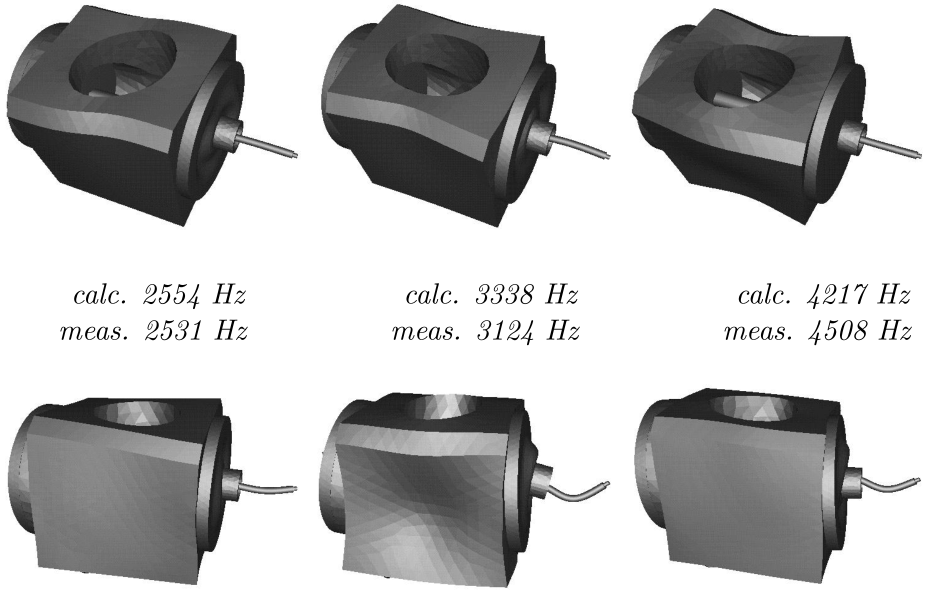

calc. 2554 Hz
meas. 2531 Hz

calc. 3338 Hz
meas. 3124 Hz

calc. 4217 Hz
meas. 4508 Hz

calc. 4593 Hz
meas. 4781 Hz

calc. 4719 Hz
meas. 4806 Hz

calc. 5025 Hz
meas. 5000 Hz

Figure 4.10: *Base-frame dominated eigenmodes of the VICTORIA test rig.*

will be excited under operating conditions are dominated by displacements of either the housing or the shaft.

The most important housing dominated eigenfrequencies and eigenmodes are presented in Figures 4.11 and 4.12.

A good agreement between measurement and prediction was obtained for most of the eigenfrequencies. An exception is the first eigenfrequency, which is highly underestimated: measured at 180 Hz and predicted at 85 Hz. This has to be attributed to the assumed loose interface between the (left) bearing outer ring and the housing. In practice, however, the interface will never be perfectly loose or, in other words, the bearing is not fully free to move in the axial direction. As a result, the measured eigenfrequency is higher than predicted.

Finally, the eigenfrequencies and eigenmodes of the test rig dominated by displacements of the shaft are shown in Figures 4.13 and 4.14.

Both figures reveal a good agreement between the measured and predicted eigenfrequencies. So it can be concluded at this stage that the numerical

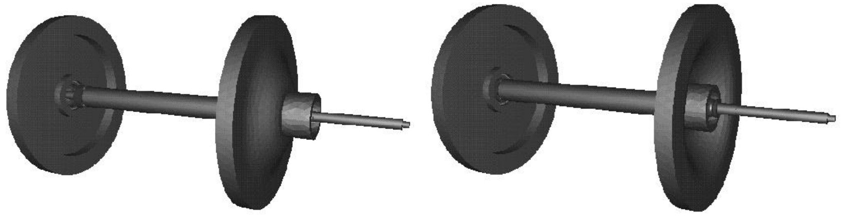

calc. 85 Hz
meas. 180 Hz

calc. 769 Hz
meas. 746 Hz

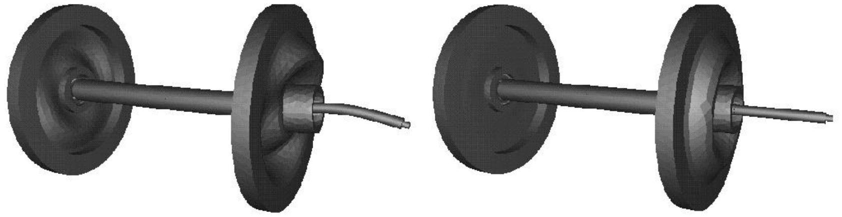

calc. 2788 Hz
meas. 2796 Hz

calc. 2920 Hz
meas. 2962 Hz

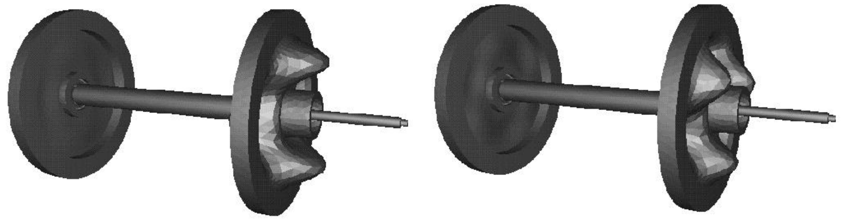

calc. 3007 Hz
meas. 3013 Hz

calc. 3466 Hz
meas. 3431 Hz

Figure 4.11: *Housing dominated eigenmodes of the VICTORIA test rig with dummy rings.*

simulation of the dynamic behaviour of the test rig assembly provides a prediction which is sufficiently accurate to make the next step, namely the extension to the application with viscoelastic bearing supports.

By replacing the full steel ring with a sandwich ring with a viscoelastic core, the modal properties will change in particular for the shaft dominated

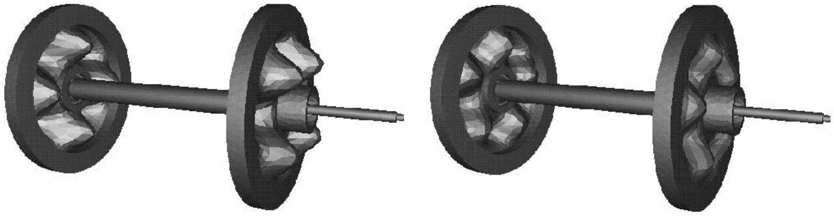

calc. 4234 Hz
meas. 4083 Hz

calc. 5336 Hz
meas. 4929 Hz

Figure 4.12: *Housing dominated eigenmodes (cont.) of the VICTORIA test rig with dummy rings.*

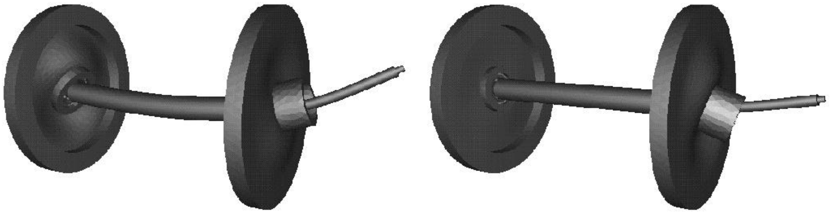

1: calc. 491 Hz
meas. 506 Hz

2: calc. 525 Hz
meas. 515 Hz

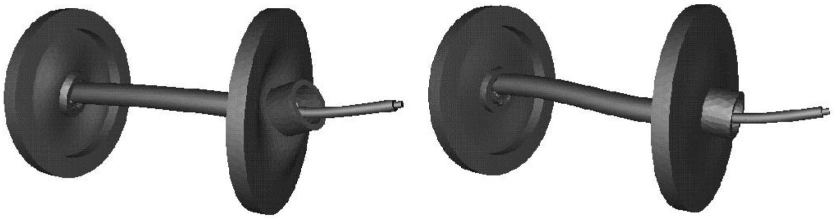

3: calc. 644 Hz
meas. 636 Hz

4: calc. 1674 Hz
meas. 1761 Hz

Figure 4.13: *Shaft dominated eigenmodes of the VICTORIA test rig.*

vibration modes, see Figure 4.15. Clearly, the base-frame dominated eigenfrequencies are not affected by the viscoelastic support. Also the housing dominated eigenfrequencies are hardly influenced by the sandwich

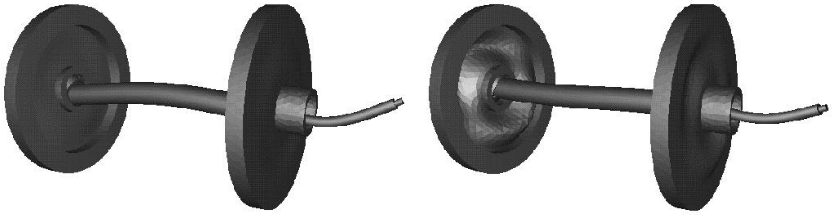

5: calc. 2393 Hz
meas. 2568 Hz

6: calc. 2883 Hz
meas. 2990 Hz

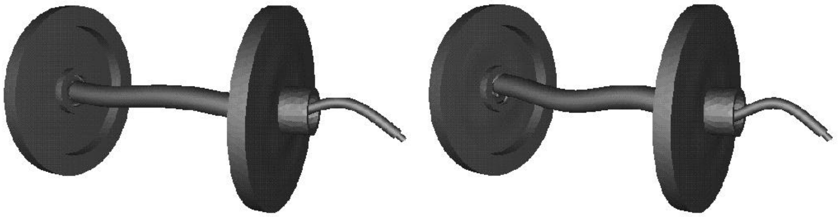

7: calc. 3679 Hz
meas. 3751 Hz

8: calc. 4883 Hz
meas. 4963 Hz

Figure 4.14: *Shaft dominated eigenmodes (cont.) of the VICTORIA test rig.*

rings and are therefore not considered further.

Clearly, the eigenfrequencies decrease in the case of a viscoelastic support. It can be observed that modes number 4 and 5 in particular are affected by the viscoelastic layers. Due to the relatively low radial stiffness of the viscoelastic layers the mentioned modes change character, namely from flexible shaft modes (as presented in Figure 4.14) to rigid body modes of the shaft in the support. Overall, the measured trends are well predicted by the model.

4.4.2 FRF analysis of the non-rotating test rig

In addition to the modal properties, the frequency response function (FRF) of the acceleration of the non-rotating test rig on a radially applied force on the shaft was determined. The FRF was directly found with the LMS Cada-X analyzer during the experimental modal analysis. Numerically, the FRFs were determined by performing a harmonic response analysis in the

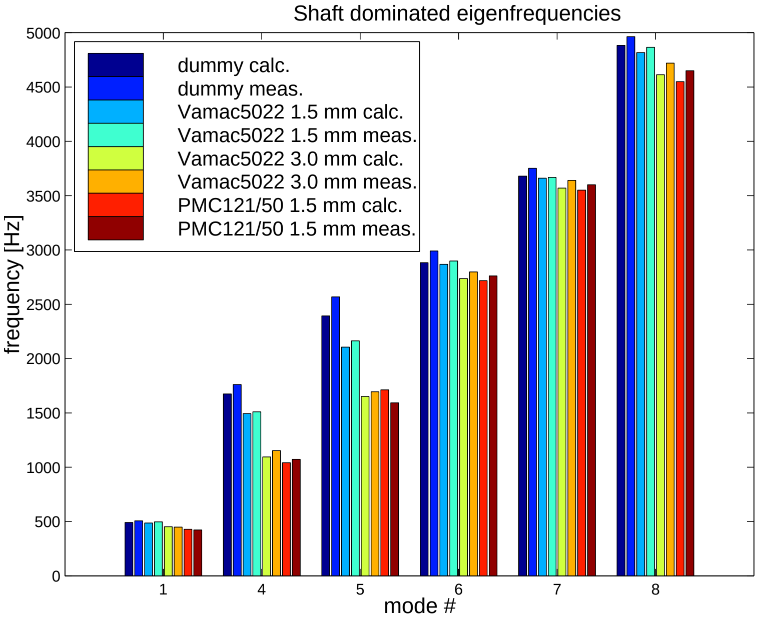

Figure 4.15: *Eigenfrequencies for six shaft dominated modes of the test rig with various supports.*

way explained in section 2.5. To account for damping in the system, the elastic components were given a structural damping value of 0.5 %.

In Figures 4.16 and 4.17 the predicted and measured FRFs of the middle point of the shaft on a radial shaft impact are shown for the test rig with dummy rings and with viscoelastic bearing supports.

A satisfactory agreement was obtained between the predictions and measurements. As mentioned in the previous section, the frequencies agree quite well, but the measured FRFs show somewhat more damping. This is probably caused by damping created in the interfaces between the bearings, the sandwich rings and the housings. Clearly, this type of damping is not fully captured in the model by a single structural damping coefficient.

The vibration transfer behaviour from the shaft to the housing was analysed by determining the FRF of a point on the housing on a radial excitation of the shaft. A specific location on the end tube of the (right-hand) housing was considered in these analyses (see Figure 4.5). In Figures 4.18 and 4.19

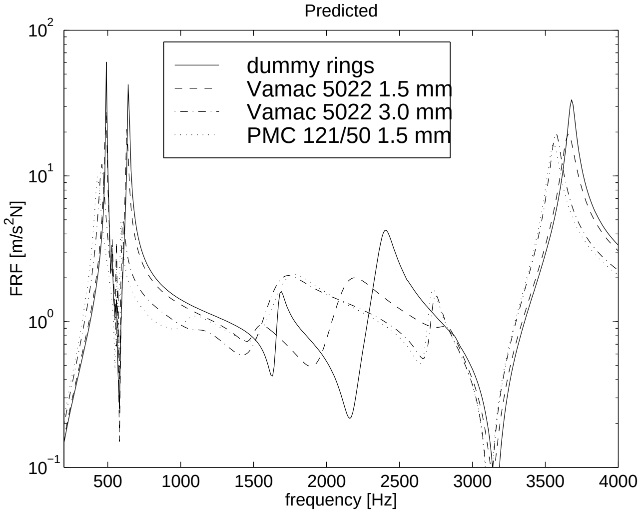

Figure 4.16: *Predicted FRF for the middle point of the test rig shaft.*

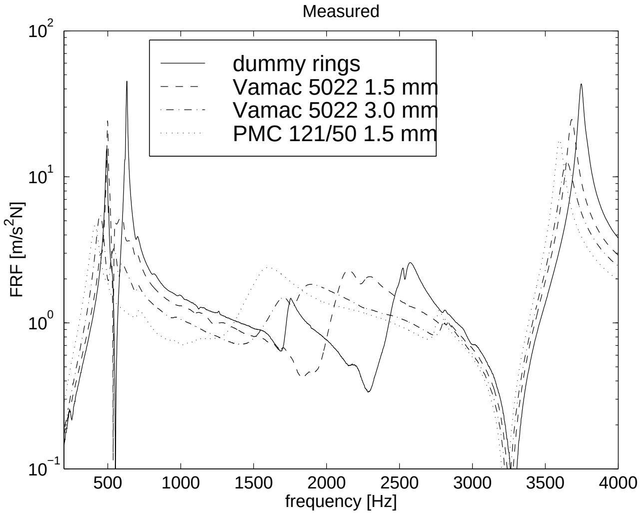

Figure 4.17: *Measured FRF for the middle point of the test rig shaft.*

the FRFs of the housing are shown for the test rig with different bearing supports.

Although the agreement between prediction and measurement is far from

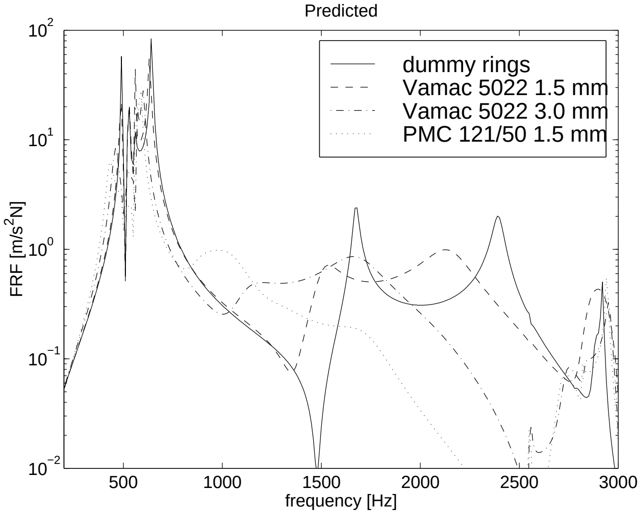

Figure 4.18: *Predicted FRF for a point on the housing of the test rig.*

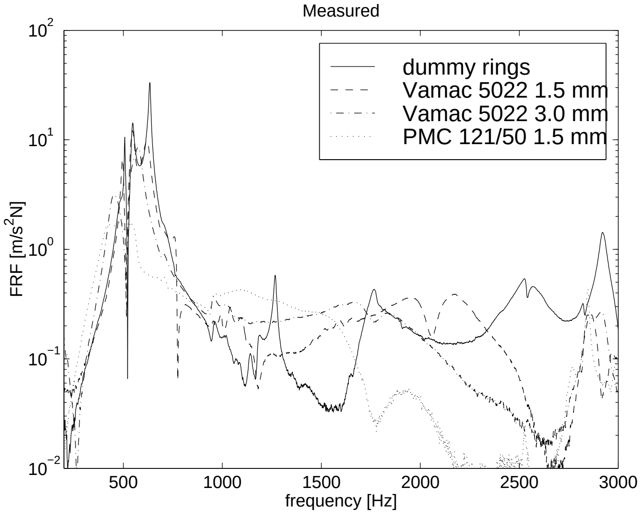

Figure 4.19: *Measured FRF for a point on the housing of the test rig.*

excellent, the effects on vibration damping and isolation of the viscoelastic supports are predicted in a satisfactory way. By the presence of a viscoelastic bearing support, vibrations of the shaft are effectively isolated from the housing. This effect is most pronounced for the system with PMC 121/50 layers due to their low stiffness. Vibration damping appears to be most effective with Vamac 5022 supports.

Overall, it can be concluded that the comparison between the measured results and those of the numerical model justifies the conclusion that the numerical model is suited to be used in design studies.

4.5 Results for the rotating test rig

As a final proof of the vibration reducing capabilities of a viscoelastic bearing support, experiments were performed on the VICTORIA test rig under operating conditions. First, a running mode analysis was performed with a constant rotational speed. Next, the rotational speed was varied in order to obtain a so-called Campbell diagram.

4.5.1 Spectrum analysis of the rotating test rig

The experimental setup as shown in Figure 4.6 was also used for these experiments. The structure was excited by the imbalance of the shaft and the bearing related excitation forces. The test rig was driven by the external electric motor with a rotational speed of 5000 rpm (83.33 Hz). In Figure 4.20 the measured frequency spectrum of the axial acceleration of the housing (location on the small end tube, see Figure 4.5) is presented for the test rig with dummy rings.

It can be observed that mainly two resonance frequencies are excited around 500 and 750 Hz. These resonance frequencies correspond with the first bending mode of the shaft and an axial mode of the housing (see Figures 4.13 and 4.11).

The vibration spectra can be interpreted in a more convenient way when they are presented in a convoluted format. For this purpose, the spectral data were added together over frequency bands of 84 Hz, which is equal to the rotational speed of the shaft. As a result, each convoluted summation contains the contribution of one order of the rotational frequency. In Figure 4.21 the convoluted spectra of the velocity level of the housing are presented for the test rig with and without viscoelastic bearing supports. The velocity level L_v is given in decibels (dB), and is defined as:

$$L_v = 10 \log \left(\frac{|v|^2}{v_{ref}^2} \right) \tag{4.1}$$

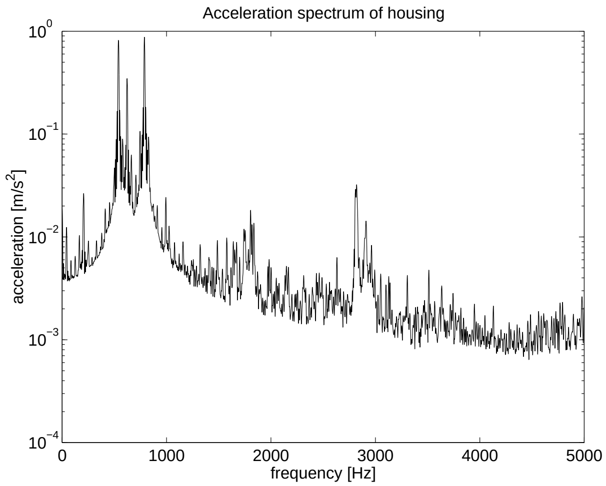

Figure 4.20: *Frequency spectrum of the acceleration of the housing for the test rig with dummy rings.*

where $|v|$ is the velocity spectrum magnitude and v_{ref} the reference velocity level. In these analyses, v_{ref} is chosen such that the velocity level is in the same order of magnitude as the radiated sound power level of a vibrating surface with the dimensions of the shield:

$$v_{ref}^2 = \frac{W_{ref}}{\rho_0 c_0 S} \tag{4.2}$$

where W_{ref} is the reference value of the sound power which is equal to 10^{-12} W. The air density is denoted by ρ_0, the speed of sound by c_0 and the surface area by S. For $\rho_0 = 1.2\ kg/m^3$, $c_0 = 340\ m/s$ and $S = 255\ cm^2$ a reference velocity v_{ref} of $3.1 \cdot 10^{-7}\ m/s$ is found. A summation is made over the complete frequency range to obtain the rms velocity level, which is indicated in the legend.
From Figure 4.21 a clear vibration isolation effect can be observed for the case of a viscoelastic bearing support. The effect is largest for the PMC 121/50 material and least for the Vamac 5022 1.5 mm layer, which is also expected and in line with the stiffness of these configurations. It is noted that the resonance peak around 750 Hz has disappeared, meaning that the axial vibrations of the shaft are effectively isolated.

The running mode analysis was also performed numerically. For this purpose, a transient dynamic simulation was performed with a time step

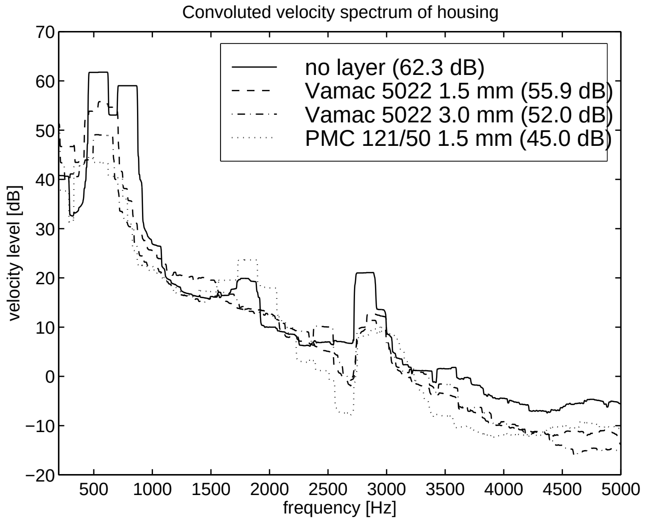

Figure 4.21: *Measured convoluted velocity spectrum of the housing.*

$\Delta t = 10^{-5}s$ for a total of 100,000 steps. The first 50 % of the response signal was left out in order to let transient effects die out. As a result, the frequency resolution equals 4 Hz.

The time signals were analysed with a Fast Fourier Transform in combination with a Hanning window to avoid signal leakage in the frequency domain. In the simulation, the shaft was given a 25 μm eccentricity at a rotational speed of 5000 rpm (83.33 Hz). The resulting convoluted velocity spectra of the test rig housing are shown in Figure 4.22.

Similar trends can be observed as in the measured convoluted spectra. In both cases, the resonance peaks around 500 and 3000 Hz dominate the spectrum. The predicted velocity levels, however, are significantly lower than the measured levels in the frequency range from 700 to 2750 Hz and for frequencies above 3 kHz. One should be aware that due to mounting and remounting of the test rig, the excitation behaviour may change. Moreover, the actual excitation forces depend on the viscoelastic bearing support. In the numerical analyses these forces were assumed to be constant. Apart from the shaft imbalance, vibrations also occur inside the rolling bearings, which are not considered in the numerical analyses.

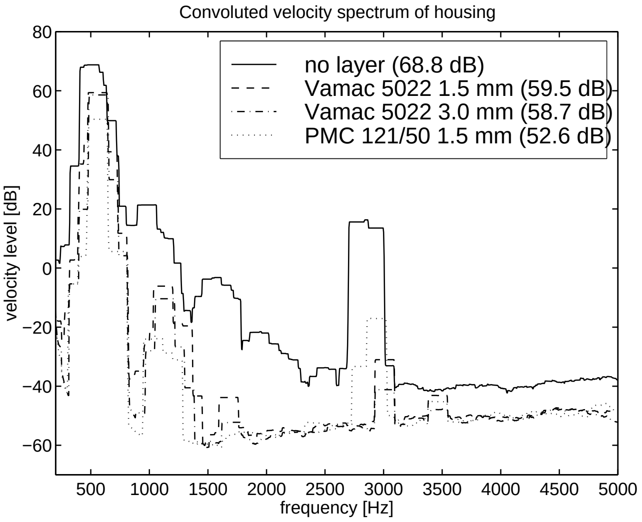

Figure 4.22: *Predicted convoluted velocity spectra of the housing.*

4.5.2 Campbell diagram analysis of the rotating test rig

In the following experiments, the frequency spectra of the acceleration of the housing were measured for increasing rotational speeds. The measured spectra were collected in a matrix and presented in the form of a contour plot, a so-called Campbell diagram. In such a diagram the resonance frequencies show up as vertical bands, whereas excitation frequencies are characterised by straight (order) lines proportional to the rotational speed. In Figures 4.23 4.24 the Campbell diagrams of the test rig both with dummy rings and with viscoelastic supports are shown. The rotational speed is varied from 2000 to 6000 rpm (33.33 to 100 Hz).

It can be observed that several resonance frequencies appear. It is predominantly the bending modes around 500 Hz that are excited. In the case of the test rig with dummy rings, high vibration amplitudes are obtained for rotational speeds above 4300 rpm (72 Hz). The resonance frequency at 640 Hz is accompanied by second order harmonics and side harmonics indicating the presence of nonlinear effects. This resonance behaviour is not observed for the test rig with viscoelastic bearing supports. Clearly, the viscoelastic support ensures an effective vibration reduction, which in the case of the PMC 121/50 support is most effective.

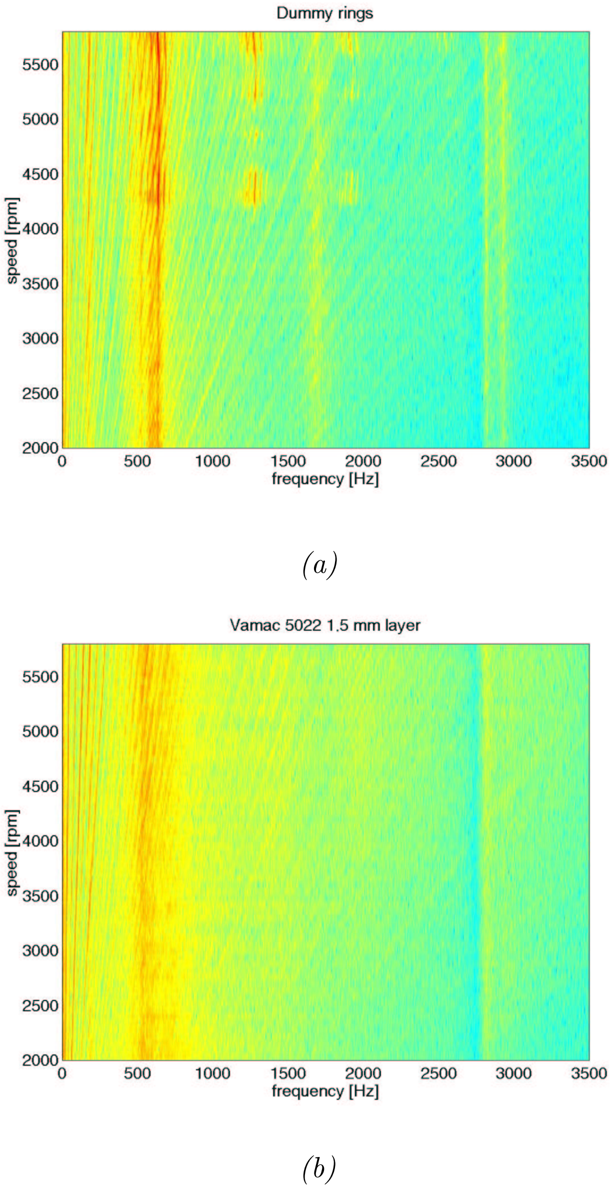

Figure 4.23: *Campbell diagram of the axial accelerations of the test rig housing with (a) dummy rings and (b) Vamac 5022 1.5 mm layers.*

In addition, clear excitation lines can be distinguished in Figure 4.23, which

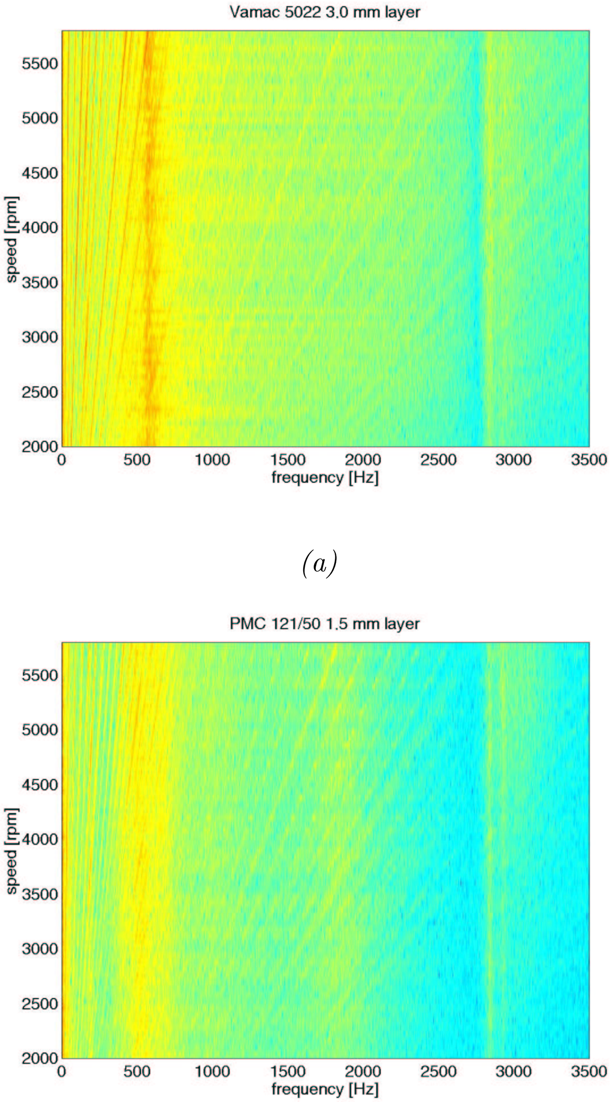

(a)

(b)

Figure 4.24: *Campbell diagram of the axial accelerations of the test rig housing with (a) Vamac 5022 3.0 mm layers and (b) PMC 121/50 1.5 mm layers.*

show up as order lines of the rotational speed. This indicates that the shaft imbalance is the main vibration exciter in the test rig. The results also indicate that the excitation levels measured for the test rig with Vamac 5022 layers (1.5 and 3.0 mm thickness) are somewhat higher than in the case of dummy rings and the PMC layer.

The rms velocity level of the measured spectra is determined as a function of the rotational speed, as presented in Figure 4.25.

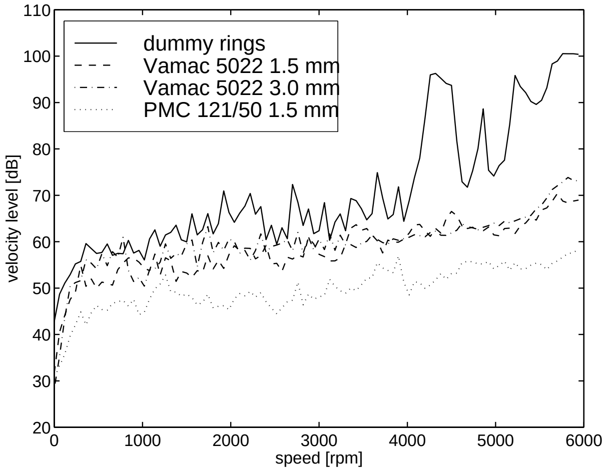

Figure 4.25: *Rms velocity level of the test rig housing as a function of the rotational speed.*

The results presented in Figure 4.25 demonstrate that the velocity levels are significantly reduced when a viscoelastic support is applied. Due to the increase of excitation level, the reduction is less clear for the Vamac 5022 materials. For high rotational speeds however, i.e. when resonance occurs for the test rig with dummy rings, the reduction still exceeds 10 dB.

4.6 Conclusions

The VICTORIA test rig has proven to be a valuable tool for investigating the dynamic behaviour of rotating machinery with viscoelastic bearing supports. The vibration damping and vibration isolation capabilities of the viscoelastic supports have shown to be effective in both non-rotating and rotating conditions.

The numerical model of the test rig was succesfully validated with an experimental modal analysis and FRF analysis of the non-rotating system. Also an acceptable agreement was obtained for the test rig with different viscoelastic layer configurations. It can be stated that the comparison between the measured and predicted results justifies the conclusion that the numerical model is suited to be used in design studies.

A significant vibration reduction was achieved for the test rig under operating conditions. This was shown in a running mode analysis and a Campbell diagram analysis. For the latter, it was observed that high amplitude resonance behaviour of the test rig with dummy rings completely disappears by adding a viscoelastic bearing support to the application. Certain trends in the dynamic behaviour of the system in running conditions are reasonably well predicted by the numerical model.

Chapter 5

Application: an electric motor

5.1 Introduction

In many household appliances, such as refrigerators, vacuum cleaners and air-conditioners, electric motors are applied. Often, the radiated noise of such electric motors is a nuisance to people living or working in the vicinity of the appliance. In the present investigation, a representative electric motor (see Figure 5.1) for air-conditioning applications is analysed. This particular motor was selected because it produces a significant amount of noise.

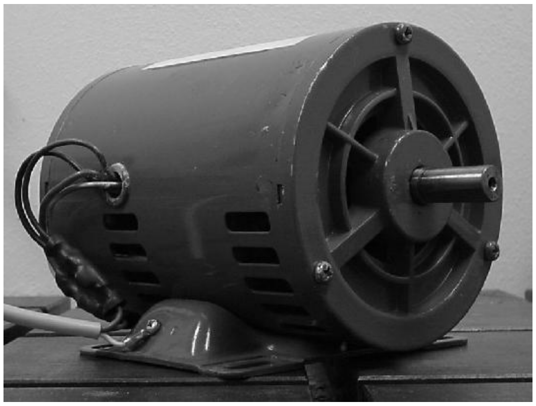

Figure 5.1: *An electric motor used in air-conditioning applications.*

The objective of this study was to reduce the radiated noise of the electric motor by the use of viscoelastic bearing supports. For this purpose, the sandwich rings tested in the VICTORIA test rig are also used in the electric motor. It should be emphasized that some fundamental differences exist between the test rig and the electric motor. First, the electric motor is geometrically much more complex than the test rig. Obviously, this makes it more difficult to construct a reliable structural model. Secondly, the excitation behaviour of the application differs. In the test rig, only imbalance and bearing forces occur, whereas in the electric motor also electromagnetic forces excite the system. The complexity of the geometry in combination with the excitation forces result in the generation of a broadband noise. This is in contrast with the VICTORIA test rig, which showed only a few main resonance frequencies.

The motor consists of four main components: the rotor, the stator-housing arrangement and two cover shields, as illustrated in Figure 5.2.

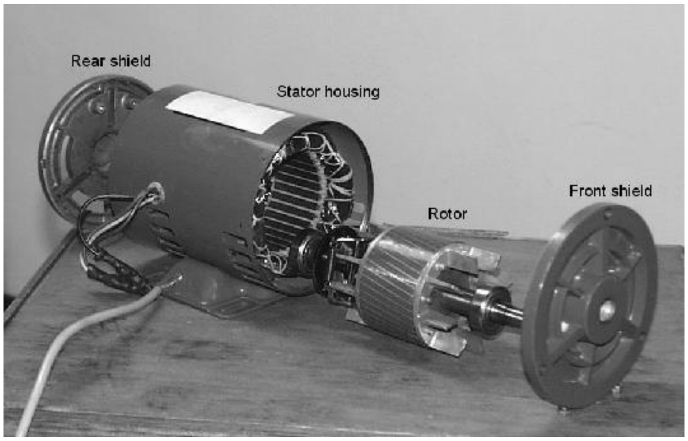

Figure 5.2: *Layout of the four main components of the electric motor.*

The rotor is supported by two deep groove ball bearings. In the assembly a spring is mounted between the front shield and the bearing outer ring ensuring the required preload. The motor is fixed to a rigid base by means of four bolts.

In this chapter first the excitation sources and the overall dynamic behaviour of the original electric motor under operating conditions are characterised (section 5.2).

A structural model of the application is presented in section 5.3. As with the VICTORIA test rig, the elastic components were modelled and validated individually before the assembled model was constructed. With the assembled model, modal and harmonic response analyses were performed. The structural model was validated with experiments consisting of modal analyses and running mode analyses. In addition, it will be shown that vibrations of the outer surface of the motor can be reduced reasonably well by a viscoelastic bearing support. The results of these analyses are discussed in section 5.4.

The complete modelling and validation procedure of the electric motor is illustrated in the diagram of Figure 5.3. In this diagram also acoustic analyses are indicated. These analyses form the subject of Chapter 6.

5.2 Preliminary analysis of the electric motor

In order to obtain insight into the overall dynamic behaviour of the electric motor, a set of exploratory measurements on the running motor were performed. As a result, both the vibration modes and the excitation frequencies of the system were identified. The vibration sources in the application are specific for electric motors and are addressed first.

5.2.1 Vibration source characterization

In rolling bearing applications, such as the VICTORIA test rig, vibrations are caused by the rotor imbalance and the rolling bearings. For an electric motor, additional vibrations are generated by the electromagnetic forces acting between the rotor and the stator. The tangential forces ensure the actual rotation of the rotor, but these forces are no important source of vibrations. A fluctuation of the radial electromagnetic forces, however, causes both the rotor and the stator to vibrate. This mechanism is explained with the help of Figure 5.4.

Under operating conditions, equal radial electromagnetic forces act along the circumference between the rotor and the stator. In perfect concentric conditions these forces are in balance. However, in the case of a small eccentricity of the rotor with respect to the stator, an air gap with variable thickness is created. As a result, a net radial force is generated near the smallest air gap acting simultaneously on the rotor and the stator. This

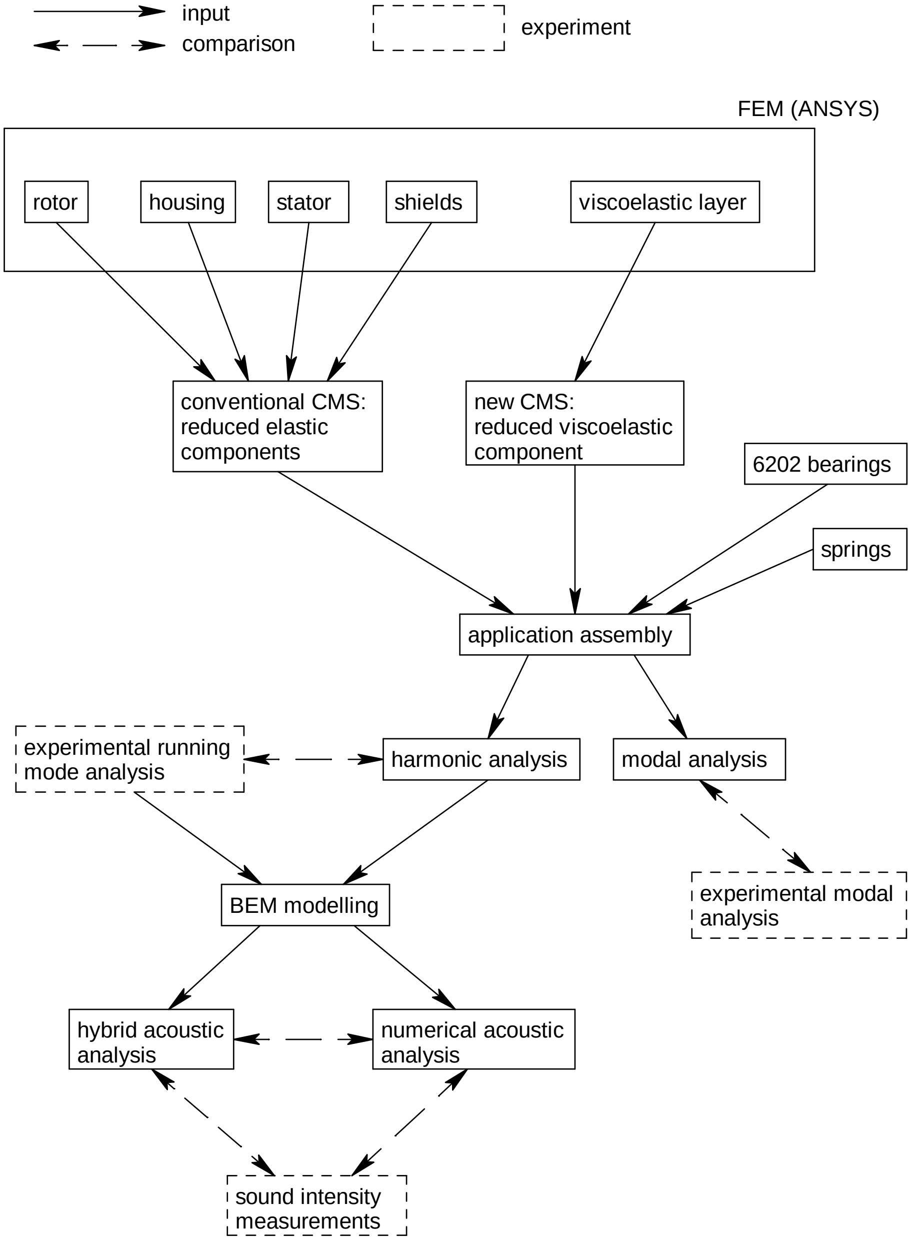

Figure 5.3: *Block diagram of the modelling procedure for the electric motor.*

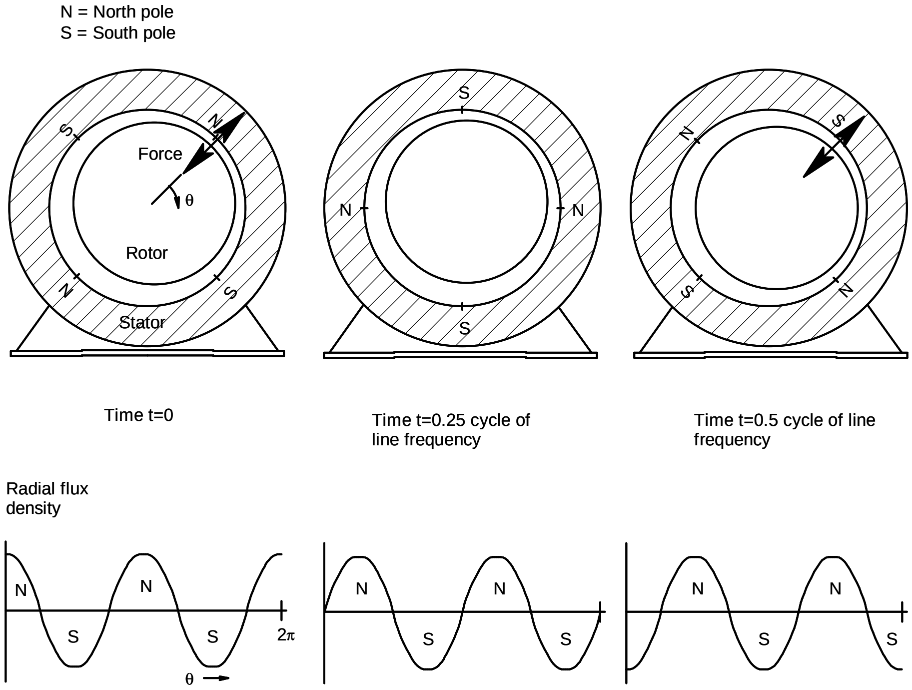

Figure 5.4: *Radially induced forces due to a rotor-stator eccentricity.*

force varies with time due to the rotation of the magnetic field of the stator. The latter is a result of the applied alternating net current with a frequency of 50 Hz. During one cycle of the line frequency one north and one south pole pass a point on the circumference, as illustrated in Figure 5.4. Therefore, the radial force fluctuates with a frequency of twice the line frequency equal to 100 Hz.
In the four-pole induction motor, one complete revolution of the magnetic field takes two cycles of the line frequency, resulting in a rotational speed of 25 Hz, i.e. 1500 rpm. Due to slip the actual rotational speed was found to be 24 Hz (1440 rpm).

The eccentricity between the stator and the rotor is a combination of a stator eccentricity and a rotor eccentricity. As a result of the stator eccentricity ε_s the airgap has a minimum thickness at a specific location around the circumference. Therefore, the resultant radial force F will have a strong directional character (see Figure 5.5a). If the eccentricity is caused by the rotor (ε_r), the minimum air gap and the corresponding radially induced force will rotate with the rotor speed of 24 Hz (Figure 5.5b). In reality, a combination of a directional force and a rotating force will occur. The induced force signals as a function of time t due to either a stator or a rotor eccentricity are shown in Figure 5.6.

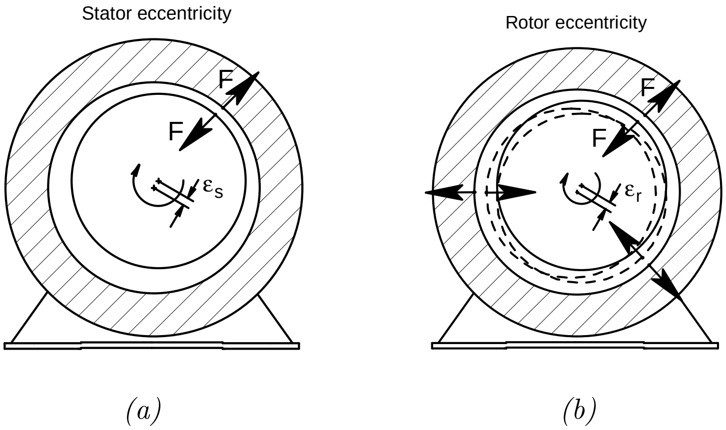

(a) *(b)*

Figure 5.5: *(a) Stator eccentricity and (b) rotor eccentricity.*

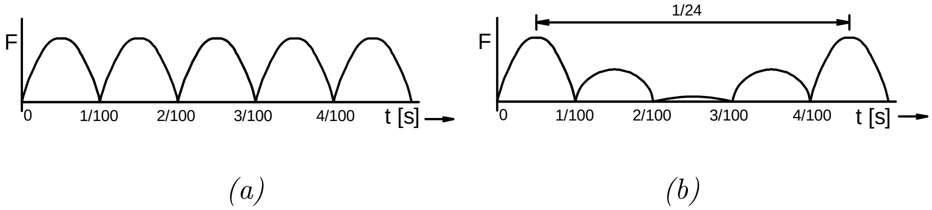

(a) *(b)*

Figure 5.6: *Force signal due to (a) stator eccentricity and (b) rotor eccentricity.*

Since the electromagnetic forces are the main sources of vibration, it can be expected that the dominating excitation frequencies be found at 100 Hz and its respective harmonics. In addition, due to the rotor imbalance, excitation peaks are expected at 24 Hz and higher harmonics. It is noted that the electromagnetic forces act both on the rotor and the stator. Consequently, the housing of the motor is excited indirectly via the path rotor-bearings-housing and directly via the stator. This is in contrast to the VICTORIA test rig, in which the housings are solely excited indirectly via the bearings, by the rotor. As a result, vibrations of the electric motor should not only be isolated but also damped by the viscoelastic bearing support. This aspect must be considered carefully in the design of the support.

5.2.2 Characterisation of electric motor vibrations

An experimental running mode analysis was performed to determine the response of the electric motor in running conditions. From this analysis the excitation frequencies can also be determined. The acceleration signals were measured on a 39 point grid of the motor housing, as shown in Figure 5.7. The node numbering of the grid is shown also, since in this chapter the response signals refer to several of these nodes. The LMS Cada-X system was used again for the signal analysis.

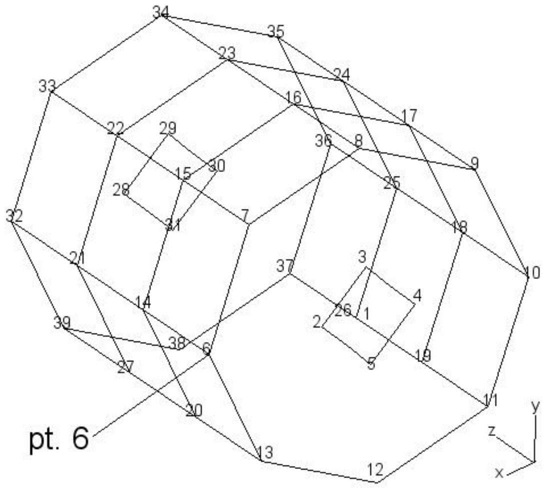

Figure 5.7: *Measurement grid of the electric motor.*

The measurement grid is suited to determine the vibration modes in the frequency range of interest, i.e. from 0 to 5 kHz. The frequency spectra of the acceleration cross-power between each gridpoint and the reference point (point 6) are summed over the gridpoints. The result is shown in Figure 5.8. For the sake of clarity, the spectra are given for frequency ranges from 0 to 500 Hz (zoom-in) and from 0 to 3000 Hz.

In Figure 5.8 clear excitation frequencies show up at 24 Hz and its harmonics, indicating the rotor imbalance. The spectrum is dominated, however, by 100 Hz peaks and its harmonics. This justifies the assumption that the electromagnetic forces are the main sources of excitation in this application. Note that a small contribution near the 100 Hz peaks can be caused by har-

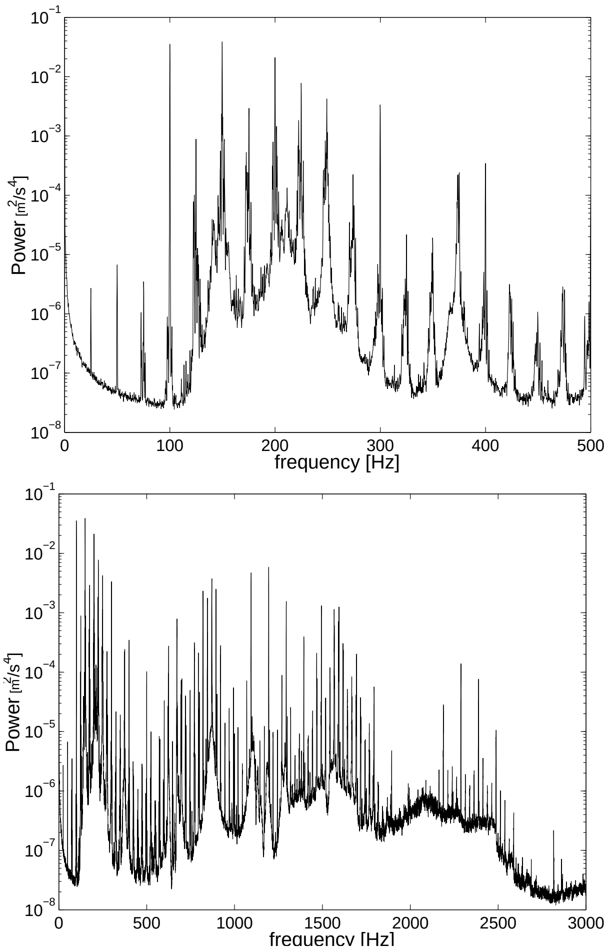

Figure 5.8: *Sum of the (absolute) cross-power spectra of the electric motor in a frequency range from 0 to 500 Hz (top) and from 0 to 3000 Hz (bottom).*

monics of 24 Hz. As the mass and stiffness of the rotor and of the stator are of the same order of magnitude, it can be expected that both components be excited at similar response levels.

Secondly, an underlying curve is visible in Figure 5.8 showing several resonance frequencies in the frequency range of interest. Some of the characteristic vibration modes are presented in Figure 5.9.

At up to about 1 kHz the vibration modes are all modes of the cylindrical housing moving relative to the foot of the motor, which is fixed to the

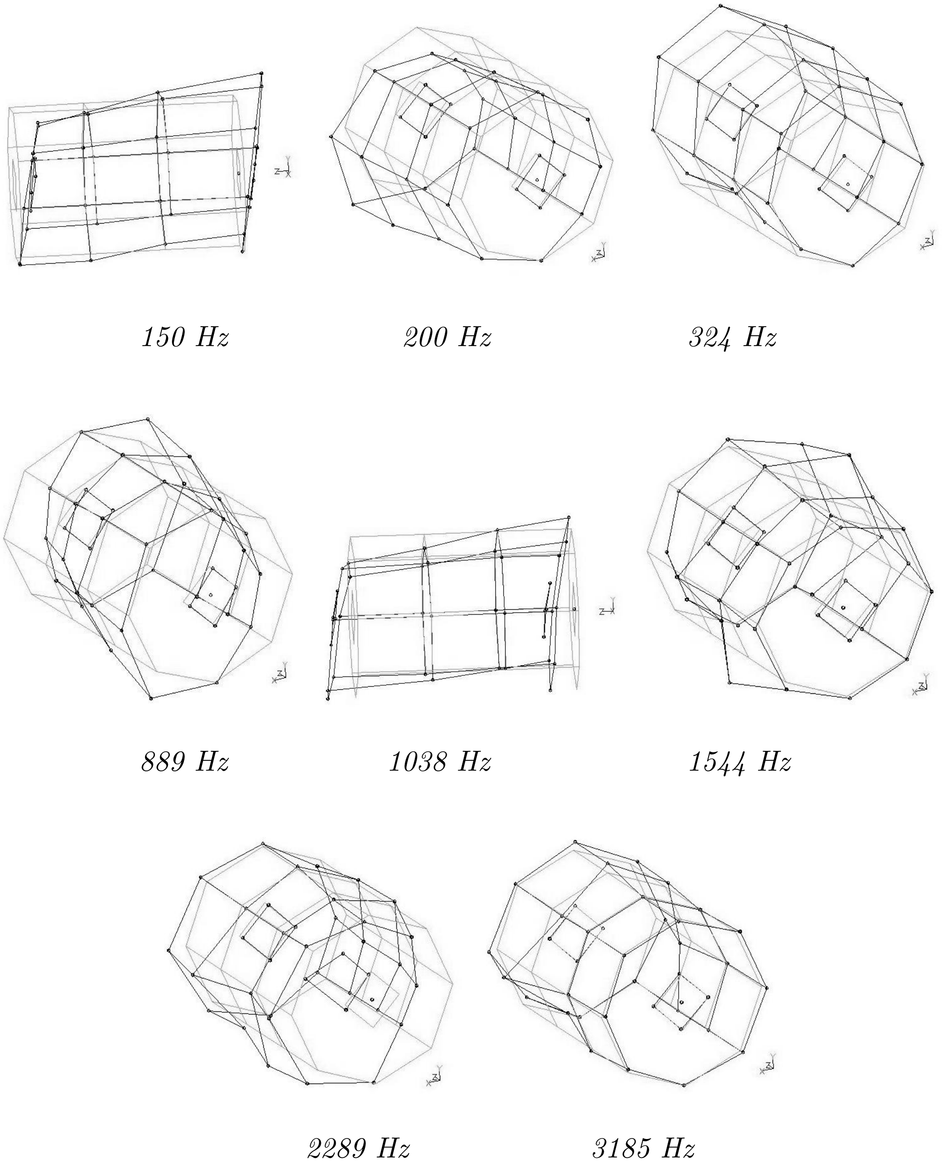

150 Hz *200 Hz* *324 Hz*

889 Hz *1038 Hz* *1544 Hz*

2289 Hz *3185 Hz*

Figure 5.9: *A selection of measured vibration modes of the electric motor during a running mode analysis.*

ground. For higher frequencies the flexibility of the housing starts to play a significant role. It is noted, however, that each mode is accompanied by a deformation of the shaft, which was not measured during the running mode analysis.

From these results it can be concluded that the electric motor is excited over a broad frequency range, mainly by the electromagnetic forces acting on the stator and the rotor. As the housing is directly excited via the stator, vibration isolation via the bearings will become less effective than in the VICTORIA test rig. The rotor vibrations, however, can still be isolated with a viscoelastic bearing support. Finally, it is to be expected that a viscoelastic support will affect the level of the excitation forces in the electric motor.

5.3 Structural model of the electric motor

The procedure to model the structure of the electric motor is similar to the one followed for the test rig as explained in Chapter 4.

The electric motor contains four elastic components that were modelled with FEM, i.e. the rotor, the stator-housing and the two cover shields. The stator-housing arrangement is a rather complex component and is therefore subdivided into a cylindrical casing, the stator and the foot. The geometry of these components was described in the solid-modelling package Pro-Engineer, after which the data was imported and meshed in the FEM program ANSYS.

5.3.1 Rotor

The rotor contains components made of three different materials: the aluminium cooling fins, a steel shaft and a soft iron core. The shaft-core assembly is considered as a single volume and the material is given a mean Young's modulus of 165 GPa. A modal analysis of the rotor in free-free conditions showed that the eigenfrequencies of up to 5 kHz are accurately predicted, as indicated in Table 5.1. The average (absolute) difference between measurement and prediction was 4.2 %.

nr.	mode	experiment	FEM	difference [%]
1	1st bending	1551	1624	4.7
2	2nd bending	2345	2430	3.6

Table 5.1: *Eigenfrequencies of the rotor.*

5.3.2 Cover shields

The front and rear cover shields are made of aluminium. As the shields are not completely identical, separate FEM models were created. It was found that the eigenfrequencies are well predicted up to 5 kHz, as shown in Tables 5.2 and 5.3. The average deviation from the measured eigenfrequencies is 3.6 % and 2.8 % for the front and rear shield, respectively.

nr.	mode	experiment [Hz]	FEM [Hz]	difference [%]
1	1st flexural	2313	2299	-0.6
2	Axial	3753	3567	-5.0
3	2nd flexural	5020	5358	6.7
4	3rd flexural	5246	5143	-2.0

Table 5.2: *Eigenfrequencies of the front shield.*

nr.	mode	experiment [Hz]	FEM [Hz]	difference [%]
1	1st flexural	2314	2445	5.7
2	Axial	3748	3744	0.1
3	2nd flexural	4690	4630	1.3
4	3rd flexural	4960	5152	3.9

Table 5.3: *Eigenfrequencies of the rear shield.*

In order to implement a viscoelastic bearing support, the cover shields had to be redesigned. New cover shields were manufactured which, in comparison with the original shields, have a simplified geometry (see Figure 5.10). The shields were designed in such a way that the sandwich rings that were used for the VICTORIA test rig can also be applied in this motor.

Figure 5.10: *The original (left) and the new (right) cover shield.*

The mass and stiffness properties were kept similar to those of the original shields. As a result, the eigenfrequencies of the new shields differ at most by 10 % from the ones of the original shields (compare Tables 5.4 and 5.2). A modal analysis showed an average error between the measured and predicted eigenfrequencies of the new shields of only 1.9 %.

nr.	mode	experiment [Hz]	FEM [Hz]	difference [%]
1	1st flexural	2077	2195	5.7
2	Axial	3807	3794	-0.3
3	2nd flexural	4982	5053	1.4
4	3rd flexural	5290	5289	0.0

Table 5.4: *Eigenfrequencies of the new shields.*

5.3.3 Stator-housing arrangement

The steel cylindrical casing contains a thin aluminium flange on the inner surface, which as a combination was modelled with FEM. To facilitate the FEM modelling process and to introduce some flexibility at the component interfaces, the stator and the foot were modelled in FEM separately (see Figure 5.11 for the stator-housing components).

The stator consists of a densely packed pile of steel plates and an iron core with copper wires. It is modelled as a solid component with a material

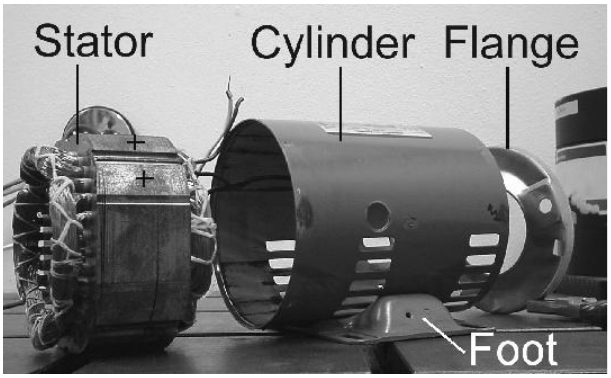

Figure 5.11: *Components of the stator-housing arrangement.*

density, such that it matches the measured mass. Young's modulus is estimated at 70 GPa. However, due to its rigidity the stiffness of the stator hardly affects the overall dynamic behaviour of the motor. Between the stator and the casing a single rigid interface is defined.

The foot is made of steel and was modelled with FEM. As the foot is welded to the casing at six points, the interfaces were defined at those specific locations. In the assembled model, springs were added at these interfaces to create the freedom to adjust the stiffness of the foot-casing arrangement (see Figure 5.12).

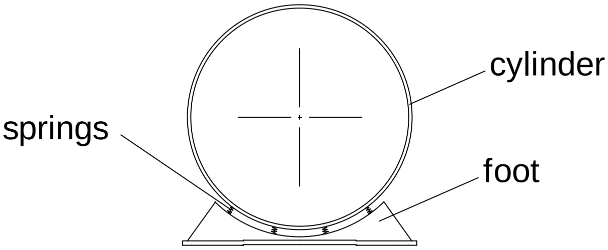

Figure 5.12: *Connection of the foot to the cylinder by springs.*

To validate the stator-housing model, measurements were performed on the assembly of the stator-housing with cover shields. In the real motor, the shields were fixed to the housing at three bolt positions equally distributed along the circumference. In the model the shields were not only fixed at the bolt positions. Between the bolts simple springs were added (as illustrated in Figure 5.13) to model the stiffness caused by the contact between the shields and the housing. The springs were assigned a constant stiffness such that the average agreement between the predicted and measured eigenfrequencies was optimised. The foot was fixed to the ground.

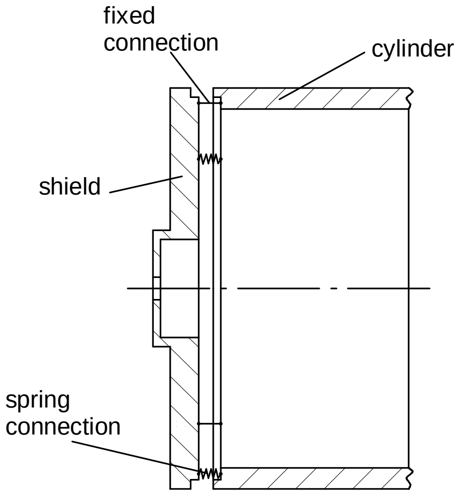

Figure 5.13: *Connection of the shield to the housing.*

The modal analysis showed a good agreement between the measured eigenfrequencies and those obtained with the tuned model up to 1 kHz and a reasonable agreement for the eigenfrequencies between 1 kHz and 3 kHz. Overall, an average deviation of 13.3 % and 14.4 % was obtained for the system with the original and new cover shields, respectively.

The eigenfrequencies of the system with either original or new cover shields are nearly equal. Only the eigenfrequencies corresponding with modes dominated by displacements of the shields will differ. In general, it was found that the influence of the new shields on the overall dynamic and acoustic behaviour of the electric motor was very small. Therefore, in further analyses only the system with the new cover shields is considered.
It should be noted that many eigenfrequencies of the flexible housing occur between 3.0 kHz and 5.0 kHz, both for the model and in the experiments. These eigenfrequencies, however, correspond with flexural eigenmodes of

nr.	mode	experiment [Hz]	model [Hz]	difference [%]
1	rocking	196	192	2.1
2	1st rolling	233	231	-0.9
3	jumping	475	479	0.8
4	1st twisting	1045	973	-7.4
5	2nd rolling	1392	1739	24.9
6	swing	1404	1471	4.6
7	flexural house	1542	2156	39.8
8	2nd twisting	2282	2817	23.4
9	axial shield	2620	2461	-6.5
10	ovality house	2630	2910	10.7
11	triangle house	2922	3668	25.5

Table 5.5: *Eigenfrequencies of the stator-housing arrangement with the original cover shields.*

nr.	mode	experiment [Hz]	model [Hz]	difference [%]
1	rocking	194	179	-8.4
2	1st rolling	233	227	-2.6
3	jumping	475	476	0.2
4	twisting	1034	937	-10.4
5	2nd rolling	1355	1725	27.3
6	swing	1404	1445	2.8
7	flexural house	1555	2157	38.7
8	2nd twisting	2319	2844	22.6
9	ovality house	2632	3097	17.7
10	axial shield	2750	2754	0.1
11	triangle house	2913	3725	27.9

Table 5.6: *Eigenfrequencies of the stator-housing arrangement with the new cover shields.*

the thin cylinder, which are difficult to determine in the experiments. At this point, these eigenfrequencies cannot be compared directly with the predicted eigenfrequencies in this frequency range.

5.3.4 Electric motor assembly

In the assembled model, two standard deep groove ball bearings and a preloading spring were added. An overview of the models of the structural components and the complete assembly is illustrated in Figure 5.14.

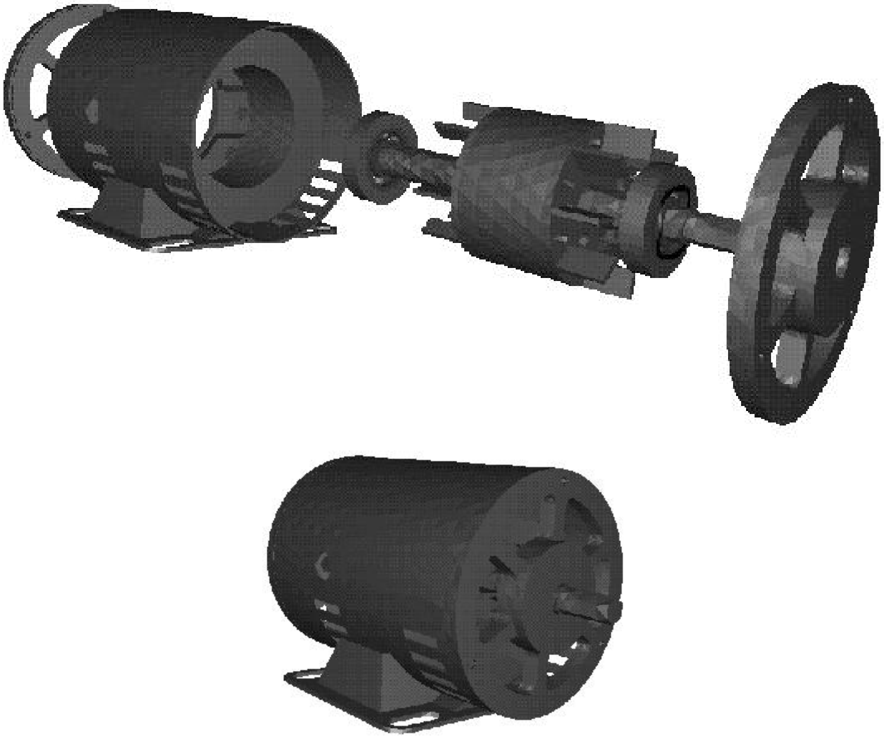

Figure 5.14: *Structural model of the electric motor.*

In the model the displacements of the foot were suppressed at the bolt positions. The preloading spring provides a 75 N preload ensuring permanent contact between the rolling elements and the raceway of the bearing. For this purpose, the right-hand bearing outer ring was left free in the axial direction. The complete model has 250 degrees of freedom.

5.4 Experimental validation of the structural model of the electric motor

5.4.1 Modal analysis

The structural model of the assembled electric motor was validated by means of a modal analysis, using the LMS Cada-X system. The most important eigenfrequencies and corresponding eigenmodes were determined up to about 3.0 kHz and are presented in Figures 5.15 and 5.16. In this case the electric motor with new shields and steel dummy rings between the bearings and the shields is considered.

An acceptable agreement, i.e. an average deviation of 12.3 %, between the calculated and measured eigenfrequencies was obtained. It can be observed that for some modes the difference in eigenfrequency is quite small when compared to the eigenfrequencies of the stator-housing assembly (Table 5.6).

Similar modal analyses were performed for the electric motor with viscoelastic bearing supports, for which the results are shown for the eigenmodes 2 to 8 in Figure 5.17. Note that two types of viscoelastic material are applied in the sandwich rings, i.e. Vamac 5022 and PMC 121/50. The thickness of the viscoelastic layers is 1.5 mm.

It can be observed that most of the eigenfrequencies are hardly affected by the presence of a (soft) viscoelastic bearing support. In fact, only the bearing support with a 1.5 mm viscoelastic layer of the PMC 121/50 material has some effect, mainly for the eigenmodes accompanied by a shaft bending (modes 4, 5 and 6). The latter effect is reasonably well predicted.

During the modal analyses FRFs were determined as a result of a vertical impact on the housing. The FRFs were also determined numerically via a harmonic response analysis. In Figure 5.18 the predicted and measured (vertical) FRF of point 8 on an impact hit on the same point in the vertical direction is shown for the motor with different bearing supports.

From this figure it can be observed that the agreement between prediction and measurement is good up to 1 kHz. For higher frequencies, however, the agreement becomes less consistent. The predicted resonance frequency around 1200 Hz, for example, is hardly excited in the actual system at 1035 Hz. This can be caused by the fact that for the measured system two resonance frequencies at 868 Hz and 1035 Hz are close to each other. For the prediction, the same eigenmodes are excited at 769 Hz and 1210 Hz. The trends in the FRFs with respect to different bearing supports are well

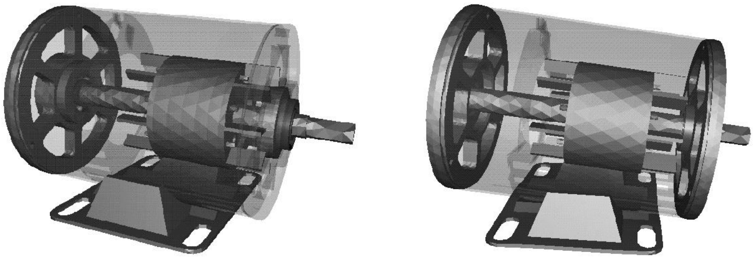

1: axial rotor
calc. 79 Hz
meas. 71 Hz

2: rocking
calc. 171 Hz
meas. 182 Hz

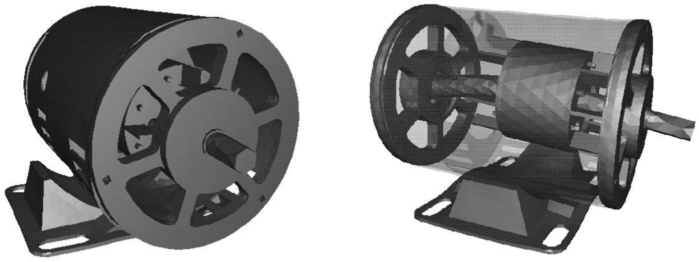

3: 1st rolling
calc. 195 Hz
meas. 201 Hz

4: 1st jumping
calc. 345 Hz
meas. 336 Hz

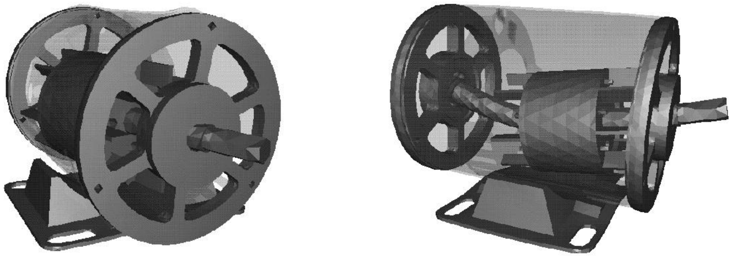

5: 2nd rolling
calc. 554 Hz
meas. 520 Hz

6: 2nd jumping
calc. 656 Hz
meas. 642 Hz

Figure 5.15: *A selection of eigenmodes of the electric motor with new shields and dummy rings.*

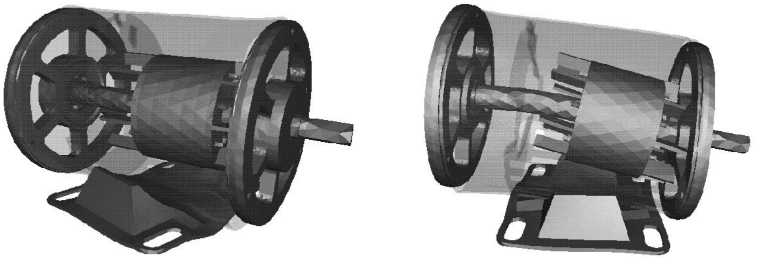

7: twisting
calc. 769 Hz
meas. 868 Hz

8: swinging
calc. 1210 Hz
meas. 1035 Hz

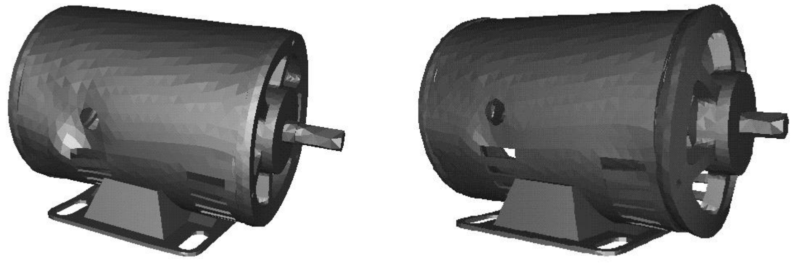

9: flexural house
calc. 2168 Hz
meas. 1525 Hz

10: axial shield
calc. 2096 Hz
meas. 1765 Hz

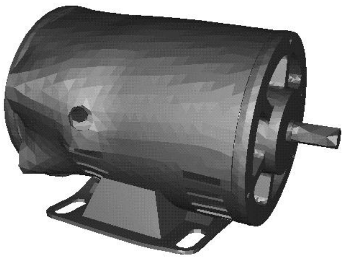

11: ovality house
calc. 3137 Hz
meas. 2626 Hz

Figure 5.16: *A selection of eigenmodes (cont.) of the electric motor with new shields and dummy rings.*

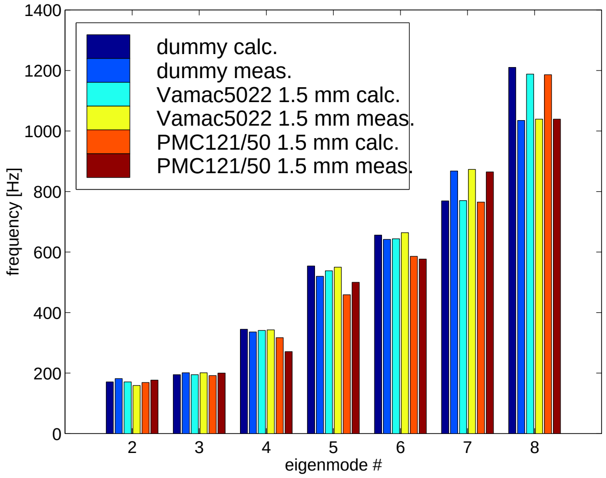

Figure 5.17: *Eigenfrequencies of the electric motor with various bearing supports.*

predicted.

Overall, it can be concluded that the structural model of the electric motor is validated in a rather satisfactory way.

5.4.2 Running mode analysis

In order to design an effective viscoelastic bearing support for the electric motor, the sources of excitation of the motor should be accurately modelled. An accurate description of the bearing forces, the rotor imbalance and the electromagnetic forces in the electric motor requires a transient analysis. It is, however, very difficult to determine the exact excitation forces beforehand, both theoretically and experimentally. Moreover, a transient analysis makes the design process of a viscoelastic bearing support very time consuming.

In this study, we attempted to simulate the dynamic behaviour of the running electric motor with the help of a harmonic response analysis. It was assumed that harmonic forces act both on the rotor and the stator (equal amplitude but in counter-phase) in the diagonal radial direction, see Figure

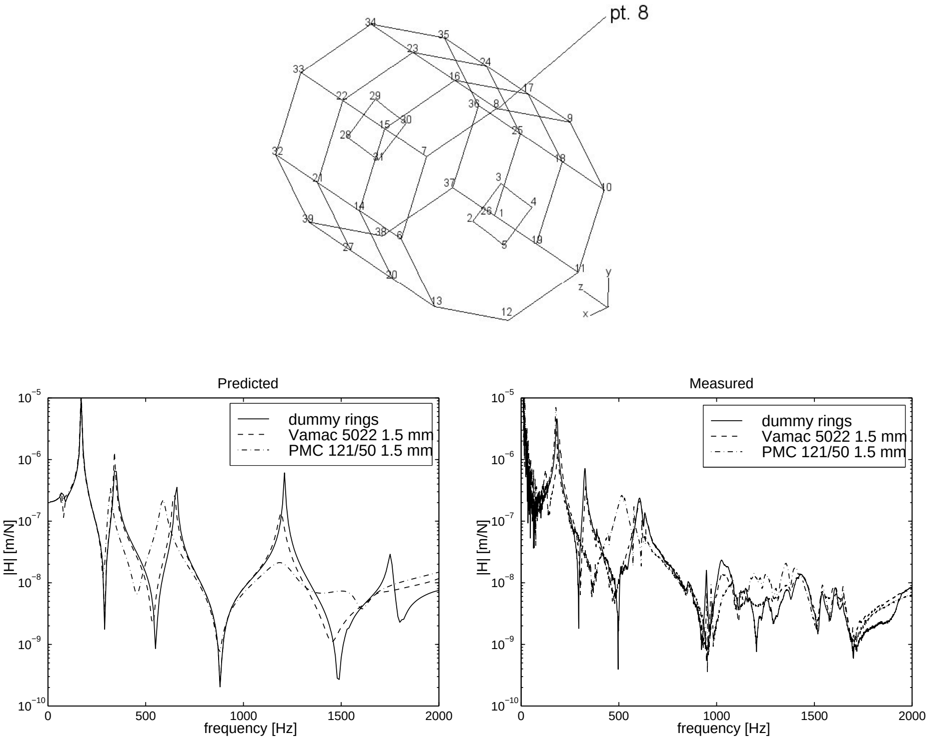

(a) (b)

Figure 5.18: *(a) Predicted and (b) measured FRF of the housing top (pt. 8) on a vertical impact force on the same point.*

5.19. From a set of preliminary measurements and calculations this representation was found most acceptable to provide the best agreement between the experiments and the model.

The force amplitude F was determined as a function of frequency in an inverse way by using the measured acceleration data on the motor surface in combination with the calculated transfer functions between the force and a number of response locations:

$$F = \frac{1}{N} \sum_{i=1}^{N} \frac{a_{X_i}}{H_{FX_i}} \tag{5.1}$$

Here a_{X_i} is the measured acceleration spectrum at point X_i, H_{FX_i} is the transfer function between the applied force and point X_i and N denotes

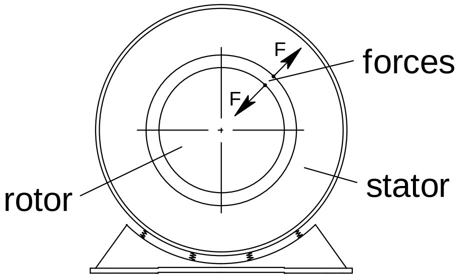

Figure 5.19: *Harmonic forces acting both on the rotor and the stator.*

the total number of points used for averaging. A total of 14 points over the surface was used in the analysis. The resulting force spectra are shown in Figure 5.20. The frequency resolution was reduced to 25 Hz, in order to save computation time in the harmonic and acoustic analyses that will follow.

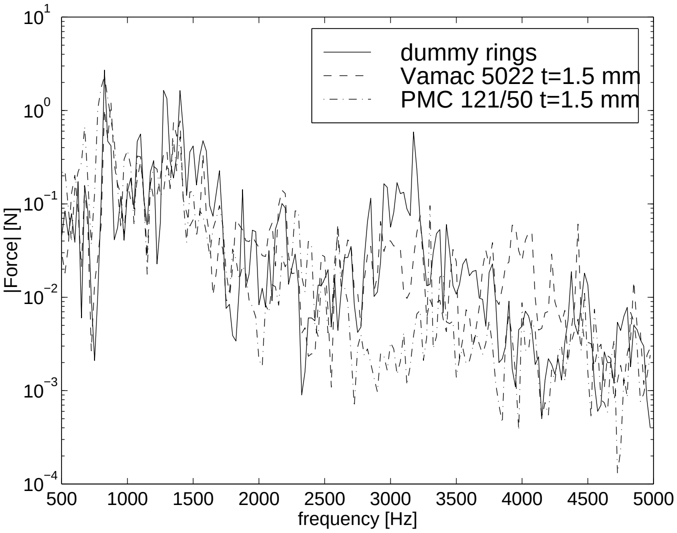

Figure 5.20: *Calculated force spectra of the electric motor using measured acceleration data.*

Clearly, the excitation forces depend on the type of bearing support. In the frequency range of up to about 2.5 kHz the forces behave in roughly the same way. For higher frequencies, however, the forces in the case of the PMC 121/50 support are considerably lower. In the case of the Vamac 5022 support the high frequency forces are slightly higher than for the PMC 121/50 support. The latter can probably be attributed to the relatively large eccentricity of the sandwich rings with the Vamac 5022 material.

The acceleration spectra of point 8 (radial direction) obtained with the help of a harmonic analysis with the frequency dependent forces are shown in Figure 5.21.

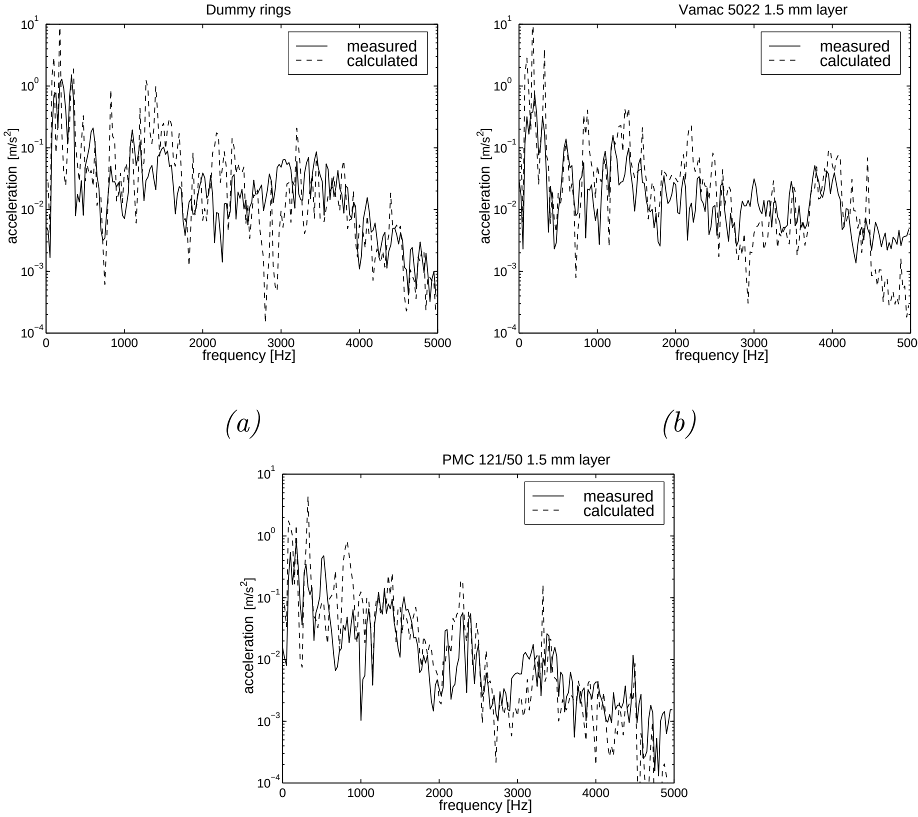

(a) *(b)*

(c)

Figure 5.21: *Measured and calculated acceleration spectra of point 8 for the electric motor with (a) dummy rings, (b) Vamac 5022 1.5 mm layer and (c) PMC 121/50 1.5 mm layer.*

The comparison between the calculated spectra and the measured spectra reveals a reasonable agreement. This means that the overall response level and the general trends in the spectra are well predicted. Thus, it can be concluded that a structural model of an electric motor with a combined experimental-numerical excitation model is well-suited to be used for design studies. As such, it has been applied with regard to the acoustic behaviour of the motor (Chapter 7).

Finally, the results of the running mode analyses for electric motors with viscoelastic bearing supports are presented. In Figures 5.22 and 5.23 the measured velocity spectra of the electric motor with dummy rings and with viscoelastic bearing supports are compared. The responses of points 2 (axial direction) and 23 (radial direction) are considered.

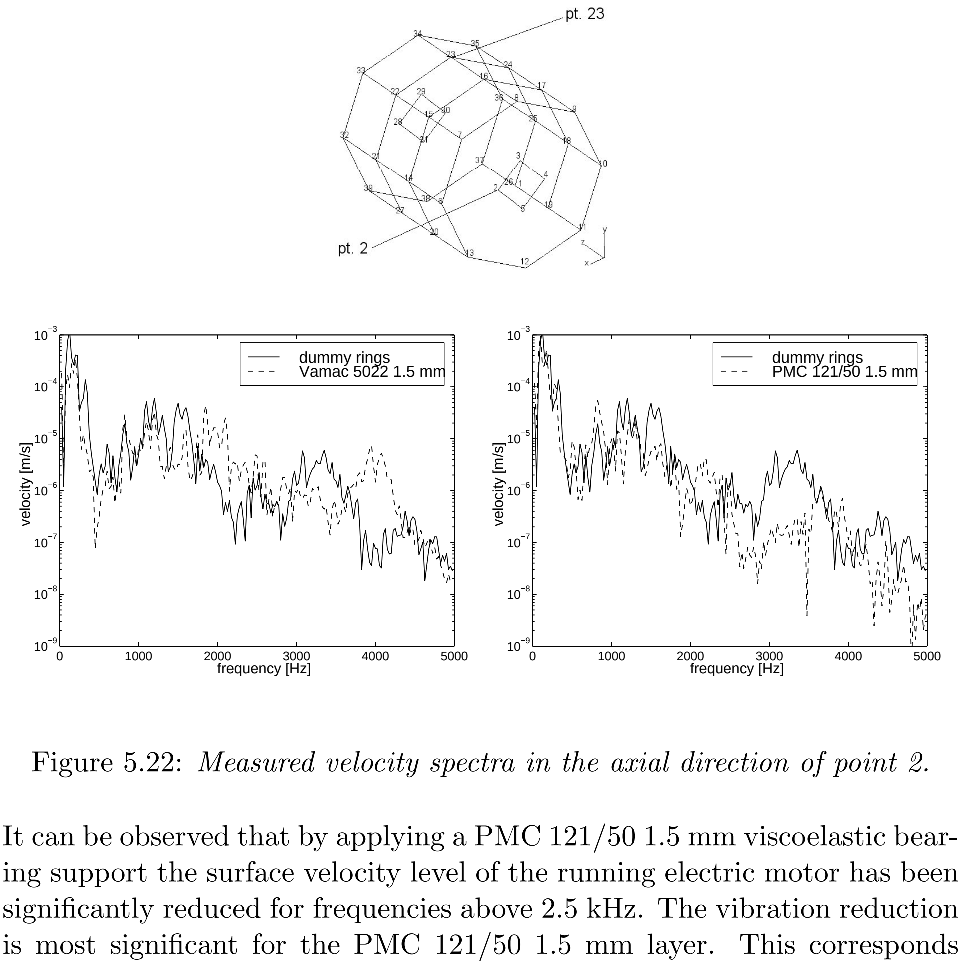

Figure 5.22: *Measured velocity spectra in the axial direction of point 2.*

It can be observed that by applying a PMC 121/50 1.5 mm viscoelastic bearing support the surface velocity level of the running electric motor has been significantly reduced for frequencies above 2.5 kHz. The vibration reduction is most significant for the PMC 121/50 1.5 mm layer. This corresponds

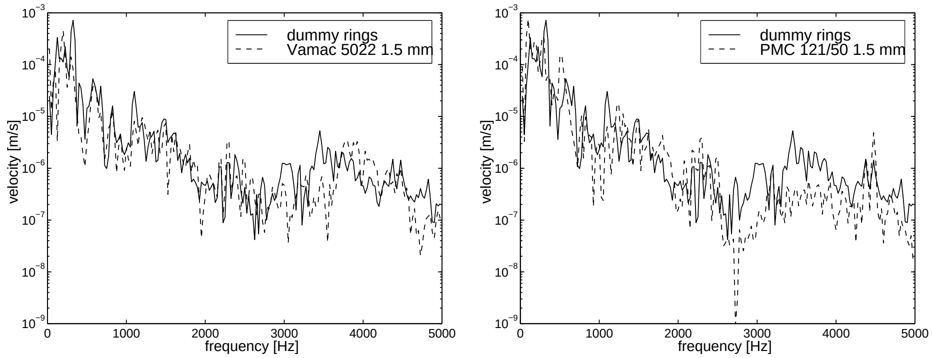

Figure 5.23: *Measured velocity spectra in the axial direction of point 23.*

with the conclusion drawn earlier for the application of this layer in the VICTORIA test rig (section 4.5).

5.5 Conclusions

From the investigations performed on the electric motor the following conclusions can be drawn:

First, it was found experimentally that the electric motor is excited over a broadband frequency range, mainly by electromagnetic forces acting between the rotor and the stator. This means that it is important not only to create vibration isolation but also vibration damping, because the housing is directly excited via the stator. The latter can be rather difficult with only a small piece of damping material in the vicinity of the bearings.

A structural model of the electric motor was successfully validated with modal measurements. In operating conditions, the vibration behaviour of the electric motor can be simulated efficiently by a harmonic response analysis. With some assumptions made for the force locations and directions, the harmonic forces can be obtained by combining the measured acceleration data across the motor surface and the predicted frequency response functions.

The excitation forces in the electric motor strongly depend on the type of bearing support. The eccentricity of the support with respect to the centre of rotation of the rotor mainly determines the level of excitation. The high frequency excitation forces, however, can be reduced by a viscoelastic bearing support. This was observed in particular for the electric motor with PMC 121/50 layers.

An effective vibration reduction of the running electric motor could be achieved in the high frequency range above 2 kHz by application of a PMC 121/50 1.5 mm viscoelastic bearing support.

Chapter 6

On the acoustic behaviour of the electric motor

6.1 Introduction

It was shown in the preceding chapters that the structural dynamic behaviour of a rotor dynamics application can be predicted in a satisfactory way. However, the structural vibration level does not bear a one-to-one relation to the sound level generated by the vibrating structure. Vibration modes may exist that do not radiate noise at all. Therefore, it is essential to consider the acoustic behaviour of a system as well.

This chapter describes a combined experimental and numerical study on the acoustic behaviour of the running electric motor. For this purpose, predictive acoustic analyses were performed using the so-called Boundary Element Method (BEM). In this method the radiating surface of a structure is subdivided into elements. By introducing the normal velocities on the surface as a boundary condition the resulting acoustic field can be calculated. For convenience of the reader a survey of the governing equations and implementation of BEM is given in Section 6.2.

For our electric motor a BEM model was constructed, with which the radiated acoustic power is calculated. As input for the acoustic calculations, both measured and calculated structural response data were used. The measured response data were used for an explicit validation of the BEM model only. Therefore, a distinction is made between a hybrid acoustic approach, i.e. the combination of measured input and a numerically predicted sound power level, and a (fully) numerical acoustic approach, see Section 6.3.

In Section 6.4 the experiments are described which were carried out to characterise the overall noise level of the application. For that purpose, sound intensity measurements were done.
The acoustic models were validated with sound intensity measurements on the running electric motor of which the results are discussed in Section 6.5. It will be shown that even with a simple BEM model it is possible to determine the broadband radiated noise of a complex rotor dynamics application.

The acoustic investigations are summarised in the block diagram of Figure 6.1.

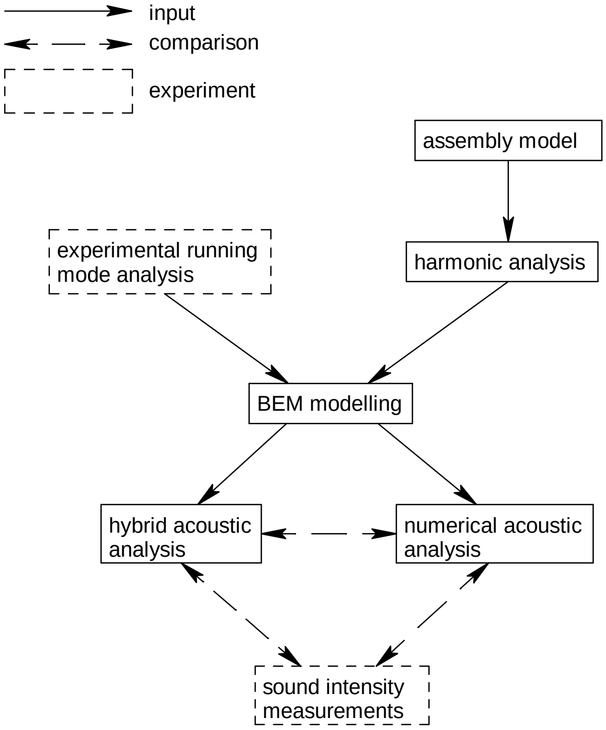

Figure 6.1: *Block diagram of the acoustic investigations on the electric motor.*

6.2 Prediction of the acoustic behaviour

Acoustic waves induced by a vibrating object are characterised by a pressure perturbation $\tilde{p}$ and a velocity perturbation vector $\tilde{\vec{v}}$:

$$\tilde{p}(t) = Re(p \cdot e^{i\omega t}), \qquad \tilde{\vec{v}}(t) = Re(\vec{v} \cdot e^{i\omega t}) \tag{6.1}$$

Pressure fluctuations of these waves in the frequency range between 16 Hz and 16 kHz are perceived by the human ear as audible sound.

Sound is often represented by the sound pressure level, a quantity which depends on the source, the distance to the source and the acoustic properties of the environment. Another quantity that is often used in acoustics is the sound intensity level, which is proportional to the square of the sound pressure in the far field under free field conditions. The sound intensity integrated over a surface area enclosing the source is known as the sound power. The advantage of the sound power is the independence of the acoustic environment. Therefore, it is a good measure for the acoustic performance of an application.

In the case of harmonic pressure perturbations, the time-averaged radiated sound power is defined in the frequency domain as:

$$\bar{W} = \int\limits_S \bar{\vec{I}} \cdot \vec{n} dS \tag{6.2}$$

with $\bar{\vec{I}} = \frac{1}{2} Re(p\vec{v}^*)$ as the time-averaged acoustic intensity, where * denotes the complex conjugate and the bar notation $^-$ the time average. S is a (hypothetical) surface enclosing the vibrating object. The vector normal to the surface S is denoted by $\vec{n}$. Using the normal velocity $v_n = \vec{v} \cdot \vec{n}$, the expression is formulated as:

$$\bar{W} = \frac{1}{2} Re \int\limits_S p v_n^* dS \tag{6.3}$$

Because the sound intensity, sound pressure and sound power can vary over a wide range, the acoustic quantities are scaled logarithmically with a reference level corresponding to the threshold of the human ear. The sound intensity level, denoted as L_I, reads:

$$L_I = 10 \log \frac{\bar{\vec{I}}}{I_0}, \qquad I_0 = 10^{-12} \frac{W}{m^2} \tag{6.4}$$

The sound pressure level L_p and sound power level L_W are defined in a similar way as:

$$L_p = 20 \log \frac{p}{p_0}, \qquad p_0 = 20 \cdot 10^{-6} Pa \tag{6.5}$$

$$L_W = 10 \log \frac{\bar{W}}{W_0}, \qquad W_0 = 10^{-12} W \tag{6.6}$$

As the human hearing is not equally sensitive to all frequencies, a weighting function is usually applied to the acoustic levels. For moderate noise levels the so-called A-weighting function usually provides satisfactory results. A C-weighting function is used for very loud or low frequency sound. The A-, C- and linear-weighting curves are shown in Figure 6.2.

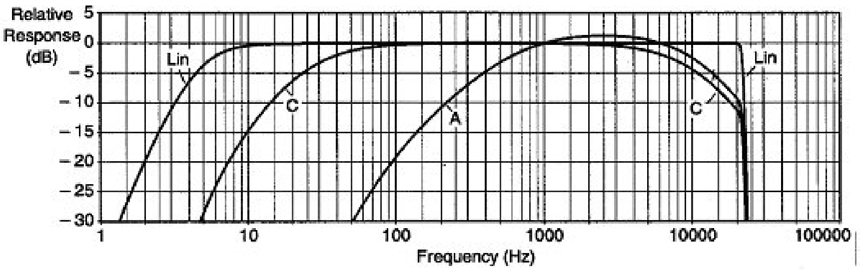

Figure 6.2: *The A-, C- and linear-weighting curves (source Barber, 1992).*

It is noted that the A-weighting function exceeds unity in the frequency range from 1 to 6 kHz. A-weighted sound levels are expressed in terms of unity dB(A).

6.2.1 Boundary element method

The sound pressure and sound power level were determined using the boundary element method (BEM), a widely used method in engineering acoustics (Ciskowski and Brebbia, 1991; Kirkup, 1998). An important advantage of the boundary element method compared to the finite element method is that it suffices to cover only the radiating surface of the vibrating object with elements. Therefore, it is very efficient for external radiation problems.

The equation which forms the basis of the boundary element method is the so-called Kirchhoff-Helmholtz integral equation. This equation relates the pressure perturbation in the acoustic domain, $p(\vec{x})$, with the pressure on the surface, $p(\vec{x}_s)$, and the velocity component, $v_n(\vec{x}_s)$, normal to the surface:

$$C(\vec{x}) \cdot p(\vec{x}) = \int_S [p(\vec{x}_s)\nabla G(\vec{x},\vec{x}_s) \cdot n(\vec{x}) + i\rho_0\omega G(\vec{x},\vec{x}_s)v_n(\vec{x}_s)]dS(\vec{x}_s) \quad (6.7)$$

where ρ_0 is the density of the acoustic medium and ω the angular frequency. $C(\vec{x})$ is a coefficient depending on the position of $\vec{x}$. $C(\vec{x}) = 1$ for a point in the acoustic domain and $C(\vec{x}) = 0.5$ for a point on the (smooth) surface S. $G(\vec{x},\vec{x}_s)$ is Green's function. This function satisfies the so-called Sommerfeld condition, ensuring that all acoustic waves propagate freely towards infinity and that no reflections occur into the considered acoustic domain. For a 3-dimensional infinite domain Green's function is given by:

$$G(\vec{x},\vec{x}_s) = \frac{e^{-ik|\vec{x}-\vec{x}_s|}}{4\pi|\vec{x}-\vec{x}_s|} \quad (6.8)$$

where $k = \omega/c_0$ denotes the free field wavenumber, with c_0 the velocity of sound in the medium.

In some cases the vibrating object, such as an electric motor, is placed on a rigid floor. In that case, the acoustic domain is represented by a 3-dimensional infinite half-space. Green's function for half-space problems reads (Ciskowski and Brebbia, 1991):

$$G(\vec{x},\vec{x}_s) = \frac{e^{-ik|\vec{x}-\vec{x}_s|}}{4\pi|\vec{x}-\vec{x}_s|} + r_H\frac{e^{-ik|\vec{x}_m-\vec{x}_s|}}{4\pi|\vec{x}_m-\vec{x}_s|} \quad (6.9)$$

where $\vec{x}_m$ is the mirrored observer point, see Figure 6.3. The reflection coefficient r_H is 1 for an acoustically hard infinite plane and -1 for a fully absorbing (soft) infinite plane.

The formulation of the integral equation (6.7) is a so-called 'direct' formulation because the boundary variables (surface pressure and normal surface velocity) have a direct physical meaning. The formulation is valid only for a closed boundary surface and can therefore represent either an interior or an exterior pressure field, not a combination of both. In our investigations

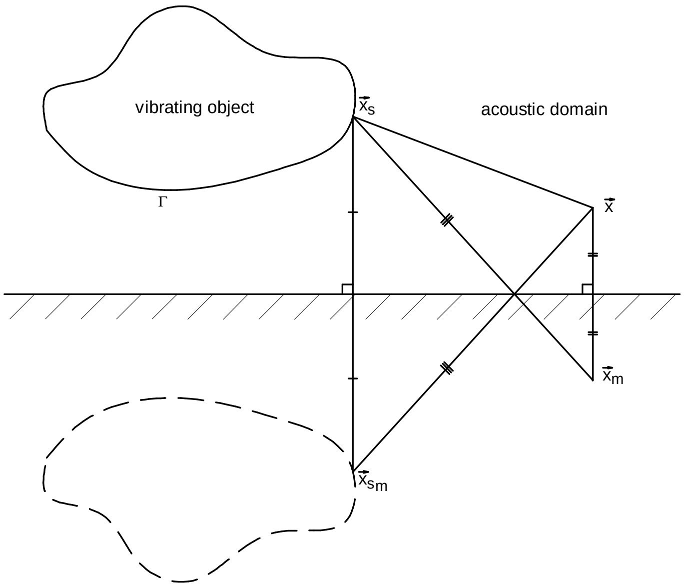

Figure 6.3: *Geometrical representation of the half-space formulation.*

only exterior problems are considered. For the sake of completeness, we note that an indirect boundary integral formulation also exists, which can be applied for combined interior/exterior acoustic problems. For more details reference is made to Fillippi (1977).

In BEM the weak formulation of the integral equation 6.7 is taken and multiplied by weighting functions. The surface of the vibrating structure is discretised into a number of elements. The nodal pressures and normal velocities are stored in vector form as $\{p\} = [p_1, p_2, ..., p_j, ...]^T$ and $\{v\} = [v_1, v_2, ..., v_j, ...]^T$, respectively. Next, the equations are discretised resulting in a set of linear equations in matrix form:

$$[A(\omega)]\{p\} = [B(\omega)]\{v\} \tag{6.10}$$

with frequency dependent system matrices $[A]$ and $[B]$. The nodal velocity amplitudes $\{v\}$ are obtained from a structural analysis or from measurements. By solving the set of equations, the surface pressures and the pressure at an arbitrary point in the acoustic domain can be determined via equation 6.7. Consequently, also the radiated sound power can be obtained. It is noted that for an efficient calculation of the matrices $[A]$ and $[B]$, a frequency interpolation technique is applied. For details about this technique the reader is referred to Benthien and Schenck (1991).

Radiated sound power

In the Boundary Element Method, the pressure and normal velocity for any point $\vec{x}_s$ on surface S are discretised:

$$p(\vec{x}_s) = \sum_j \phi_j(\vec{r}_s) p_j = \{\phi\}^T\{p\} \tag{6.11}$$

$$v_n(\vec{x}_s) = \sum_j \phi_j(\vec{r}_s) v_j = \{\phi\}^T\{v\} \tag{6.12}$$

with $\{\phi\} = [\phi_1, \phi_2, ..., \phi_j, ...]^T$ containing the basis functions that are used to discretise the pressure and velocity. Using equation 6.3 the discretised expression for the radiated sound power yields:

$$\bar{W} = \frac{1}{2} Re \int_S \{p\}^T\{\phi\}\{\phi\}^T\{v\}^* dS = \frac{1}{2} Re[\{p\}^T[N]\{v\}^*] \tag{6.13}$$

where the matrix $[N] = \{\phi\}\{\phi\}^T$. With the help of equation 6.10 this expression for the frequency dependent sound power can be rewritten as:

$$\bar{W}(\omega) = \frac{1}{2}\{v\}^T Re[([A]^{-1}[B])^T[N]]\{v\}^* = \frac{1}{2}\{v\}^T[C(\omega)]\{v\}^* \tag{6.14}$$

where the matrix $[C(\omega)]$ is called the power coupling matrix. This matrix is positive definite as the radiated power is always positive for any nonzero value of $\{v\}$.

6.2.2 Radiation modes formulation

The radiated sound power of a structure can efficiently be calculated with the radiation modes formulation, a relatively new concept in acoustics introduced by Borgiotti (1990) and applied in the field of acoustic design and optimization (Kuijpers, 1999; Kessels, 2000), acousto-elastic modelling (Basten, 2001; Cunefare and Currey, 1994) and active noise control (Elliott and Johnson, 1993).

The radiation modes formulation is a powerful reduction method based on the fact that the surface velocity of a structure can be decomposed into a

set of independently radiating components, the *radiation modes*. They form an orthogonal modal basis with respect to the total acoustic power. This in contrast with structural eigenmodes which are orthogonal with respect to the kinetic and elastic energy of the structure.
A main advantage of the radiation modes is that they are independent of the boundary conditions and the (structural) material properties, but only on the external geometry of the structure under consideration and on the frequency. This implies that the radiation modes can be reused for acoustic analyses as long as the geometry does not change. As a result, very efficient calculations of the radiated sound power can be performed.

The radiation modes concept is directly related to the radiation efficiency $\sigma(\omega)$. This quantity in acoustics indicates how well a vibrating object radiates sound. It is defined as the ratio between the power per unit area radiated by the source and the power radiated by a reference source. The reference source can be considered as a sphere vibrating uniformly over the surface with a mean square velocity $\langle \bar{v^2} \rangle$:

$$\sigma(\omega) = \frac{\bar{W}(\omega)/S}{\rho_0 c_0 \langle \bar{v^2} \rangle} \tag{6.15}$$

The mean square velocity $\langle \bar{v^2} \rangle$ can be written in discretised form as:

$$\langle \bar{v^2} \rangle = \frac{1}{S} \int\limits_S v_n^2(\vec{x}_s) dS = \frac{1}{S} \{v\}^H [N] \{v\} \tag{6.16}$$

Using the expression for the sound power 6.14 and the discretised mean square velocity, equation 6.16 is expressed in discrete form as:

$$\sigma(\omega) = \frac{1}{\rho_0 c_0} \frac{\{v\}^H [C(\omega)] \{v\}}{\{v\}^H [N] \{v\}} \tag{6.17}$$

where $\{v\}^H$ is the hermitian (complex conjugate transpose) of the normal velocity. This equation can be converted into the following generalised eigenvalue problem (Cunefare, 1991):

$$[C(\omega)]\{v\} = \lambda(\omega)[N]\{v\} \tag{6.18}$$

where $\lambda = \sigma \rho_0 c_0$. Solving the eigenvalue probem results in real eigenvalues λ_k and real eigenvectors $\{q_k\}$. The eigenvalues are a measure for the modal radiation efficiencies σ_k of the system:

$$\sigma_k(\omega) = \frac{\lambda_k(\omega)}{\rho_0 c_0} \tag{6.19}$$

The eigenvectors $\{q_k\}$ are stored columnwise in the matrix $[Q]$ and are associated with the radiation modes, which are normalised with respect to the matrix $[N]$, according to:

$$[Q]^H[N][Q] = [I] \tag{6.20}$$

$$[Q]^H[C][Q] = [\Lambda] \tag{6.21}$$

where $[Q] = [\{q_1\}, \{q_2\}, ..., \{q_k\}, ...]$, $[\Lambda]$ is a diagonal matrix containing the eigenvalues and $[I]$ is the identity matrix. Again, it is noted that the radiation modes only depend on the geometry of the vibrating structure and on the frequency, as the matrices $[C]$ and $[N]$ are only dependent on those properties.

The radiation modes can now be used to describe the velocity distribution of the surface:

$$\{v\} = \sum_k \{q_k\}\zeta_k = [Q]\{\zeta\} \tag{6.22}$$

where ζ_k are the modal contribution coefficients. Pre-multiplying this equation by $[Q]^H[N]$ and using the normalisation of equation 6.20, the modal contribution coefficients can be computed:

$$\{\zeta\} = [Q]^H[N]\{v\} \tag{6.23}$$

Substitution of 6.22 into 6.14 gives:

$$\bar{W}(\omega) = \frac{1}{2}\{v\}^T[C(\omega)]\{v\}^* = \frac{1}{2}\{\zeta\}^H[Q]^H[C(\omega)][Q]\{\zeta\} \tag{6.24}$$

which after using the normalisation in 6.21, leads to:

$$\bar{W}(\omega) = \frac{1}{2}\{\zeta\}^H[\Lambda(\omega)]\{\zeta\} \tag{6.25}$$

From this expression it can be learned that the radiated acoustic power can be calculated very efficiently, once the radiation modes are known. Obviously, the radiation modes can be reused as long as the geometry of the structure remains unchanged. This is important because in general the radiating surface of a bearing application does not change when a viscoelastic support is added in the vicinity of the bearings. Therefore, efficient numerical analyses can be performed for variable viscoelastic layer properties, such as the material type or the geometry of the layer.

6.2.3 Implementation

In general, the structural FEM models are rather complex. The models consist of several components, each having many elements on the surfaces. It is not practical to perform a full acoustic analysis for such refined models. Therefore, a relatively simple geometric model was built, representing the shape of the radiating surface. This 'acoustic' model was then meshed with boundary elements and was used for the acoustic analysis.

The velocity distribution of the radiating surface was extracted from the structural analysis or the vibration measurement and subsequently used as input data for the acoustic analysis. As the surface meshes of the structural model or the measurement grid and the acoustic model are different, the nodal 'structural' velocities were transformed to nodal 'acoustic' velocities (see the following section for details). The resulting output is the velocity distribution of the acoustic model for each specified frequency. These data in combination with the radiation modes were used to calculate the acoustic radiated power of the vibrating structure based on equations 6.23 and 6.25.

6.3 Acoustic modelling of the electric motor

For the acoustic analyses of the electric motor a simple BEM model was created, see Figure 6.4.

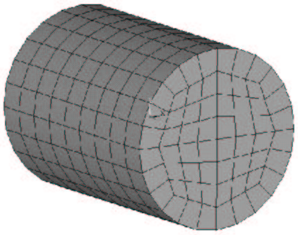

Figure 6.4: *Boundary element model of the electric motor.*

Due to the shielded rotor and the fixed foot, it is justified to assume that only the cylindrical outer casing and the cover shields radiate noise. Radiation of the foot and the rotor were not considered. Use was made of the half-space formulation with an infinite half-space located at 5 mm from the bottom of the structure.

For the sound power calculation the radiation modes formulation (Section 6.2.2) was adopted. For this purpose, the radiation modes and accompanying radiation efficiencies were calculated for the cylindrical BEM model. As an example, a number of characteristic radiation modes are presented in Figure 6.5 for frequencies of 1000, 1500 and 2500 Hz. The radiation modes are visualised in terms of a normal surface velocity distribution.

This figure shows that the radiation modes and the corresponding radiation efficiencies strongly depend on the frequency. In general, the radiation efficiency increases with the frequency. It is important to notice that the sound power level is determined both by the radiation efficiency and the modal contribution coefficient of the radiation modes that compose the velocity distribution of the vibrating structure. If the velocity distribution spatially matches an efficient radiation mode, high sound power levels can be expected. This appears to be the case for the measured vibration mode around 1500 Hz (Figure 5.9), which matches the second radiation mode at 1500 Hz. As will be discussed later on in section 6.4.3, high sound power levels were obtained at this specific frequency.

It is recalled here that the radiation modes only depend on the geometry of the structure and on the frequency. This has the advantage that the radiation modes only have to be calculated once as long as the geometry remains unchanged. This also applies to the electric motor because the viscoelastic bearing support does not change the geometry of the outer surface. As a result, the acoustic analysis can be performed in a very efficient way and is well-suited for parameter studies on the design of an effective viscoelastic bearing support. It should be noted that in such an analysis only the acoustic radiated power is calculated. In order to determine the sound pressure at an arbitrary point in the acoustic field, a fully computational analysis has to be performed for each design.

6.3.1 Hybrid acoustic modelling

In order to test the validity of the acoustic model, it has to be ensured that the structural velocities for the calculations are as accurate as possible. Therefore, first a hybrid acoustic modelling approach was used, in which measured velocity data are introduced as input. In this way, all possible errors due to inaccuracies of a structural model are circumvented.

1000 Hz

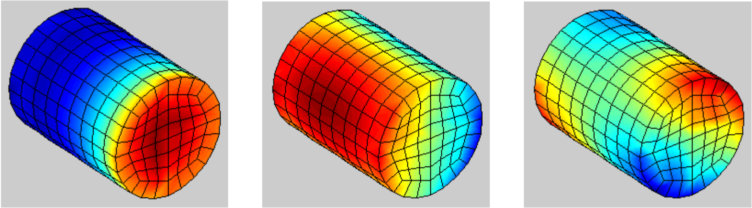

rad. efficiency 0.98 0.68 0.27

1500 Hz

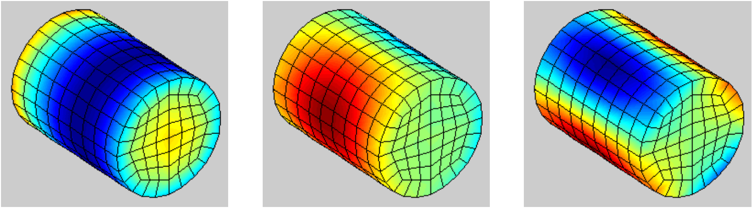

rad. efficiency 1.17 1.08 0.69

2500 Hz

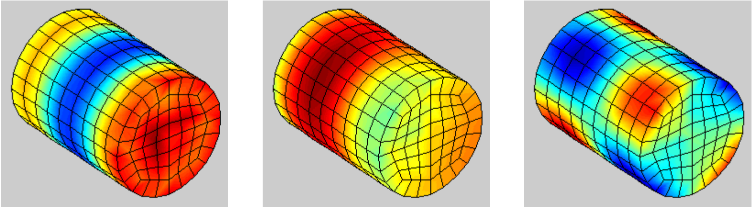

rad. efficiency 1.90 1.42 1.28

Figure 6.5: *Some characteristic radiation modes with accompanying radiation efficiencies of the BEM model at 1000, 1500 and 2500 Hz.*

For this purpose, a running mode analysis on the motor was carried out after which the cross-power spectra were determined between each point of the measurement grid and a reference point. In order to be able perform acoustic analyses in a reasonable time frame the frequency resolution was set to 25 Hz. The structural velocity of each gridpoint was calculated by:

$$v_i = \sqrt{2}\frac{XP_i}{2\pi f\sqrt{AP_{ref}}} \tag{6.26}$$

where v_i is the complex velocity, XP_i the cross-power spectrum between the acceleration at point i and the reference point, and AP_{ref} denotes the auto-power spectrum of the reference point. The reference point is located on the table in order to determine the (absolute) phase information of each gridpoint. To go from acceleration to velocity, XP_i is divided by $2\pi f$, where f is the frequency. As the spectra are measured as rms values, the factor $\sqrt{2}$ is introduced to obtain velocity amplitudes.

As the BEM model contains more nodes than the measurement grid, the measured velocity data must be projected onto the BEM model. For this purpose, linear interpolation between the gridpoints was applied. The velocity of each node of the BEM model was computed with the use of four closest measurement gridpoints. As a result, the normal velocity distribution over the BEM model surface was obtained. A typical example is shown in Figure 6.6 for a vibration mode at 642 Hz. The maximum normal velocity in this graph (indicated by the red color) is in the order of 10 $\mu m/s$.

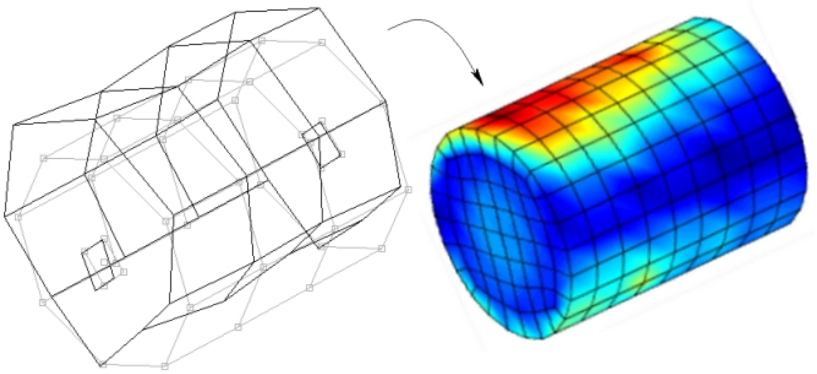

Figure 6.6: *Measured structural velocity projected on a BEM model for a vibration mode at 642 Hz.*

Finally, the acoustic radiated power and other acoustic quantities were calculated as a function of frequency.

6.3.2 Fully numerical acoustic modelling

In the fully numerical approach, a harmonic response analysis was performed to simulate the dynamic behaviour of the running electric motor. As a result, the structural velocities were found in each finite element node of the surfaces of the components. Similar to the hybrid modelling approach, the velocity data were projected on a simple BEM model. In this case, however, the value of the velocity of the closest finite element node is used for each node of the boundary element mesh. This results in a sufficiently accurate velocity distribution as the finite element model contains about 100 times more surface nodes than the measurement grid.

6.4 Measured acoustic behaviour of the electric motor

6.4.1 Approach

In the present investigations, sound intensity measurements were performed to analyse the acoustic behaviour of the running electric motor. The acoustic power radiated by a vibrating object can easily be determined with the help of acoustic intensity measurements. For this purpose, one has to define a virtual surface enclosing the source. The sound intensity is then measured by scanning the surface with a sound intensity probe, according to international standards (ISO 9614-2). The sound power radiated through the global surface equals the product of the average normal intensity and the surface area.

The acoustic intensity measurement is based on the pressure gradient method. The pressure gradient over a specific distance between two points in a sound field is directly related to the particle velocity. By using two closely spaced microphones (Figure 6.7) both the pressure gradient and the pressure in the middle point can be determined, so the acoustic intensity can be determined as well.

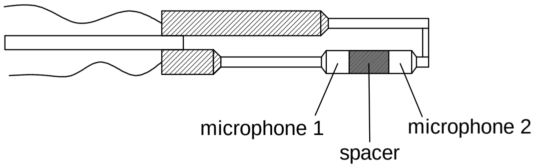

Figure 6.7: *Sound intensity probe.*

For the measurements performed in this study, the accuracy in the radiated sound power is estimated at 1.5 dB.

For details about the limitations and errors in sound intensity measurements, the reader is referred to Sas (2001).

6.4.2 Experimental setup

Before the actual measurements can take place, a number of boundary conditions need to be ensured for the electric motor. Normally, under operating conditions the motor is mounted on a rigid surface. Therefore in this study the motor was mounted on a table with such a high mass that vibrations of the table are negligible. Moreover, to further avoid any contribution of the table a plate with a smooth (acoustically hard) surface was placed around the motor (see Figure 6.8). The plate was structurally decoupled from the table by using thick pieces of foam and a small air gap, as is sketched in Figure 6.9.

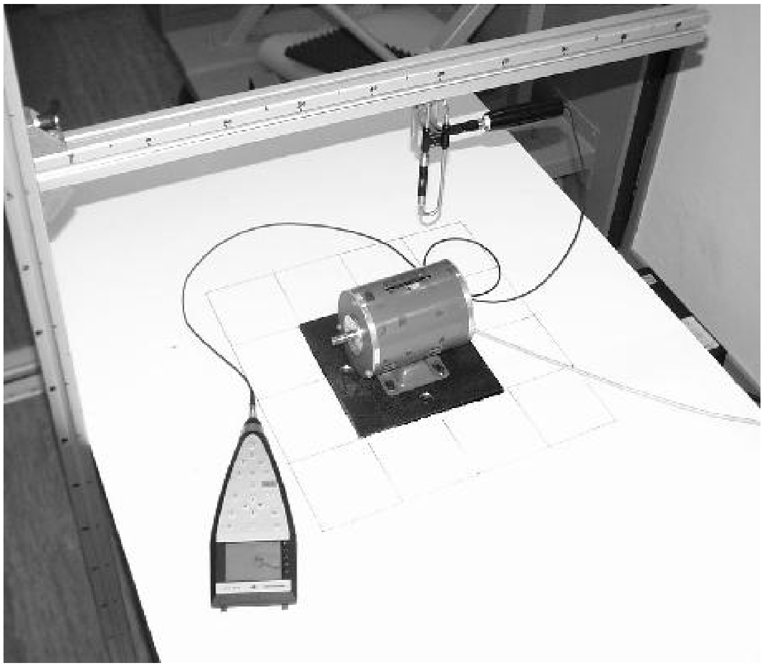

Figure 6.8: *Setup for acoustic intensity measurements of the electric motor.*

In this way the system can be considered as a structure vibrating in a half-space. The half-space boundary (plate) is considered acoustically hard, i.e. all incoming sound is fully reflected into space. The dimensions of

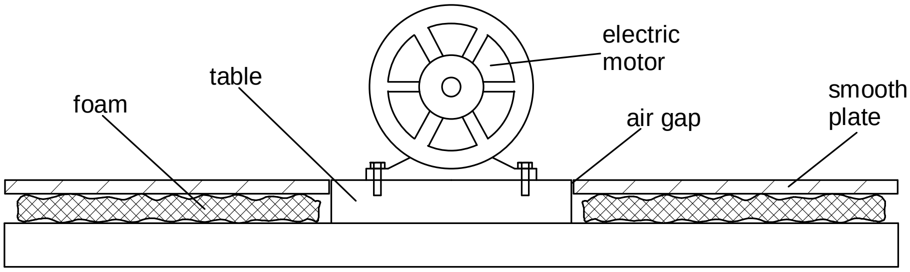

Figure 6.9: *Cross-section of the test setup with a smooth plate decoupled from the electric motor.*

the plate were 100 by 150 cm, thus accurate analyses could be performed from about 500 Hz. For lower frequencies the acoustic wavelengths are too large with respect to the table dimensions, meaning that the half-space assumption is violated.

For the sound intensity measurements a B&K sound intensity probe type 3595 was used in combination with a sound analyser type B&K 2260. The sound pressure time signals of both microphones were measured and exported to the National Instruments data acquisition card (type AT-A2150). The data were processed in combination with the LabView software. From the cross-power spectrum $XP_{p_1p_2}$ between pressure 1 and pressure 2 (see Figure 6.7) the time averaged sound intensity was computed from the expression:

$$\bar{I} = -\frac{Im(XP_{p_1p_2})}{\rho_0\omega\Delta r} \tag{6.27}$$

where Δr is the spacer length, which is equal to the distance between the two microphones.
Next, the radiated sound power was calculated by multiplication of the time and spatially averaged sound intensity $\bar{I}_{av}$ with the scanned surface area S:

$$\bar{W} = \bar{I}_{av} \cdot S \tag{6.28}$$

The above mentioned scanning method was applied on a surface with dimensions 50x50x30 cm, enclosing the motor at a distance of 15 cm from the surface. Each surface of the box was scanned hand held during 12 seconds with the intensity probe. In order to ensure the measurement quality, different spacer configurations can be used for different frequency ranges . For the present analyses, however, it was found sufficient to use a 12 mm spacer only.

6.4.3 Experimental results

In Figure 6.10a the measured sound power level of a running electric motor with dummy rings is shown as a function of frequency. An A-weighting function (see Figure 6.2) is applied to obtain the sound power level in dB(A). The averaged A-weighted surface velocity level of the electric motor is shown in Figure 6.10b. A reference velocity level $v_{ref} = 1.85 \cdot 10^{-7}$ is chosen to make the velocity level comparable to the sound power level (see equations 4.1 and 4.2).

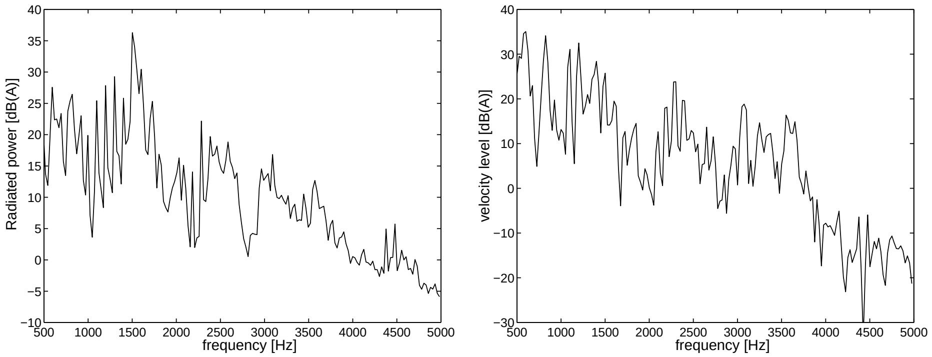

(a) *(b)*

Figure 6.10: *(a) Measured sound power level and (b) velocity level of the electric motor.*

It can be observed that the highest (A-weighted) sound power levels occur in the frequency range from 500 to 1600 Hz with a clear peak at about 1500 Hz. This does not hold for the velocity level, for which several peaks with similar level appear up to 1500 Hz. In general, the trend of the average velocity level differs to some extent from that of the sound power level. This confirms the need to analyse not only the structural vibration behaviour but also the acoustic behaviour of the electric motor.

Most probably the sound level peak at 1500 Hz corresponds with the vibration mode measured at 1544 Hz (see Figure 5.9). This vibration mode shows large flexible deformations of the housing, mainly in the radial direction.

6.5 Validation of the acoustic models

6.5.1 Validation of the hybrid acoustic model

As mentioned earlier the distribution of the surface velocities, measured during a running mode analysis, was used as input for the acoustic computation. The acoustic radiated power was determined as a function of frequency, both experimentally and numerically. The results are shown in Figure 6.11 for the frequency range between 500 and 5000 Hz. For lower frequencies the accuracy is low as a result of the half-space assumption. For frequencies above 2.5 kHz the acoustic radiated power appeared to decrease considerably.

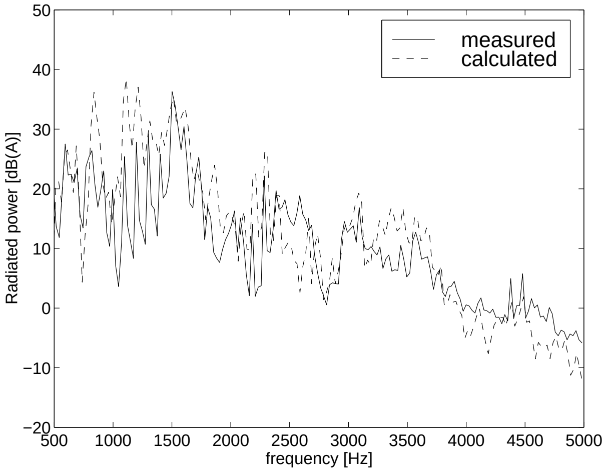

Figure 6.11: *Total measured and calculated radiated acoustic power of the electric motor.*

In general, Figure 6.11 reveals a reasonably good agreement between the calculated and measured acoustic powers. For some frequencies, however, the spectra show a difference in the sound power of nearly 10 dB(A). Some of the deviations might be caused by the presence of some holes on both sides of the motor, as can be observed in Figure 5.1. Clearly, the effect of these holes is not accounted for in the BEM model, just as the radiation of the foot.

More importantly is that deviations probably result from the limited number of sensors used for the vibration measurement. An increase of the number of sensors results in a more accurate velocity distribution over the surface, which may result in a better sound power prediction.

Possible errors due to the BEM modelling procedure, such as errors from the model geometry, the number of elements, the element type and the velocity projection method have been investigated. However, it was found that none of these aspects causes significant differences. As an example, the radiated sound power was calculated with two other BEM models, which are illustrated in Figure 6.12. For one model the boundary element mesh was refined, whereas for the other BEM model a small recess was modelled at both ends of the cylinder to describe the geometry of the shields more accurately. The results, as given in Figure 6.13, show an excellent agreement.

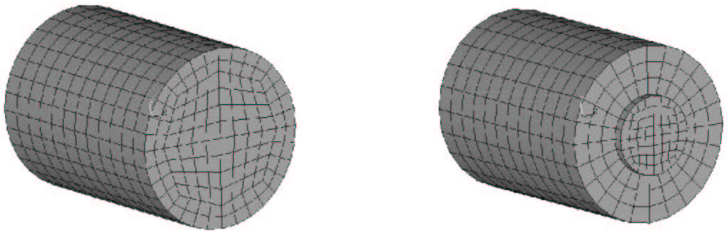

Figure 6.12: *BEM model with mesh refinement (left) and with an alternative geometry (right).*

It could not be excluded that during the sound measurements background noise, reflection, absorption, a non-constant motor noise and the (manual) scanning method result in possible errors in the sound power values. To check this the sound measurement was repeated several times. A satisfactory repeatibility was found, the uncertainty between different measurements stayed within 3 dB(A).

The conclusion is that even with a very simple BEM model the radiated acoustic power of a (complex) running electric motor can be predicted in a satisfactory way.

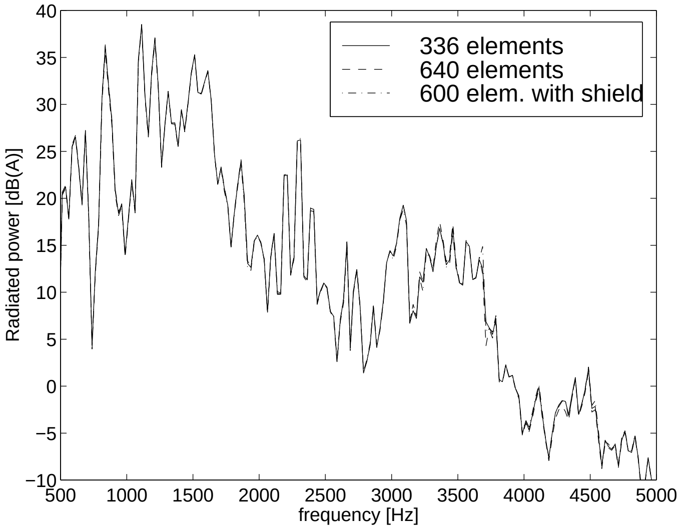

Figure 6.13: *Calculated acoustic power of the electric motor using three different BEM models.*

6.5.2 Validation of the fully numerical acoustic model

The fully numerical acoustic model concerns the BEM model in combination with the numerically predicted structural velocities on the outer surface of the motor. For this purpose, a harmonic response analysis was performed in the way as discussed in Section 5.4.2. In Figure 6.14 the sound power levels obtained with a hybrid analysis are compared with the fully numerical prediction.

With the exception of some large deviations in the frequency range above 2.5 kHz, a reasonable agreement was obtained between the hybrid model and the fully numerical model. For the frequencies around 3200 Hz the fully numerical model overestimates the acoustic power significantly. This is the result of inaccurately predicted velocity data of the motor surface, such as was observed in Figure 5.21a. Generally, the trends in the sound power curve are fairly well predicted, specifically in the frequency range from 1000 to 2500 Hz. This is important because the highest sound power levels were measured in this frequency range. This allows us to use the model for design purposes.

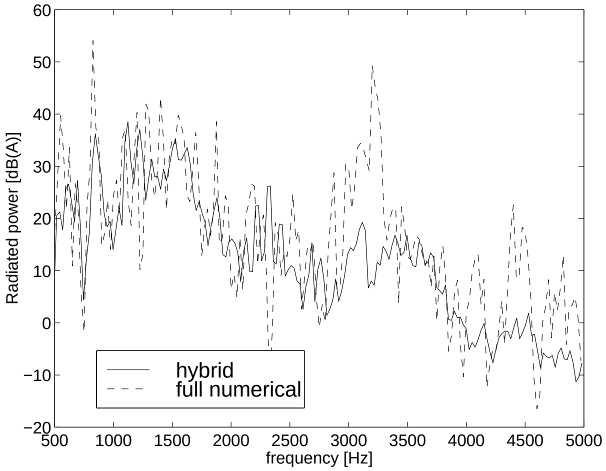

Figure 6.14: *Radiated acoustic power of the electric motor calculated with a hybrid analysis and a fully numerical approach.*

6.6 Experimental results of the electric motor with viscoelastic bearing supports

The acoustic behaviour of the electric motor was also investigated for different viscoelastic bearing supports. In Figure 6.15 the experimental results are shown.

From this figure similar trends can be observed as in the results of the running mode analyses from the previous chapter (see Figures 5.20 and 5.21). Clearly, the radiated noise is reduced with the PMC 121/50 1.5 mm support. For the Vamac 5022 1.5 mm support the sound reduction is less effective. These trends are directly related to the excitation forces in the systems (Figure 5.20). The sound power reduction by the PMC 121/50 support appears to be significant in the high frequency range, i.e. above 1500 Hz. In fact, the reduction is 5.1 dB for the rms sound power level. This result shows that by applying an accurately manufactured viscoelastic bearing support the noise level of a rotor dynamics application can be improved.

6.7 Conclusions

From the results of the experimental and numerical studies on the noise emitted by an electric motor several conclusions can be drawn:

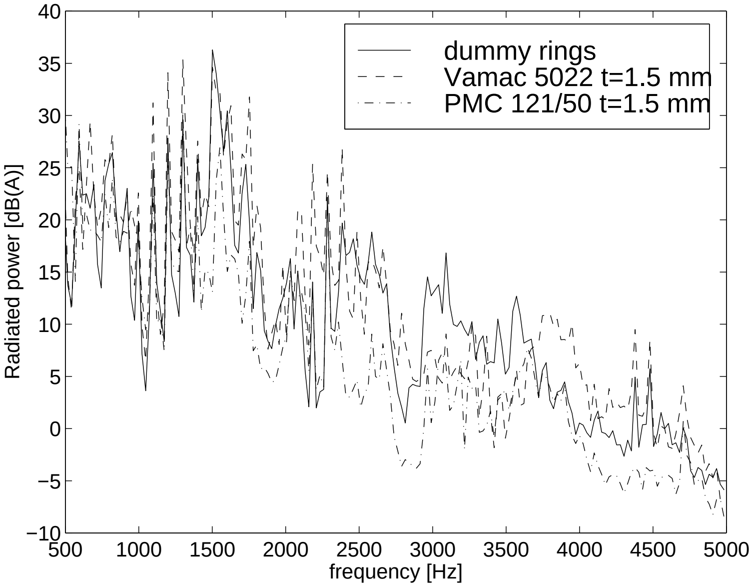

Figure 6.15: *Measured radiated acoustic power of the electric motor with different bearing supports.*

Based on the radiation modes formulation an efficient method is obtained to predict the radiated sound power of a vibrating structure. The main advantage is that the radiation modes can be reused as long as the geometry of the surface of the structure does not change. This is especially of importance in the design process for a viscoelastic bearing support because changing this part does not alter the radiating surface of the application.

The sound intensity measurements on the running electric motor showed that the highest sound level occurs around 1500 Hz. As the sound power as a function of the frequency differs in essence from the vibration level it can be concluded that an acoustic analysis is essential for a good understanding of the acoustic behaviour of the electric motor.

The broadband noise of a running electric motor can be predicted quite accurately with a simple BEM model when use is made of measured surface velocity data.
The use of numerically simulated surface velocities led to less accurate

results for the radiated power in the high frequency range. However, the general trends in noise levels are well predicted in the dominant frequency range, i.e. from 1000 to 2500 Hz. Therefore, the fully numerical approach, based on the radiation modes technique, is still sufficiently accurate for design studies on a viscoelastic bearing support.

The sound power level of the electric motor was reduced by 5.1 dB by application of a PMC 121/50 1.5 mm bearing support. This was mainly the result of decreased excitation forces.

Chapter 7

Design strategy for a viscoelastic bearing support

7.1 Introduction

7.1.1 Preceding considerations

A significant improvement of the noise and vibration characteristics was demonstrated in the dynamic and acoustic experiments on the VICTORIA test rig and the electric motor by the application of viscoelastic bearing supports. In the case of the electric motor, however, the improvement was not only a result of vibration damping or isolation but mainly the result of a decrease in excitation forces. It appeared that the excitation forces in the electric motor strongly depend on the bearing support. This aspect is, however, very difficult to predict.

The numerical simulation of the vibrational behaviour of the structure was quite succesful for the VICTORIA test rig.
However, the results for the electric motor were less satisfactory. Especially for the simulation of the running motor, it was only the trends in the dynamic response that were reasonably well predicted. This made it difficult to make accurate predictions of the radiated sound on the basis of a fully numerical simulation. One must be aware, though, that the electric motor is a much more complex system than the VICTORIA test rig.

Nevertheless, by using the structural model in combination with a simple BEM model some important trends in the radiated sound power (see Figure

6.14) were predicted in a satisfactory way. This holds especially for the frequency range from 1000 to 2500 Hz, for which the highest sound power levels were measured (Figure 6.11). This confirms the value of predictive models for acoustic design studies, albeit that one must be aware of the limitations of such an approach. In that respect, a hybrid modelling approach gives more accurate predictions of the sound power level. The disadvantage of such an approach, however, is the necessity of performing costly and time consuming measurements and prototyping.

7.1.2 Outline

An attempt is made to present some guidelines for the design of viscoelastic bearing supports. Probably, these guidelines are also useful for engineers dealing with other methods of reducing the noise produced in rolling bearing applications. First, some basic design rules are presented. Next, a more quantitative method for design improvement is formulated. The latter method was applied on the VICTORIA test rig for which the vibration behaviour is analysed. In addition, a parameter study is performed on the electric motor with the aim to improve its acoustic behaviour.

7.2 Basic design rules

As a first step, some basic design rules for the implementation of a viscoelastic bearing support are proposed. They serve as a basis for a more thorough design procedure, which is discussed later. The rules presented here are based on the experience gathered in this study, but are by no means exhaustive.

- Firstly and most important, the design of a viscoelastic bearing support is very much dependent on the **application**. Basically, this implies that for each application the structural and acoustic behaviour must be well understood. For a systematic approach to an engineering noise problem this means: identification of (1) the noise source mechanisms, (2) the sound paths and (3) the components radiating the noise.

- Viscoelastic **damping** only becomes effective when the viscoelastic material is subjected to **shear** deformation. This has consequences for the precise shape of the viscoelastic layers. In Figure 7.1 some geometries are presented which are suitable for axial, tilting and radial motions of the bearing, respectively.

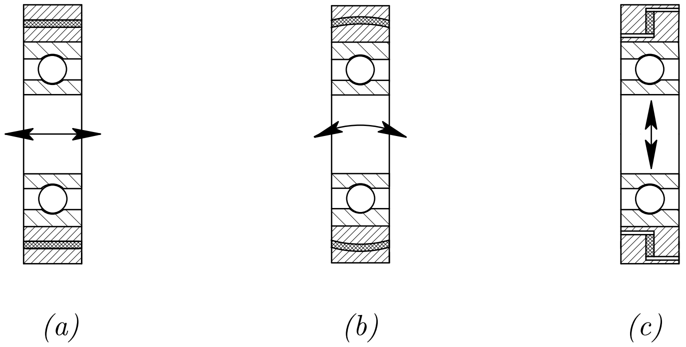

Figure 7.1: *(a) Cylindrical, (b) spherical and (c) radial viscoelastic layers suited for the damping of axial, tilting and radial vibrations of the bearing, respectively.*

- Vibration **isolation** is most effective when a high stiffness of the bearing support is avoided. A high stiffness can result from the high bulk modulus of viscoelastic materials. Viscoelastic support designs such as shown in Figure 7.2 should therefore not be applied because the stiffness is very high both in the axial, tilt and radial directions.

Figure 7.2: *Some badly designed viscoelastic layer configurations.*

For an effective vibration isolation the support stiffness must be chosen as low as possible, though sufficient to provide the static support.

- Vibration isolation can be achieved when the bearing application is excited mainly by the bearing-shaft arrangement, e.g. due to a shaft imbalance or gear meshing.

- The creation of vibration damping is required when the sound radiating component is directly excited, e.g. the housing in an electric motor which is excited by electromagnetic forces.
- The choice of **viscoelastic material** depends on the mechanical, thermal and chemical properties. Moreover, costs can be a decisive parameter. Regarding mechanical properties, damping of a viscoelastic material is directly related to the frequency dependent stiffness, i.e. the shear modulus. A material for which the shear modulus strongly increases with the frequency (e.g. Vamac (AEM), EPDM or some polyurethane rubbers), shows a high loss factor and can thus be used for vibration damping. The high stiffness at high frequencies, however, limits the usage of these materials for vibration isolation purposes. In that case low damping materials corresponding with low frequency dependence of the stiffness should be applied. Natural Rubber (NR), for example, is a material that satisfies these demands.

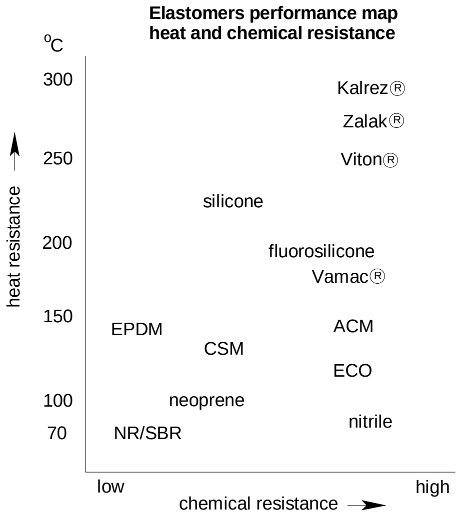

Figure 7.3: *Heat and chemical resistance map of various rubbers.*

The environment in which a viscoelastic bearing support is applied is also important for the material choice. Temperature and chemical (or oil) resistance are decisive. In Figure 7.3 an overview of the heat and chemical resistance for a variety of rubbers is shown.

In general, the cost of a material is directly related to the heat and

chemical resistance.
Finally, viscoelastic materials are subjected to material ageing phenomena, i.e. material properties change in the long term. As a result, the viscoelastic bearing support has a specific duration of life. It is known that natural rubber (NR) has good life characteristics.

- The **geometrical design** of the viscoelastic support must be chosen such that the required stiffness is obtained in the axial, tilt and radial directions. For this purpose the thickness, the radius, the width and the conical angles of a viscoelastic layer can be varied, see Figure 7.4.

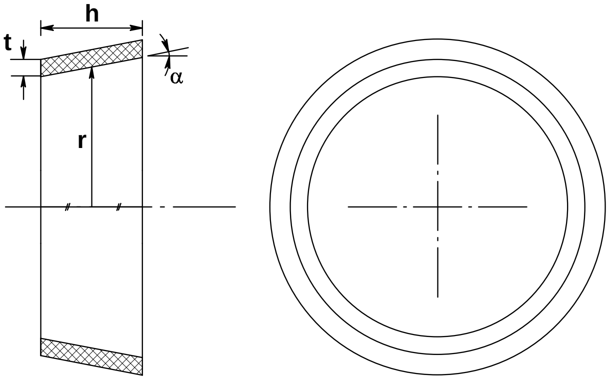

Figure 7.4: *Design parameters of a viscoelastic layer.*

The effects of thickness, radius, width or angle variations on the normalised (static) stiffnesses are shown in Figure 7.5. The values of the stiffnesses are normalised to the corresponding stiffnesses of a standard configuration with $r = 17.5$ mm, $h = 11$ mm, $t = 1.5$ mm, $\alpha = 0^o$ and the material properties of Vamac 5022 are used. The radial (k_{rad}), axial (k_{ax}) and tilt stiffness (k_{til}) values were obtained from the (reduced) stiffness matrix of the CMS model of the layer (expression 7.1). Note that in the case of a nonzero angle α a coupling stiffness term k_{cou} also appears in the matrix. It was found, however, that this term is of minor importance for the dynamic behaviour of the bearing support. Also, the torsional stiffness k_{tor} is not varied in the present analyses, because it had very little effect on the overall dynamic response.

$$[k_{ve}] = \begin{bmatrix} k_{rad} & 0 & 0 & 0 & k_{cou} & 0 \\ 0 & k_{rad} & 0 & -k_{cou} & 0 & 0 \\ 0 & 0 & k_{ax} & 0 & 0 & 0 \\ 0 & -k_{cou} & 0 & k_{til} & 0 & 0 \\ k_{cou} & 0 & 0 & 0 & k_{til} & 0 \\ 0 & 0 & 0 & 0 & 0 & k_{tor} \end{bmatrix} \tag{7.1}$$

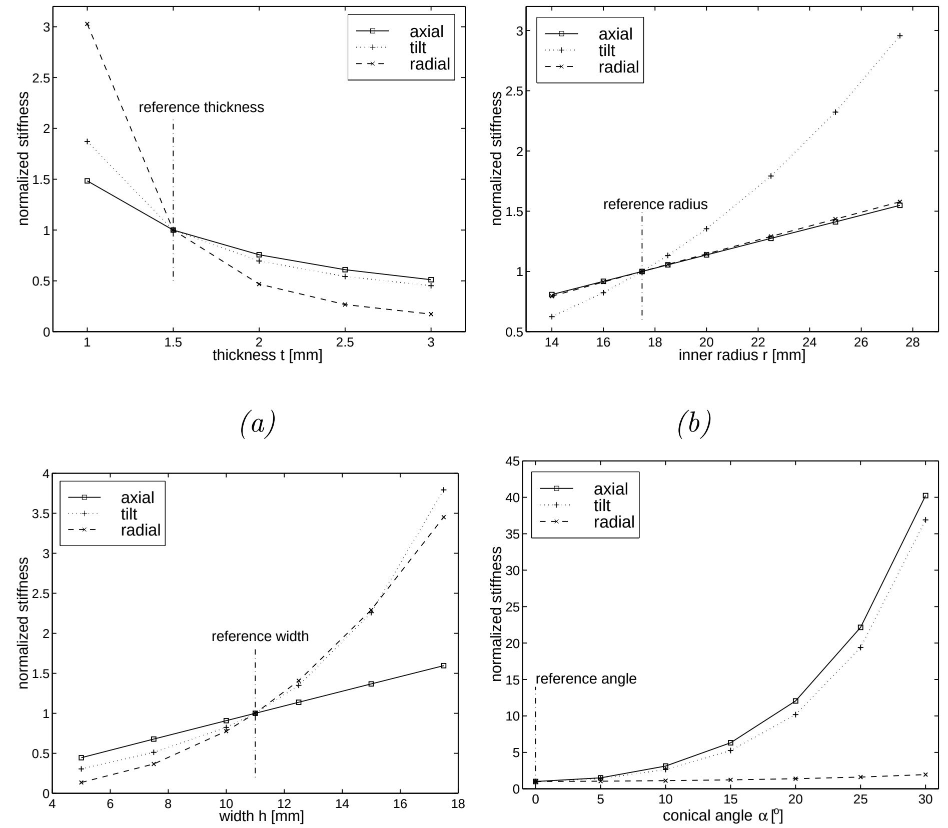

(a) (b)

(c) (d)

Figure 7.5: *Normalised stiffness of the viscoelastic layer as a function of the (a) thickness, (b) radius, (c) width and (d) conical angle.*

The results indicate that a change in thickness mainly influences the radial stiffness. A change in radius will mostly affect the tilt stiffness, whereas the layer width determines both the radial and tilt stiffnesses.

An increase of the conical angle hardly influences the radial stiffness, but the axial and tilt stiffnesses change considerably. From these observations it can be concluded that the stiffness in each individual direction can easily be altered.

The stiffness of the support can also be reduced by applying patches of material around the circumference, in a way as sketched in Figure 7.6.

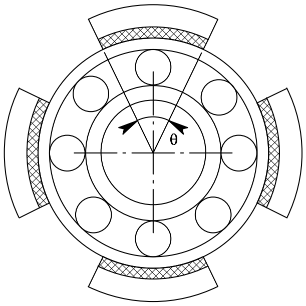

Figure 7.6: *Patches of viscoelastic material along the circumference.*

- The design of the support also depends on the **bearing properties** and the **bearing type**. The relative flexibility of the bearing support determines the efficiency of vibration isolation of the application. This means that for a clear isolation effect the bearing support needs to be more flexible than the bearing itself. In the case of a deep groove ball bearing (DGBB), for example, the axial and tilt stiffnesses of the support need to be low, as a DGBB itself is relatively flexible in these directions. A taper roller bearing (TRB), however, is much stiffer in the axial and tilt directions implying that the viscoelastic layer could be less flexible.

7.3 Design approach

The presented design rules concern a number of qualitative aspects. This knowledge will be useful when thinking about the shape the viscoelastic support could take and which material could be used. The effectiveness of the bearing support, however, needs to be maximised in a more quantitative way, i.e. by making use of numerical modelling techniques. For this purpose the structural and acoustic model of the bearing application can be of great help, because the reduced models result in short calculation times. This is ideal for design optimisation studies.

To finalise this study, an attempt is made to define a specific design criterion for the bearing application based on a number of design parameters for a viscoelastic support. In addition, a set of constraints needs to be fulfilled.

Design criterion

The aim of these investigations is to reduce radiated noise. Therefore, the root mean square (rms) sound power level has to be minimised. To account for the perceptibility of the human ear, an A-weighting function is applied:

minimise $L_{WA,rms}$ = A-weighted rms sound power level in dB(A)

$L_{WA,rms}$ is defined as:

$$L_{WA,rms} = 10 \log \left(\frac{W_{A,rms}}{10^{-12}} \right) \tag{7.2}$$

where $W_{A,rms}$ is the rms sound power over the complete frequency range, ω_1 to ω_{N_f} in a total of N_f steps:

$$W_{A,rms} = \sqrt{\sum_{j=1}^{N_f} 0.5 W_A(\omega_j)^2} \tag{7.3}$$

In the case of a structural design, such as for the VICTORIA test rig, the vibration level has to be minimised. The (spatially averaged) mean square velocity amplitude of the vibrating surface is selected as a measure for the overall vibration level:

$$\langle \bar{v^2} \rangle = \frac{1}{N} \sum_{i=1}^{N} \bar{v_i}^2 \tag{7.4}$$

where $\bar{v_i}$ is the time averaged velocity amplitude at location i and N is the total number of locations across the surface. The velocity level L_v is then expressed as:

$$L_v = 10 \log \left(\frac{\langle \bar{v^2} \rangle}{v_{ref}^2} \right) \tag{7.5}$$

where v_{ref} denotes the reference velocity level, see section 4.5.1. Again, an rms summation can be made over the frequency range to obtain the rms velocity level $L_{v,rms}$.

Design variables

In the present analyses no redesign of the structural components of the system will take place, except for the viscoelastic bearing support. As a consequence, the design variables are limited to the geometrical configuration, orientation and material characteristics of the viscoelastic layer. In fact, the most important design variables have already been shown in Figure 7.4.

When considering this configuration in combination with circumferential material patches (Figure 7.6) the number of variables is extended with a patch angle θ and a number of patches N_p. The material characteristics can be represented by a bulk modulus K and a complex dynamic shear modulus $G^*(\omega)$. As a result, the array with geometrical design variables x_g is given as:

$$x_g = [t, r, h, \alpha, \theta, N_p, K, G^*(\omega)]$$

It was found from the results presented in Figure 7.5 that these variables do not independently influence the axial, tilt and radial stiffnesses. In fact, many geometrical designs may be possible for a specific layer stiffness. Therefore, in the present approach we tried to find an optimal set for the axial (k_{ax}), tilt (k_{til}) and radial (k_{rad}) components of the stiffness matrix of the viscoelastic support. To account for the viscoelastic material behaviour, a distinction is made between the volumetric or bulk term and the deviatoric term of the stiffness:

$$k_{ax} = k_{ax,bulk} \cdot K + k_{ax,dev} \cdot G^*(\omega) \tag{7.6}$$

$$k_{til} = k_{til,bulk} \cdot K + k_{til,dev} \cdot G^*(\omega) \tag{7.7}$$

$$k_{rad} = k_{rad,bulk} \cdot K + k_{rad,dev} \cdot G^*(\omega) \tag{7.8}$$

As a result, the new array of design variables x_m becomes:

$$x_m = [k_{ax,bulk}, k_{ax,dev}, k_{til,bulk}, k_{til,dev}, k_{rad,bulk}, k_{rad,dev}, K, G^*(\omega)]$$

When an optimal set for these stiffness parameters has been determined, a suitable matching geometry has to be found. This can be achieved by using the relations between the geometrical parameters and the stiffnesses shown in Figure 7.5.

Design constraints

Generally, for rotating machinery the following set of constraints is of importance in the design process of a viscoelastic bearing support:

- The *static support stiffness* of the structure has to satisfy certain criteria. Therefore, it is necessary to analyse the effects of a flexible bearing support under static loading conditions caused by weight and preload. It is assumed that the (static) displacement of the bearing outer ring must not exceed the mounting tolerance between the bearing outer ring and the housing (ref. SKF catalogue (2002)).

- A certain *running accuracy* of the shaft or rotor must be fulfilled. This is affected both by the flexibility and by the geometrical accuracy of the viscoelastic bearing support.

- Obviously, there will be *geometrical constraints* for the layer design. In most applications there is only a limited space available for implementation of the viscoelastic support. Generally, the radius of the layer is determined by the bearing size, whereas for the thickness, width and conical angles of the configuration limited variations can be applied. There is no geometrical constraint on the patch angle.

- *Temperature* is an important contraint as it determines the material damping and stiffness characteristics. Moreover, the use of viscoelastic materials is restricted up to a certain maximum temperature, see Figure 7.3.

- In certain applications, e.g. gear boxes, oil resistance is of importance. In such a case, the viscoelastic layer must have a good *chemical resistivity*. This might also limit the choice of materials (Figure 7.3).

- Viscoelastic materials will *creep* under constant loading. Clearly, creep must be prevented whenever possible because it will influence the running conditions in rotating machinery. In the case of large static loading conditions, (vulcanised) rubbers should be used as they exhibit only marginal creep effects.

- The *life time* that the viscoelastic support must fulfill is a constraint and might limit the choice of materials.

Design tool

The numerical models describing the vibrational and acoustic behaviour of a bearing application are used to perform the design studies with respect to an optimum noise performance. A harmonic analysis was performed to simulate the dynamic behaviour of the system in running conditions. The resulting structural velocity data were used to compute the radiated sound power of the acoustic model (see also Section 6.2.3). A computationally efficient parameter study using the radiation modes technique was performed with respect to various stiffness parameters of the viscoelastic support. In Figure 7.7 a block diagram of such a parameter study is presented. Note that two loops are present in this diagram, one for the stiffness parameter and one for the frequency range.

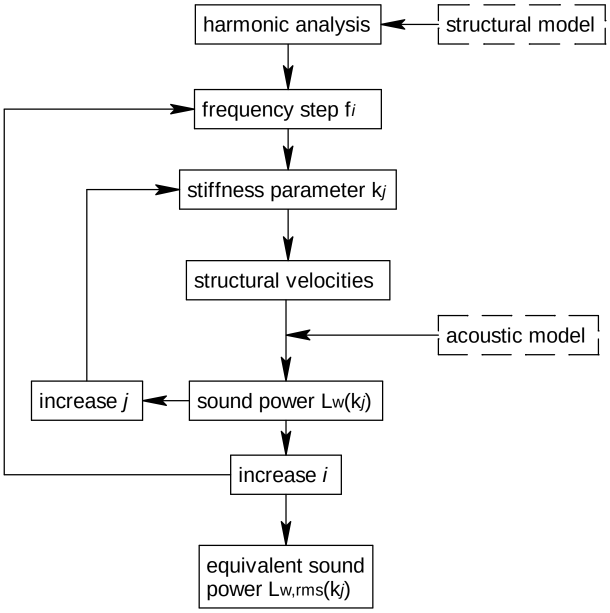

Figure 7.7: *Block diagram of a stiffness parameter study in acoustic analyses.*

The presented approach is applied in Section 7.5 for an acoustic design study of the electric motor. First, some design variations are applied on the VICTORIA test rig to improve its structural dynamic behaviour.

7.4 Design of a viscoelastic bearing support for the VICTORIA test rig

The numerical model was used to design an effective viscoelastic bearing support to reduce the structural vibration level of the test rig. A harmonic response analysis was performed to simulate the dynamic behaviour of the rotating test rig. Such an analysis is not a perfect simulation of the transient dynamics during operating conditions but it gives a good indication of the general dynamic behaviour.

In the analyses a unit radial force was applied in the middle of the shaft representing the imbalance force in practical running conditions. Vibration isolation of the test rig was studied for various viscoelastic support designs. For this purpose, the stiffness and damping characteristics of the support were varied through the usage of different materials and geometrical layer configurations.
In Figure 7.8 the velocity level of the housing is shown as a function of frequency for three different types of viscoelastic material. In this analysis the geometry of the layers is cylindrical (Figure 7.1a) with a thickness of 1.5 mm. Note that the rms velocity level $L_{v,rms}$ is given in the legend.

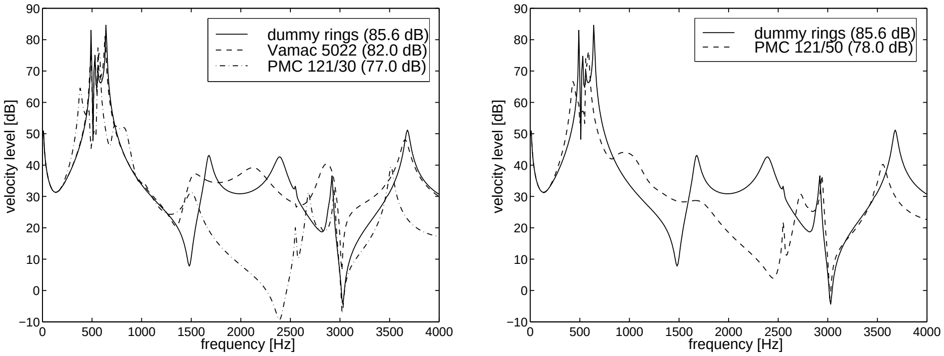

(a) *(b)*

Figure 7.8: *Velocity level as a function of frequency for the test rig with (a) Vamac 5022 and PMC 121/30 layers and (b) PMC 121/50 layers.*

Clearly, the effect of vibration isolation increases for softer support materials, such as PMC 121/30. Vamac 5022 on the other hand is a material with a high stiffness and favourable damping characteristics. This results in a poor vibration isolation but a rather good vibration damping effect.

Both effects are more or less achieved by the PMC 121/50 material, as illustrated in Figure 7.8b.

Apart from different materials, also the effect of the geometry of the viscoelastic layer was studied. For this purpose the cylindrical, spherical and radial layer configurations were considered (Figure 7.1). It was supposed that these layers be particularly effective for the isolation of axial, tilting and radial vibrations of the bearing, respectively.
The vibration level of the VICTORIA housing with the mentioned supports is shown in Figure 7.9.

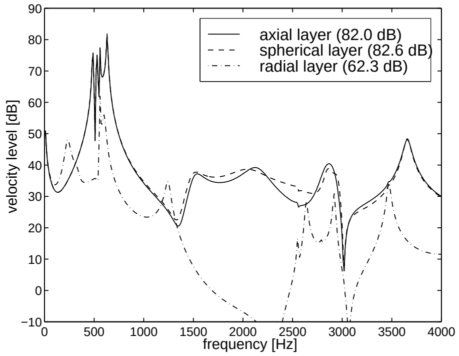

Figure 7.9: *Velocity level as a function of frequency for the test rig housing with Vamac 5022 cylindrical, spherical and radial viscoelastic layers.*

A spherical layer design hardly influences the dynamic behaviour of the system at all. Apparently, the stiffness of this design does not differ much from the stiffness of the cylindrical layer. The radial layer design, however, is much softer in the radial direction and therefore shows a very effective vibration isolation. The rms velocity level of the housing was reduced by about 20 dB in comparison with the other two designs.

Besides the dynamic behaviour of the test rig, also the static behaviour of the application is affected by the presence of a viscoelastic bearing support. In Figure 7.10a the static radial stiffness of the support is given for different designs. For this purpose, a static analysis was performed with a force acting on the shaft in the vertical direction. The displacement of the outer ring of the bearing was calculated such that the radial stiffness of the support can be derived. The stiffness limit is based on a gravitational force of 10 N per bearing, because the shaft has a mass of about 2 kg. It was assumed that the displacement of the outer ring must not exceed 10 μm, which is of the order of the mounting tolerance between the bearing outer ring and the housing. Therefore, the required radial stiffness must be at least 10^6 N/m. In addition, in Figure 7.10b the rms velocity level of both housings of the test rig are shown for the different layer designs.

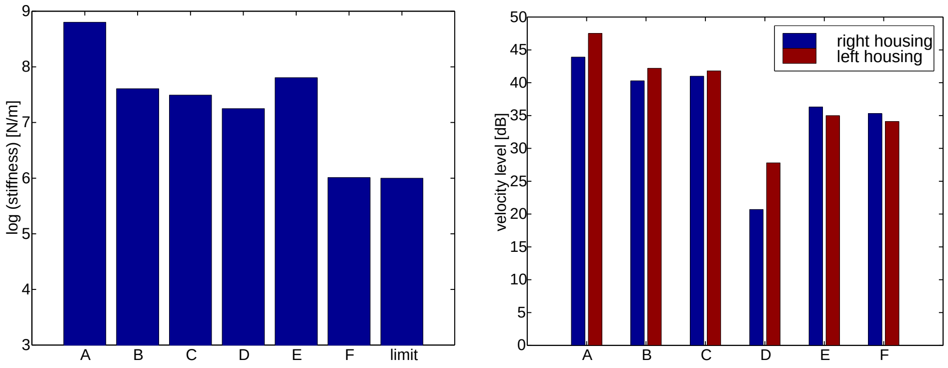

(a) *(b)*

Figure 7.10: *(a) Static radial stiffness and (b) total velocity level for the test rig with (A) dummy rings, (B) Vamac 5022 1.5 mm cylindrical layers, (C) PMC 121/50 1.5 mm layers, (D) PMC 121/30 1.5 mm layers, (E) Vamac 5022 spherical layers and (F) Vamac 5022 radial layers.*

The static stiffness of the bearing support significantly decreases when a viscoelastic support is applied. In fact, the radial stiffness decreases by a factor ranging from 10 for the spherical layer up to 620 for the radial layer design. What is clear from the graphs in Figure 7.10 is the direct relation between the vibration level and the radial support stiffness of the test rig, i.e. the lower the stiffness the lower the vibration level. Because the stiffness of the radial layer configuration just exceeds the required stiffness, it can be concluded from the analysed designs that this is the optimum regarding the vibration level.

7.5 Design of a viscoelastic bearing support for the electric motor

In this section a more elaborate design study is performed for the electric motor. It will be attempted to determine the design parameters for the viscoelastic bearing support of the electric motor in such a way that an optimal acoustic performance is obtained. For this purpose the stiffnesses as presented in Section 7.3 are varied for two types of viscoelastic material, Vamac 5022 and PMC 121/50.

7.5.1 Results for Vamac 5022 material

The stiffness parameters for a cylindrical Vamac 5022 viscoelastic layer with a 1.5 mm thickness, 11 mm width and 35 mm inner diameter, are collected in Table 7.1.

$k_{ax,bulk}$	0.0
$k_{ax,dev}$	$9.64 \cdot 10^{-1}$
$k_{til,bulk}$	$2.64 \cdot 10^{-10}$
$k_{til,dev}$	$2.98 \cdot 10^{-4}$
$k_{rad,bulk}$	$2.73 \cdot 10^{-4}$
$k_{rad,dev}$	$2.84 \cdot 10^{1}$

Table 7.1: *Stiffness parameter values for a cylindrical Vamac 5022 layer.*

The structural and acoustic analyses were performed in the frequency range 1000 to 2500 Hz in steps of 25 Hz, because in this range the highest sound power levels were observed. Moreover, the results of the numerical model showed a reasonably good agreement with the measured data in this frequency range. The frequency spectrum of the excitation of the system with Vamac 5022 supports, as determined earlier (Section 5.4.2), was used in the fully numerical simulations.

A study was performed in which the stiffness parameters were varied independently from each other. The values given in Table 7.1 were used as a reference set.

In Figure 7.11 the rms sound power level is shown as a function of the stiffness parameters $k_{rad,bulk}$, $k_{rad,dev}$ and $k_{til,dev}$, which are normalised to their reference values. In addition, a radial stiffness limit $k_{rad,lim}$ is shown.

Again, this limit was based on a maximum displacement of the bearing outer ring of 10 μm. Due to the rotor mass an 8.7 N radial gravitational load per bearing was applied. Note that the allowable stiffness range is at the right-hand side of this limit.

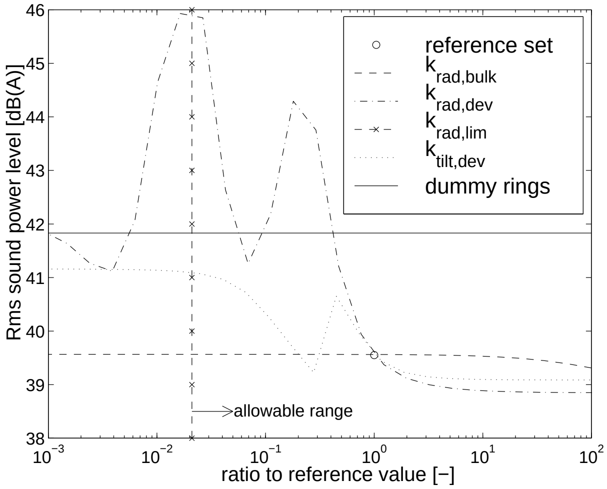

Figure 7.11: *The rms sound power level as a function of the stiffness ratios with actual excitation forces.*

Several observations are of interest. First, a variation of the deviatoric tilt or radial stiffness results in the most significant sound power changes. It was evaluated that the other stiffness parameters ($k_{ax,bulk}$,$k_{ax,dev}$,$k_{til,bulk}$) had a negligible influence on the rms sound power level and are therefore not considered.

Secondly, only an increase of the deviatoric tilt or radial stiffness decreases the rms sound power level when compared with the reference set. The maximum noise reduction relative to the motor with dummy rings was about 3.0 dB(A).

The optimal support stiffness, however, is strongly dependent on the applied excitation spectrum. If we take, for instance, an excitation force decreasing linearly with the frequency, see Figure 7.12, the study results in a completely different set of parameter values.

As an example, the sound power spectra for the optimal radial stiffness values in the case of the actual excitation ($k_{rad,dev} = 1.0e3$) and linear

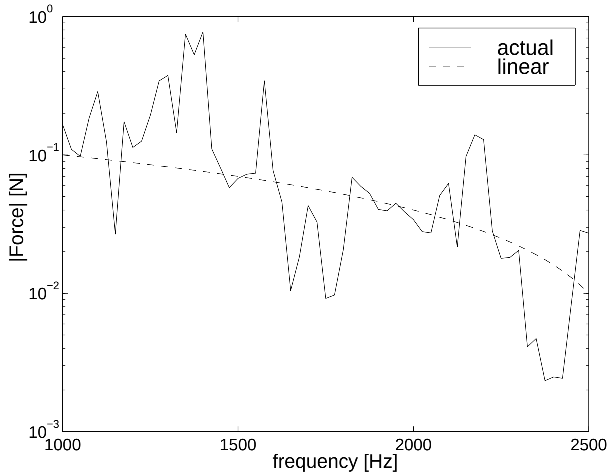

Figure 7.12: *Applied force spectra.*

excitation ($k_{rad,dev} = 1.2$) are presented in Figure 7.13.

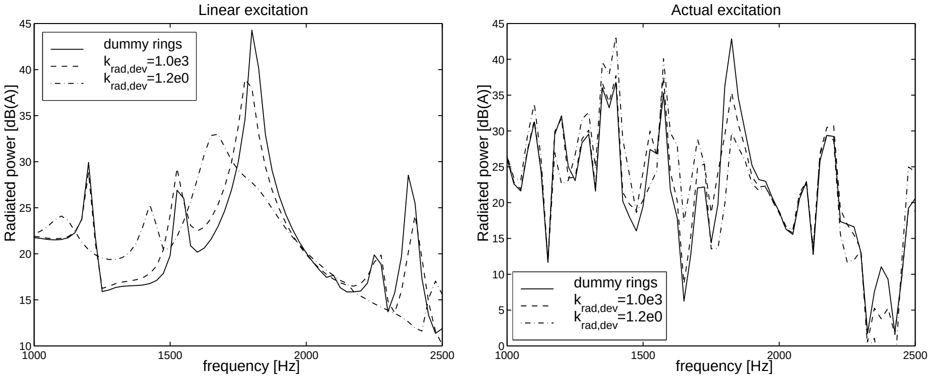

Figure 7.13: *Sound power spectra for linear and actual excitation forces.*

These figures indeed confirm that the optimal stiffness is highly dependent on the excitation behaviour. In the case of linear excitation the sound level peak at 1800 Hz is dominant. This peak is effectively reduced by decreasing the radial stiffness parameter to a value of 1.2. For the actual excitation, however, such a low stiffness results in high sound power levels around 1400 Hz. Therefore, the optimal stiffness is high ($k_{rad,dev} = 1.0e3$) if the actual excitation is considered.

7.5.2 Results for PMC 121/50 material

The optimised stiffness parameters also depend on the viscoelastic material properties. This is shown in Figure 7.14, in which the rms sound power values are shown for varying deviatoric radial and tilt stiffnesses of a PMC 121/50 material support.

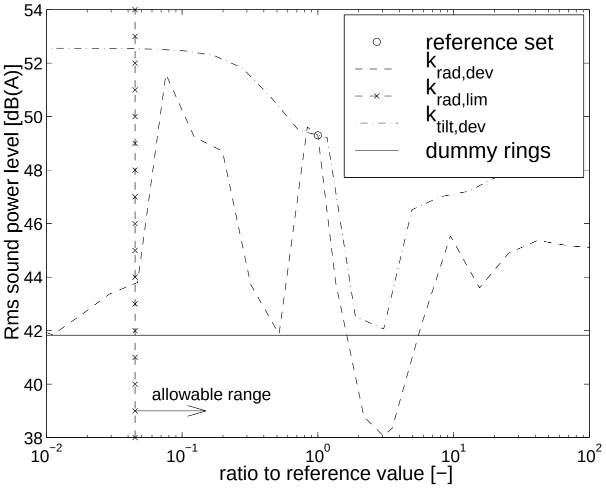

Figure 7.14: *Rms sound power level as a function of the stiffness ratios for PMC 121/50 material with actual excitation spectrum.*

By applying PMC 121/50 material, the sound power level of the electric motor can hardly be reduced. For most stiffness values, the rms sound power level is even higher than for the motor with dummy rings. However, when the radial stiffness of the support is increased by a factor 3, a reduction of about 4.0 dB(A) can be obtained. This is more than the 3.0 dB(A) sound reduction that is achieved with Vamac 5022 material.

Using the optimal (deviatoric) radial stiffness, the deviatoric tilt stiffness can be varied again. The results of this analysis are shown in Figure 7.15, showing that the optimal radial stiffness found in Figure 7.14 is indeed a global optimum.
By changing the tilt stiffness of the viscoelastic support in comparison with the reference value the sound power level always increases. Therefore, the optimal viscoelastic bearing support must have a radial stiffness of 3 times the reference value, whereas the other stiffness variables should be equal to

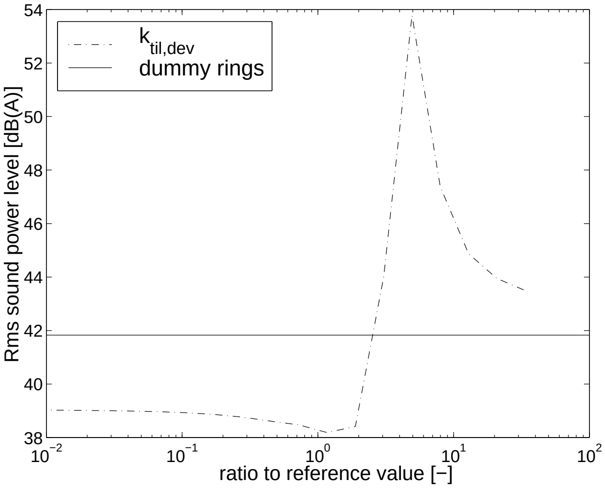

Figure 7.15: *Rms sound power level as a function of the tilt stiffness for PMC 121/50 material with optimal radial stiffness.*

the reference set.

In practice the radial stiffness of the layer can be increased in several ways. A thickness reduction from 1.5 mm to 1.0 mm, for example, would increase the radial stiffness by a factor 3 as is shown in Figure 7.5a. This also affects the tilt and axial stiffness, though, which is not desirable. The tilt stiffness, however, has only increased by a factor 1.9, which hardly affects the radiated sound power (see Figure 7.15). The tilt stiffness could be reduced by decreasing the inner radius of the layer, but due to the bearing size this is limited.

From these analyses it can be concluded that by using a properly designed viscoelastic bearing support the sound power level of the running electric motor can be reduced by about 4.0 dB(A).

7.6 Final considerations

A set of qualitative design rules and a more quantitive design approach have been presented. It was concluded that the stiffness of a viscoelastic bearing support can be optimised with respect to the equivalent radiated sound power of the application. Furthermore, the viscoelastic material choice depends on mechanical, thermal and chemical properties as well as on the life characteristics. Most essential, but not unexpected, is the fact that the design of an effective bearing support is strongly dependent on the dynamic behaviour of the application itself.

Based on the results for the VICTORIA test rig it can be stated that a viscoelastic bearing support has good potential for noise and vibration improvement of rolling bearing applications.
In the case of the electric motor, however, this potential has not been fully exploited. Several reasons can be proposed. First, vibration isolation was very difficult to achieve as in the electric motor the housing is directly excited by electromagnetic forces on the stator. It is very difficult to damp vibrations using only a relatively small piece of damping material in the vicinity of the bearings.
Secondly, the actual character of the excitation forces diminished the vibration damping potential of the viscoelastic layer. This influence is different for each application and could also turn out to be beneficial. It is concluded that viscoelastic bearing supports can be a solution for the electric motor to decrease the radiated noise, but the solution is not very robust. For a robust solution it must be attempted to create a significant vibration isolation in such a way that the dynamic response of the radiating surface of the structure decreases over a wide frequency range.

An important aspect that was disregarded in the numerical analyses is the influence by the viscoelastic bearing support on the electromagnetic excitation. This aspect fell outside the scope of this project. It is recommended, however, to investigate this topic in future research. Amongst others electromagnetic force calculations have been described by Arkkio (1987), Im (1997) and Neves (1999).

Chapter 8

Concluding remarks and Recommendations

8.1 Concluding remarks

This thesis described the dynamic and acoustic behaviour of rolling bearing applications with viscoelastic bearing supports. Ultimately, the investigations covered a wide range of aspects in mechanical engineering:

(1) the description of viscoelastic material behaviour;
(2) development of a new Component Mode Synthesis method for viscoelastic components;
(3) experimental investigations on the mechanical properties of viscoelastic materials;
(4) development of advanced structural models of rotor dynamics applications;
(5) numerical and experimental investigations on the dynamic and acoustic behaviour of an electric motor;
(6) development of a design strategy for noise reduction by viscoelastic bearing supports

To the author's knowledge, this is the first comprehensive study that combines a wide range of numerical tools (Maxwell, TTS, FEM, CMS, BEM) for the analysis of complex bearing applications.

The objectives that were defined in Section 1.5 have mainly been achieved. First, a numerical tool was developed to predict the dynamic and acoustic behaviour of rolling bearing applications with viscoelastic bearing supports. With respect to this result some important conclusions can be drawn:

- Linear viscoelastic behaviour can be described efficiently in the time and the frequency domains by a generalised Maxwell model. The measured material properties can be accurately approximated over a wide frequency range, i.e. from 10 Hz to 10 kHz, with 5 or 6 Maxwell elements.
- Component mode synthesis (CMS) has shown to be an efficient method for modelling rotor dynamics applications with viscoelastic bearing supports. CMS is applicable to viscoelastic FEM components provided that the equations of motion are written in a convenient linear form. This was validated with numerical analyses and experimental investigations on several ring samples.
- The excitation behaviour of a bearing application under operating conditions can be efficiently simulated with a harmonic response analysis using a hybrid modelling approach. This means that the harmonic forces are obtained by combining the measured acceleration data of a set of response points on the vibrating structure, and the predicted frequency response functions (FRF) between the location of the excitation force and the response points.
- A simple Boundary Element Method (BEM) model has shown to give satisfyingly accurate predictions of the sound power of a running electric motor in a wide frequency range. The accuracy is mainly determined by the structural velocities on the surface of the motor. In that respect, a hybrid modelling approach using measured velocity data gives better results.
- Efficient numerical models were developed for two applications with viscoelastic bearing supports; a rotor dynamics test rig and an electric motor. The test rig was successfully validated with dynamic experiments up to a frequency of 5 kHz. For the (running) electric motor the trends in the dynamic response showed an acceptable agreement up to about 2.5 kHz. Both numerical models have shown their value in design studies regarding noise and vibration.

The second aim of this study was to apply a viscoelastic bearing support in an actual rotor dynamics application. This was achieved for a rotor dynamics test rig and an electric motor.

The vibration level of the rotor dynamics test rig, characterised by strong resonant behaviour, was significantly reduced by viscoelastic bearing supports as a result of vibration isolation and damping.

For the electric motor a noise reduction of about 5 dB(A) was measured as a result of decreased excitation forces.

From the investigations of these systems two major conclusions can be drawn:

- Vibrations can be effectively isolated only if vibrations are transmitted from the rotor/shaft via the bearings to the housing. If the housing is directly excited, noise reduction must be achieved by increasing the damping of the system as well.
- In the case of an excitation spectrum with discrete peaks, such as for the electric motor, noise and vibration levels of rotating machinery may incedently even increase with a viscoelastic bearing support.
  For a more robust solution it is advised to create a significant vibration isolation such that the dynamic response of the radiating surface of the structure decreases over a wide frequency range.

Overall, it can be concluded that viscoelastic bearing supports are well suited to reduce the noise and vibration level of rotating machinery.

It should be noted, however, that the purpose of this thesis is not to give the exact solution for an optimal silencing layer, but to provide the engineer with a design strategy for an effective viscoelastic bearing support. As such, this study can be considered quite successful.

8.2 Recommendations

Finally, some recommendations for future research are given:

- A viscoelastic bearing support influences the excitation forces in a rolling bearing application under operating conditions. This aspect, however, was not investigated numerically in the present research. It is recommended that this aspect be examined in greater detail in future design studies. For this purpose, transient dynamic analyses need to be performed in which the excitation forces in the system are integrally computed.

- In order to compare a bearing application with and without viscoelastic support, the running accuracy in both systems must be equal. Therefore, the sandwich rings must be manufactured with accurate concentricity. In the present research, this was achieved to some extent for the PMC 121/50 material only. For accurate sandwich rings with Vamac material it is suggested to use an injection moulding process.

- In order to apply a viscoelastic bearing support in practice, a number of important aspects such as temperature, ageing, creep and life characteristics of the support must be investigated in more detail.

Acknowledgement

When I started working on this PhD project, I mainly considered it as a challenge. And a challenge it has been! But above all it was a fantastic experience during 4 years. I was very fortunate being able to use the knowledge and competences of both the SKF Engineering & Research Centre in Nieuwegein and the Applied Mechanics and Polymers group at the University of Twente. In that respect I would like to thank my promotor Henk Tijdeman, who played a crucial role in the cooperation between both organisations. I also thank him for the continuous support and enthousiasm in finishing this research.
From SKF ERC I would like to thank especially my assistent-promotor Jeroen Wensing. His contribution to this research has been very important. Whatever problem occurred, he always found a clever way to solve it. Thanks a lot!

From the Applied Mechanics and Polymers group at the University of Twente I would like to thank Remko Akkerman, André de Boer, Peter van der Hoogt, Ruud Spiering and Ysbrand Wijnant for their valuable contributions to this thesis and for the fruitful discussions.
Thanks also to my PhD student colleagues at the University of Twente: Marco Oude Nijhuis, René Visser and Clemens Beijers.

The list of people, who worked with me in SKF ERC and made me have a great time, has become quite long over the years. Of the System Dynamics Group at SKF ERC I want to thank Teun Zandbergen for his interest and support in this project. Also I thank my (ex-)colleagues of the (former) Noise and Vibration team for their help and the contribution to this work and creating a very pleasant office atmosphere: Raimond Breuker, Paul Dietl, Jean-Philippe Gaborel, Gerrit van Nijen, Daniele Sindaco and Emmanuel Villeneuve. Special thanks go to Arnoud Reininga for his direct contribution to the work in this thesis on the electric motor.

I also want to thank the people from the SKF ERC toolroom and the people from Chicago Rawhide Elastomer in Germany for the manufacturing of many products used in this research.
From SKF, I thank Stathis Ioannides for the encouraging support and I thank the Manager Director of SKF ERC for his kind permission to publish this work and for using foto material of SKF.
Of course, there have been many more persons in SKF ERC from all over the world, with who I shared fantastic times. Thanks to you all!

Obviously, I thank Debbie Vrieze for her fantastic administrative support. Thanks to her the communication between SKF and the University became very pleasant. Also, I would like to thank Katrina Emmett for her valuable suggestions concerning the English language.

Finally, I would like to thank all my family and friends. Special thanks go out to my parents, who greatly supported me during both my studies and this PhD study.

Nieuwegein, January 2003

Hedzer Tillema

Nomenclature

Roman scalars

a	acceleration	$[m/s^2]$
a_T	temperature shift factor	$[-]$
C_1, C_2	WLF-equation parameters	$[-], [K]$
c	viscous damping coefficient	$[Ns/m^2]$
c_0	velocity of sound	$[m/s]$
E	Young's modulus	$[N/m^2]$
e_{mn}	deviatoric part of strain tensor	$[-]$
F_c, F_c^j	contact force	$[N]$
G, G_i	shear modulus	$[N/m^2]$
$G(\vec{x})$	Green's function	$[-]$
G'	storage modulus	$[N/m^2]$
G''	loss modulus	$[N/m^2]$
G_d	complex dynamic shear modulus	$[N/m^2]$
G_{rel}	stress relaxation function	$[-]$
$\mathcal{H}$	history tensor	$[-]$
H_{FX}	transfer function between force and response	$[N/m]$
h	width	$[m]$
$\bar{\vec{I}}$	time averaged sound intensity	$[W/m^2]$
I_0	reference sound intensity	$[W/m^2]$
I_{xx}, I_{yy}, I_{zz}	mass moments of inertia	$[kgm^2]$
K	bulk modulus	$[N/m^2]$
k	free field wave number	$[m^{-1}]$
k_{ax}	axial stiffness of viscoelastic support	$[N/m]$
k_{cou}	coupling stiffness of viscoelastic support	$[N/m]$
k_{rad}	radial stiffness of viscoelastic support	$[N/m]$
k_{til}	tilt stiffness of viscoelastic support	$[N/rad]$
k_{tor}	torsional stiffness of viscoelastic support	$[N/rad]$

L_I	sound intensity level	$[dB]$
L_p	sound pressure level	$[dB]$
L_v	velocity level	$[dB]$
$L_{v,rms}$	rms velocity level	$[dB]$
L_W	sound power level	$[dB]$
L_{WA}	A-weighted sound power level	$[dB(A)]$
$L_{WA,rms}$	A-weighted rms sound power level	$[dB(A)]$
M_r, N_r	number of terms in series for u_r^{os}	$[-]$
M_t, N_t	number of terms in series for u_t^{os}	$[-]$
M_z, N_z	number of terms in series for u_z^{os}	$[-]$
N	number of Maxwell elements	$[-]$
N_p	number of patches	$[-]$
$\tilde{p}$	sound pressure perturbation	$[Pa]$
p	sound pressure amplitude	$[Pa]$
p_0	reference sound pressure amplitude	$[Pa]$
r	radius	$[m]$
r_H	reflection coefficient	$[-]$
r, θ, z	cylindrical coordinates	$[-]$
S	surface	$[m^2]$
s_{mn}	deviatoric part of stress tensor	$[-]$
T	temperature	$[^0C]$
T_0	reference temperature	$[^0C]$
t	time	$[s]$
t	thickness	$[m]$
u_r	radial displacement	$[m]$
u_t	tangential displacement	$[m]$
u_z	axial displacement	$[m]$
V	volume	$[m^3]$
$\tilde{\vec{v}}$	sound velocity perturbation	$[m/s]$
$\vec{v}$	sound velocity amplitude	$[m/s]$
v	velocity	$[m/s]$
$\langle \bar{v}^2 \rangle$	spatially averaged mean square velocity	$[m^2/s^2]$
v_n	normal sound velocity amplitude	$[m/s]$
v_{ref}	reference velocity amplitude	$[m/s]$
$\bar{W}$	time averaged sound power	$[W]$
W_0	reference sound power	$[W]$
$\vec{x}$	point in acoustic medium	$[-]$
x_b	translational interface degree of freedom	$[-]$
x_g	array with geometrical design variables	$[-]$

x_m	array with stiffness matrix design variables	$[-]$
Z	number of rolling elements	$[-]$
Z_{is}, Z_{os}	half width of layer	$[m]$

Greek scalars

α	conical layer angle	$[^0]$
γ_{mn}	shear strain tensor	$[-]$
δ	DMA phase angle	$[^0]$
δ_c	contact indentation	$[m]$
δ_{mn}	Cronecker delta	$[-]$
ε_{mn}	Cauchy strain tensor	$[-]$
ε_{kk}	hydrostatic part of strain tensor	$[-]$
ε_r	rotor eccentricity	$[m]$
ε_s	stator eccentricity	$[m]$
ζ_k	modal contribution coefficient	$[-]$
η	loss factor	$[-]$
η, η_i	viscosity	$[Ns/m^2]$
θ	patch angle	$[^0]$
κ	deflection coefficient	$[N/m]$
λ	eigenvalue	$[-]$
ν	Poisson's ratios	$[-]$
ρ	density	$[kg/m^3]$
ρ_0	density of air	$[kg/m^3]$
σ_{mn}	Cauchy stress tensor	$[-]$
σ_{kk}	hydrostatic part of stress tensor	$[-]$
σ	radiation efficiency	$[-]$
τ, τ_i	relaxation time	$[s]$
φ_b	rotational interface degree of freedom	$[-]$
ω	angular frequency	$[rad]$

Roman vectors

$\{a_r\}, \{b_r\}$	vectors with contributions of the series for u_r^{os}
$\{a_t\}, \{b_t\}$	vectors with contributions of the series for u_t^{os}
$\{a_z\}, \{b_z\}$	vectors with contributions of the series for u_z^{os}
$\{F\}$	vector with external forces
$\{f\}$	vector with generalised external forces
$\{h\}$	history vector

$\{p\}$	vector with generalised degrees of freedom
$\{p\}$	vector with nodal pressures
$\{q\}$	vector with bearing degrees of freedom
$\{q_k\}$	eigenvector of radiation modes problem
$\{R\}$	right hand side vector
$\{v\}$	vector with normal velocities
$\{x\}$	vector with nodal degrees of freedom
$\{x_b\}$	vector with nodal interface degrees of freedom

Greek vectors

$\{\varepsilon\}$	strain vector
$\{\zeta\}$	vector containing modal contribution coefficients
$\{\phi\}$	basis functions for sound pressure and velocity
$\{\sigma\}$	stress vector

Roman matrices

$[A], [B]$	acoustic system matrices
$[B]$	matrix relating $\{\varepsilon\}$ and $\{x\}$
$[C]$	damping matrix
$[C]$	power coupling matrix
$[c]$	generalised damping matrix
$[D]$	viscous material matrix
$[E]$	elastic material matrix
$[H]$	history matrix
$[I]$	identity matrix
$[K]$	stiffness matrix
$[k]$	generalised stiffness matrix
$[M]$	mass matrix
$[m]$	generalised mass matrix
$[N]$	matrix with shape functions
$[Q]$	matrix with eigenvectors of radiation modes problem
$[T_1], [T_2]$	transformation matrices

Greek matrices

$[\Lambda]$	matrix with eigenvalues
$[\Psi]$	matrix with column-wise stored shape functions

super-/subscripts

ax	axial
$calc$	calculated values
dev	deviatoric
i	referring to the inner ring
i	referring to Maxwell element number
j	referring to rolling element number
lim	limit
$meas$	measured values
n	normal
o	referring to outer ring
$pred$	predicted values
rad	radial
ref	reference
res	resultant
rms	root mean square
s	surface
til	tilt
tor	torsional
ve	viscoelastic

abbreviations

AP	auto-power spectrum
BEM	boundary element method
CMS	component mode synthesis
DGBB	deep groove ball bearing
DMA	dynamic mechanical analyzer
DOF	degree of freedom
EHL	elasto-hydrodynamic lubrication
FEM	finite element method
FRF	frequency response function
TTS	time temperature superposition
WLF	William, Landel and Ferry
XP	cross-power spectrum

Appendix A

History vector derivation

The equations of motion of a viscoelastic FEM component are expressed as:

$$[M_{ve}]\{\ddot{x}\}^{p+1} + [C_{ve}]\{\dot{x}\}^{p+1} + [K_{ve}]\{x\}^{p+1} = \{F\} - [H_{ve}]\{h_x\}^{p+1} \tag{A.1}$$

where $[M_{ve}]$, $[C_{ve}]$, $[K_{ve}]$ and $[H_{ve}]$ represent the mass, damping, stiffness and history matrix, respectively. The externally applied forces are stored in the vector $\{F\}$. The history vector $\{h_x\}^{p+1}$ is a vector with respect to the (FEM) DOF $\{x\}$ containing the deformation rates from the past:

$$\{h_x\}^{p+1} = \sum_{i=1}^{N} \{h_x\}_i^{p+1} \tag{A.2}$$

$$\{h_x\}_i^{p+1} = c_{1,i}\{\dot{x}\}^p + c_{2,i}\{h_x\}_i^p \tag{A.3}$$

where i is the Maxwell element number and N the total number of Maxwell elements. The constants $c_{1,i}$ and $c_{2,i}$ are defined as:

$$c_{1,i} = 2\eta_i(1 - c_{2,i}) - \frac{\Delta t - \tau_i(1 - c_{2,i})}{\Delta t} + \frac{\Delta t - \tau_i(1 - c_{2,i})}{\Delta t c_{2,i}} \tag{A.4}$$

$$c_{2,i} = exp(-\Delta t/\tau_i) \tag{A.5}$$

where η_i and τ_i denote the viscosity and relaxation time of the i-th Maxwell element, respectively. The time step is denoted by $\Delta t = t^p - t^{p-1}$.

Equation A.3 can also be written as a function of the previous velocity vectors as:

$$\begin{aligned} \{h_x\}_i^{p+1} &= c_{1,i}\{\dot{x}\}^p + c_{2,i}\{h_x\}_i^p \\ &= c_{1,i}\{\dot{x}\}^p + c_{1,i}c_{2,i}\{\dot{x}\}^{p-1} + c_{2,i}\{h_x\}_i^{p-1} \\ &= c_{1,i}\{\dot{x}\}^p + c_{1,i}c_{2,i}\{\dot{x}\}^{p-1} + c_{1,i}c_{2,i}^2\{\dot{x}\}^{p-2} + .. \\ &.. + c_{1,i}c_{2,i}^{p-1}\{\dot{x}\}^1 + c_{1,i}c_{2,i}^{p}\{\dot{x}\}^0 + c_{2,i}^{p+1}\{h_x\}_i^0 \end{aligned} \tag{A.6}$$

The vectors $\{h_x\}_i^0$ are equal to zero, because there is no history assumed at time $t = 0$.

In accordance with the Component Mode Synthesis the DOF vector $\{x\}$ is written as a linear combination of shape functions: $\{x\} = [\Psi]\{p\}$. The vector $\{p\}$ contains the generalised degrees of freedom. Substitution of this relation in combination with equation A.6 into the equations of motion yields:

$$\begin{aligned} &[M_{ve}][\Psi]\{\ddot{p}\}^{p+1} + [C_{ve}][\Psi]\{\dot{p}\}^{p+1} + [K_{ve}][\Psi]\{p\}^{p+1} = \\ &\{F\} - [H_{ve}][\Psi]\sum_{i=1}^{N}(c1_i\{\dot{p}\}^p + c1_ic2_i\{\dot{p}\}^{p-1} + .. + c1_ic2_i^p\{\dot{p}\}^0) \end{aligned} \tag{A.7}$$

Pre-multiplying with $[\Psi]^T$ results in:

$$\begin{aligned} &[\Psi]^T[M_{ve}][\Psi]\{\ddot{p}\}^{p+1} + [\Psi]^T[C_{ve}][\Psi]\{\dot{p}\}^{p+1} + [\Psi]^T[K_{ve}][\Psi]\{p\}^{p+1} = \\ &\{F\} - [\Psi]^T[H_{ve}][\Psi]\sum_{i=1}^{N}(c1_i\{\dot{p}\}^p + c1_ic2_i\{\dot{p}\}^{p-1} + .. + c1_ic2_i^p\{\dot{p}\}^0) \end{aligned} \tag{A.8}$$

As a consequence, the reduced set of equations can be written as:

$$[m_{ve}]\{\ddot{p}\} + [c_{ve}]\{\dot{p}\} + [k_{ve}]\{p\} = \{f\} - [h_{ve}]\{h_p\} \tag{A.9}$$

where $[m_{ve}]$, $[c_{ve}]$, $[k_{ve}]$ and $[h_{ve}]$ are the reduced mass, damping, stiffness and history matrix, respectively:

$$[m_{ve}] = [\Psi]^T[M_{ve}][\Psi] \tag{A.10}$$

$$[c_{ve}] = [\Psi]^T[C_{ve}][\Psi] \tag{A.11}$$

$$[k_{ve}] = [\Psi]^T[K_{ve}][\Psi] \tag{A.12}$$

$$[h_{ve}] = [\Psi]^T[H_{ve}][\Psi] \tag{A.13}$$

$$\{f\} = [\Psi]^T\{F\} \tag{A.14}$$

The vector $\{h_p\}$ is now based on the generalised DOF $\{p\}$:

$$\begin{aligned} \{h_p\}^{p+1} &= \sum_{i=1}^{N}(c1_i\{\dot{p}\}^p + c1_ic2_i\{\dot{p}\}^{p-1} + c1_jc2_j^2\{\dot{p}\}^{p-2} + .. \\ &\qquad .. + c1_ic2_i^{p-1}\{\dot{p}\}^1 + c1_ic2_i^p\{\dot{p}\}^0) \\ &= \sum_{i=1}^{N}(c1_i\{\dot{p}\}^p + c2_i\{h_p\}_i^p) \end{aligned} \tag{A.15}$$

Appendix B

Maxwell model parameters

The parameters of the generalised Maxwell representation (Figure B.1), used to curve-fit the viscoelastic materials, are listed in Table B.1.

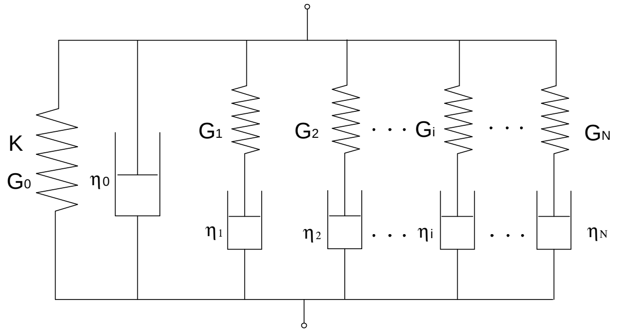

Figure B.1: *The generalised Maxwell model*

	Vamac 5022	Vamac 6522	PMC 121/30	PMC 121/50	PMC 860
G_0	0.7155e6	0.9437e7	3.2912e5	5.9780e5	0.1405e7
G_1	3.9236e6	6.3629e7	1.6191e5	4.6526e5	1.3622e7
G_2	1.3578e6	1.7770e7	0.6330e5	1.6653e5	0.3227e7
G_3	1.3722e6	0.7059e7	0.4662e5	0.7876e5	0.1208e7
G_4	0.8004e6	0.4924e7	0.0805e5	0.1968e5	0.0425e7
G_5	0.7734e6	0.2871e7	0.4928e5	0.4233e5	0.0232e7
G_6	-	0.4343e7	-	-	0.0181e7
η_0	78.0	50.0	2.0	13.0	6.0
η_1	1.9618e2	6.3629e1	8.0954e0	2.3263e1	1.3622e1
η_2	6.7889e2	1.7770e2	3.1648e1	8.3263e1	3.2271e1
η_3	6.8610e3	7.0587e2	2.3311e2	3.9382e2	1.2078e2
η_4	4.0020e4	4.9236e3	4.0253e2	9.8387e2	4.2474e2
η_5	3.8672e5	2.8710e4	2.4638e4	2.1166e4	2.3197e3
η_6	-	4.3428e5	-	-	1.8072e4

Table B.1: *Maxwell model parameters for several viscoelastic materials (units G_i in N/m^2, η_i in Ns/m^2).*

Appendix C

Properties of a DGBB 6202

The geometrical and material properties of a 6202 deep groove ball bearing, required for the calculations, are listed in Table C.1.

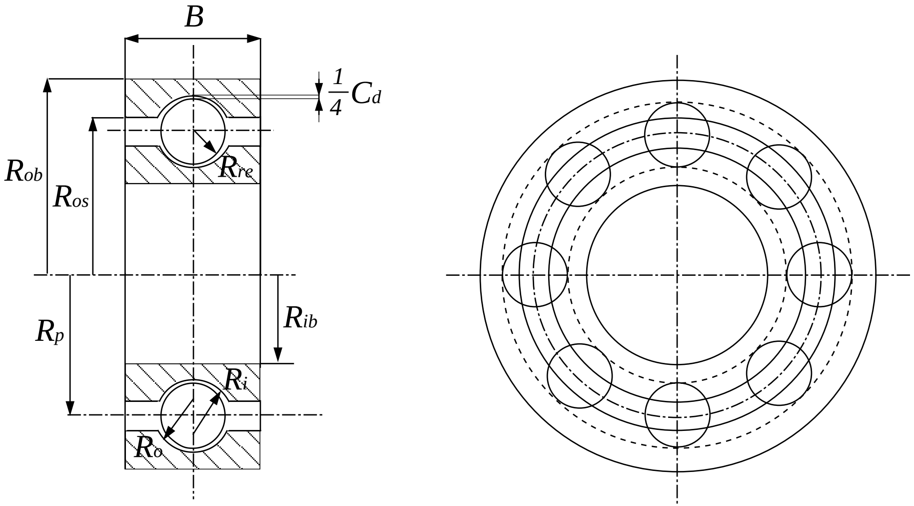

Figure C.1: *Geometrical properties of a deep groove ball bearing.*

ball bearing	
outer ring width:	$B = 11.0$ mm
outer bore radius:	$R_{ob} = 17.5$ mm
outer shoulder radius:	$R_{os} = 14.6$ mm
outer groove radius:	$R_o = 3.24$ mm
inner bore radius:	$R_{ib} = 7.5$ mm
inner groove radius:	$R_i = 3.07$ mm
number of rolling elements:	$Z = 8$
pitch radius:	$R_p = 12.63$ mm
radial clearance:	$C_d = 10\ \mu m$
ball radius	$R_{re} = 3.0$ mm
modulus of elasticity:	$E = 2.06\text{e}11$ Pa
Poisson's ratio:	$\nu = 0.3$
density:	$\rho = 7800$ kg/m^3
contact damping coefficient:	$c_{res} = 100$ Ns/m^2

Table C.1: *Geometrical and material properties of a DGBB 6202.*

Bibliography

Aktürk, N. and Gohar, R. (1994). Damping the vibrations of a rigid shaft supported by ball bearings by means of external elastomeric O-ring dampers. *Journal of Engineering Tribology*, 208:183–190.

Alfrey, T. (1944). Non-homogeneous stresses in viscoelastic media. *Q. Appl. Math.*, II(2):113-119.

Alfrey, T. (1948). *Mechanical behaviour of high polymers.* Interscience, New York.

Arkkio, A. (1987). Analysis of induction motors based on the numerical solution of the magnetic field and circuit equations. *Acta Polytechnica Scandinavia, Electrical Engineering Series*, 59.

Baaijens, F. P. T. (1991). *Applied computational mechanics.* Lecture notes, University of Eindhoven, The Netherlands.

Bagley, R. L. and Torvik, P. J. (1983). Fractional calculus - a different approach to the analysis of viscoelastically damped structures. *AIAA Journal*, 21(5):741-748.

Barber, A. (1992). *Handbook of noise and vibration control.* Elsevier Advanced Technology, Oxford.

Basten, T. G. H. (2001). *Noise reduction by viscothermal acousto-elastic interaction in double wall panels.* PhD thesis, University of Twente, the Netherlands, ISBN 90-3651597-1.

Bathe, K. J. (1982). *Finite element procedures in engineering analysis.* Prentice-Hall, New Jersey.

Baz, A. (1993). Active constrained layer damping. *Proceedings of Damping '93*, IBB:1–23.

Benthien, G. W. and Schenk, H. A. (1991). Structural-acoustic coupling, in *Boundary element methods in acoustics*, edited by R.D. Ciskowski and C.A. Brebbia. Elsevier Applied Science, London, Chapter 6.

Borgiotti, G. V. (1990). The power radiated by a vibrating body in an acoustic fluid and its determination from boundary measurements. *Journal of the Acoustical Society of America*, 88(4):1884–1893.

Ciskowski, R. D. and Brebbia, C. A. (1991). *Boundary element methods in acoustics*. Elsevier Applied Science, London.

Craig, R. R. and Bampton, M. C. C. (1968). Coupling of substructures for dynamic analysis. *AIAA Journal*, 6(7):1313–1319.

Cunefare, K. (1991). The minimum multi-modal radiation efficiency of baffled infinite beams. *Journal of the Acoustical Society of America*, 90:2521–2529.

Cunefare, K. and Currey, M. N. (1994). On the exterior acoustic radiation modes of structures. *Journal of the Acoustical Society of America*, 96(4):2302–2312.

Dovstam, K. (1995). Augmented Hooke's law in frequency domain. A three-dimensional, material damping formulation *International Journal of Solids and Structures*, 32(19):2835–2852.

Dutt, J. K. and Nakra, B. C. (1992). Stability of rotor systems with viscoelastic supports. *Journal of Sound and Vibration*, 153(1):89–96.

Dutt, J. K. and Nakra, B. C. (1992). Vibration response reduction of a rotor shaft sytem using viscoelastic polymeric supports. *Journal of Vibration and Acoustics*, 115:221–223.

Elliott, S. J. and Johnson, M. E. (1993). Radiation modes and the active control of sound power. *Journal of the Acoustical Society of America*, 94(4):2194–2204.

Enelund, M. and Olsson, P. (1997). Time-domain finite element analysis of viscoelastic structures with fractional derivatives constitutive relations. *AIAA Journal*, 35(10):1630–1637.

Ferry, J. D. (1980). *Viscoelastic properties of polymers.* John Wiley & Sons, New York.

Filippi, P. J. T. (1977). Layer potentials and acoustic diffraction. *Journal of Sound and Vibration*, 54:473–500.

Flügge, W. (1975). *Viscoelasticity.* Springer Verlag, New York.

Fung, Y. C. (1965). *Foundations of solid mechanics.* Prentice-Hall, Eaglewood Cliffs, New Jersey.

Hertz, H. (1881). Über die Berührung fester elastischen Körper. *Journal für die reine und angewandete Mathematik*, 92:156–171 (in German).

Im, D. H., et al. (1997). Analysis of radial force as a source of vibration in an induction motor with skewed slots. *IEEE Transactions on Magnetics*, 33(2):1650–1653.

Kessels, P. (2000). *Engineering toolbox for structural-acoustic design.* PhD thesis, University of Eindhoven, the Netherlands, ISBN 90-3862682-7.

Kirkup, S. M. (1998). *The Boundary element methods in acoustics.* Integrated Sound Software.

Kuijpers, A. H. W. M. (1999). *Acoustics modelling and design of MRI-scanners.* PhD thesis, University of Eindhoven, the Netherlands, ISBN 90-3860648-6.

Lakes, R. S. (1998). *Viscoelastic solids.* CRC Press, Boca Raton.

Lesieutre, G. A. and Mingori, D. L. (1990). Finite element modeling of frequency-dependent material damping using augmenting thermodynamic fields. *Journal of Guidance, Control and Dynamics*, 13(6):1040–1050.

Lesieutre, G. A. and Bianchini, E. (1995). Time domain modeling of linear viscoelasticity using anelastic displacement fields. *Journal of Vibration and Acoustics*, 117(4):424–430.

Mead, D. J. (1998). The forced vibration of a three-layer, damped sandwich beam with arbitrary boundary conditions. *Journal of Sound and Vibration*, 10(2):163–175.

Nakra, B. C. (1998). Vibration control in machines and structures using viscoelastic damping. *Journal of Sound and Vibration*, 211(3):449–465.

Nashif, A. D., Jones, D. I. G. and Henderson, J. P. (1985). *Vibration damping.* John Wiley & Sons, New York.

Neves, C. G. C., et al. (1999). Experimental and numerical analysis of induction motor vibrations. *IEEE Transactions on Magnetics*, 35(3):1314–1317.

Panda, K. C. and Dutt, J. K. (1999). Design of optimum support parameters for minimum rotor response and maximum stability limit. *Journal of Sound and Vibration*, 223(1):1–21.

Ross, D., Ungar, E. E. and Kerwin, E. M. (1959). Damping of plate flexural vibrations by means of visco-elastic laminae. *Structural Damping ASME*, section 3.

Sas, P., Augusztinovicz F. and Ossipov A. (2001). Pressure gradient acoustic intensity measurements. *from Advanced Dynamics of Structures course lectures*, University of Twente.

Schwarzl, F. and Staverman A. J. (1952). Time-temperature dependence of linear viscoelastic behaviour. *Journal Applied Physics*, 23:838–843.

Shabaneh, N.H. and Zu, J.W. (2000). Dynamic analysis of rotor-shaft systems with viscoelastically supported bearings. *Mechanisms and Machine Theory*, 35:1313–1330.

Shen, I. Y. (1996). Stability and controllability of Euler-Bernoulli beams with intelligent constrained layer treatments. *Journal of Vibration and Acoustics*, 118:70–77.

SKF, editor (2002). *SKF General Catalogue*. Carl Gerber GmbH, Germany.

Tillema, H. G. (2001). Dynamic behaviour of ball bearing applications with constrained damping layers. 19^{th} *International Modal Analysis Conference, Kissimmee FL, USA*.

Tillema, H. G. and Wensing, J. A. (2002a). Validation of a rotor dynamics model with viscoelastic bearing supports. *International Conference on Structural Dynamics Modelling, Madeira, Portugal*.

Tillema, H. G. and Wensing, J. A. (2002b). Acoustic analysis of an induction motor with viscoelastic bearing supports. *Internoise conference, Dearborn MI, USA*.

Wensing, J. A. (1998a). *On the dynamics of ball bearings*. PhD thesis, University of Twente, the Netherlands, ISBN 90-3651229-8.

Wensing, J. A. (1998b). Dynamic behaviour of ball bearings on vibration test spindles. 16^{th} *International Modal Analysis Conference, Santa Barbara, USA*.

Wensing, J. A. and Nijen, G. C. v. (2001). The dynamic behaviour of a system that includes a rolling bearing. *Proc. Institute of Mechanical Engineers*, 215(1):509–518.

Wijnant, Y. H. (1998). *Contact dynamics in the field of elastohydrodynamic lubrication.* PhD thesis, University of Twente, the Netherlands, ISBN 90-3651223-9.

Wijnant, Y. H., Wensing, J. A. and Nijen, G. C. v. (1999). The influence of lubrication on the dynamic behaviour of ball bearings. *Journal of Sound and Vibration*, 222(4):579–596.